Johanna Spitzer, BSc

Engineering geological and geomechanical analysis of a rock slope in the Ödenwinkelkees – Focus on the determination of the discontinuity network and its characteristics

Master's Thesis

Submitted in fulfilment of the requirements for the degree of

Master of Science

Master's programme Geoscience

at

Graz University of Technology

Supervisor
Univ.-Prof. Dipl.-Ing. Dr.-Ing.Thomas Marcher

Co Supervisor
Thomas Geisler, MSc

Mag. Gerald Valentin

Institute of Rock Mechanics and Tunnelling
Graz University of Technology

Graz, March 2021

EIDESSTATTLICHE ERKLÄRUNG
AFFIDAVIT

Ich erkläre an Eides statt, dass ich die vorliegende Arbeit selbstständig verfasst, andere als die angegebenen Quellen/Hilfsmittel nicht benutzt, und die den benutzten Quellen wörtlich und inhaltlich entnommenen Stellen als solche kenntlich gemacht habe. Das in TUGRAZonline hochgeladene Textdokument ist mit der vorliegenden Masterarbeit identisch.

I declare that I have authored this thesis independently, that I have not used other than the declared sources/resources, and that I have explicitly marked all material which has been quoted either literally or by content from the used sources. The text document uploaded to TUGRAZonline is identical to the present master‘s thesis.

Datum / Date	Unterschrift / Signature

Principle of equality

Due to reasons of legibility, this work does not include gender-specific formulations. However, the used male expressions stand for both genders.

Acknowledgement

I would like to thank Prof. Dr. Thomas Marcher for the opportunity of writing this interesting master thesis at the Institute of Rock Mechanics and Tunnelling at TU Graz.

I want to thank M.Sc. Thomas Geisler for the supervision of this exciting master thesis. The advice and opportunity to always ask questions was very helpful.

Furthermore, I want to thank Mag. Gerald Valentin for showing me around at the field site and the meaningful ideas and suggestions. I would like to thank for the organization and possibility to spend a few days at the Ödenwinkelkees for the field work. I also want to thank Bernhard Zagel for the organization and support making the field work possible.

I also want to thank Mag. Ingo Hartmeyer from Georesearch Forschungsgesellschaft mbH, for providing information about their studies at the Ödenwinkelkees and the opportunity to ask for help when I needed it.

Abstract

Climate warming leads to the retreat of alpine glaciers. Therefore, rock slope failures are increasing as the rock slope must adjust to new boundary conditions. With concurrently increasing infrastructure in the higher mountains, these rock slope failures can lead to a serious risk. Glaciation and deglaciation impose stresses on underlying bedrock. These can be induced by mechanical (erosion, oversteepening), thermal (solar radiation, temperature cycles) or hydrological (groundwater fluctuations, increased pore pressures) processes and furthermore, by cryogenic processes like freeze-thaw weathering and permafrost degradation. A rock slope close to the Ödenwinkelkees (Tauern range, Salzburg) was previously covered by the glacier, but is exposed since the end of the Little Ice Age in the mid-19th century. A geomechanical analysis of the discontinuity network contribute to the evaluation of how glacier retreat affects rock slope stability. The rearrangement of in-situ stresses and development of high stress ratios after deglaciation leads to the formation of new joints often referred to as sheeting joints. For data acquisition traditional field work methods were used. Several measurements of dip and dip direction were conducted with the geological compass and scanline mapping aided to determine further discontinuity characteristics. Photographic analyses of the rock slope provided information about the spatial pattern of the discontinuity network, which can be statistically evaluated. The obtained data was afterwards analysed using the software Dips 7.0. As a result, four joint sets can be differentiated. Whereas the development of the first two prominent and persistent discontinuity sets can be linked to glacial processes. According to kinematic analyses the rock slope stability dominantly depends on the orientation of these joint sets in respect to the slope orientation. Sliding and toppling are both feasible failure modes. Surface parallel joint planes are favourably oriented for planar sliding and rock mass is prone to failure if the joints daylight.

High in-situ stress ratios caused by glacier retreat may play a dominant role for discontinuity development. Afterwards, thermal and hydrological stresses drive progressive fracture propagation through intact rock, connecting joint planes and resulting in very persistent discontinuities. Main processes may be water infiltration generating high pore water pressures, and the combination with temperatures around 0 °C, leading to increased freeze-thaw weathering. Additionally, the subsurface temperature regime changes after the protective glacier cover disappeared. The analyses indicate that permafrost does not play a dominant role during present rock slope weakening processes. The altitude of 2200 to 2300 m and easterly exposed rock slope indicate that permafrost is not present in the shallow subsurface anymore.

Kurzfassung

Die Auswirkungen des Klimawandels sind besonders im Alpenraum zu beobachten. Die erhöhten Temperaturen lassen Gletscher in den Alpen schmelzen, was negative Auswirkungen auf die Felsstabilität haben und zu erhöhter Felssturzaktivität führen kann.
Mit gleichzeitig besser ausgebauter Infrastruktur in den Bergen, kann das in Zukunft zu einem erhöhten Risiko werden.
Durch die Entgletscherung entstehen Spannungen im Gebirge. Diese können sich durch mechanische (Erosion, Steilhang), thermische (Sonnenstrahlung, Temperatur-schwankungen), hydrologische (Grundwasserschwankungen, Porenwasserdruck) oder eismechanische (Frost-Tau-Wechsel, Permafrostdegradierung) Prozesse entwickeln.
Ein Berghang in der Nähe des Ödenwinkelkees (Hohe Tauern, Salzburg) ist seit dem Ende der kleinen Eiszeit, Mitte des 19. Jh, nicht mehr von dem Gletscher bedeckt. Eine geomechanische Analyse des Berghangs und des Trennflächengefüges soll mehr Informationen über den Einfluss der Entgletscherung auf die Hangstabilität geben.
Eine Umverteilung der Spannungen in der Felsformation und hohe Spannungsverhältnisse führen zu der Entwicklung von hangparallelen Klüften. Messungen wurden während der Feldarbeit mit traditionellen Methoden durchgeführt. Neigungswinkel und –richtung der Trennflächen wurden mit dem geologischen Kompass und weitere Eigenschaften mit Hilfe der Scanline festgestellt. Durch fotografische Analysen des Berghangs, kann das Trennflächengefüge näher beschrieben und statistisch ausgewertet werden. Die Daten der Kompass Messungen wurden daraufhin mit der Software Dips 7.0 analysiert. Vier Trennflächensets konnten definiert werden, wobei die ersten beiden markanteren und durchgängigen Sets vermutlich durch die Entgletscherung entstanden sind. Diese bestimmen auch die Versagensmechanismen. Nach der kinematischen Analyse sind Rutschen und Kippen mögliche Mechanismen. Besonders die hangparallelen Klüfte sind vorteilhaft für Rutschungen entlang der Trennflächen orientiert.
Die Entstehung der Klüfte kann vor allem auf die Spannungsumverteilung im Gestein zurückgeführt werden. Darüber hinaus können weitere thermische und hydrologische Spannung zu fortschreitender Bruchausbreitung führen, wodurch durchgängige Trennflächen entstehen. Dominierende Prozesse können erhöhte Wasserinfiltration und die damit verbundene Erhöhung des Porendrucks sein. Die Kombination mit Temperaturen um den Gefrierpunkt führt, durch Frost-Tau-Wechsel, zur Verwitterung und folglich zu weiterer Brauchausbreitung. Permafrostdegradation spielt womöglich keine dominierende Rolle. Die Höhe von 2200 bis 2300 m und die östliche Orientierung des Berghangs sprechen dafür, dass kein Permafrost mehr im oberflächennahen Untergrund vorhanden ist.

Table of contents

List of figures

List of tables

Abbreviations

LIA .....Little Ice Age

LGM.....last glacial maximum

IPA.....International Permafrost Association

JS .....joint set

JRC .....joint roughness coefficient

ZAMG .....Zentralanstalt für Meteorologie und Geodynamik

DEM .....digital elevation model

Symbols

γ_r.....unit weight of rock [MN/m³]

H.....depth of overburden [m]

σ_1.....major principal stress [MPa]

σ_2.....intermediate principal stress [MPa]

σ_3.....least principal stress [MPa]

σ_n.....normal stress [MPa]

θ .....joint inclination angle [°]

Ψ_S.....slope dip angle [°]

Ψ_P.....discontinuity plane dip angle [°]

α_S.....slope dip direction [°]

α_P.....discontinuity plane dip direction [°]

ϕ_j.....friction angle of the discontinuity surface [°]

1 Introduction

1.1 Motivation

Global warming highly affects high-alpine, glacial environments. Glaciers are retreating in the European Alps since the Little Ice Age (LIA). Since then Alpine glaciers lost almost 50 % of their area until 2000 (Zemp *et al.*, 2006). Rock slopes are exposed and one consequence is an increasing number of rockfall events (Krautblatter *et al.*, 2013) . The areas are converting to a paraglacial environment and slopes have to adjust to new boundary conditions (Deline *et al.*, 2015). As a result rock-slope failures and rock-mass deformations can develop (Baroni *et al.*, 2014). Because of an increasing urban development in mountain areas at the same time, rock slope stability assessment in alpine environments becomes increasingly important (Fischer *et al.*, 2010). Additionally, future climate warming will lead to further glacier retreat and expose bedrock, which may result in increased rates of rockfalls in these regions (Zemp *et al.*, 2006).

For slope stability assessment knowledge about the internal structures and mechanisms that control slope movements are necessary (Willenberg *et al.*, 2008). Discontinuity patterns are created due to the geological and tectonic genesis, repeated glaciation cycles, the erosional and stress history and small-scale mechanical, thermal, hydrological, and chemical processes (Messenzehl, 2018). Discontinuity characteristics like orientation, persistence, spacing, surface roughness and seepage control the rock slope stability (Wyllie & Mah, 2005). New joints can be generated due to paraglacial stress changes. These may progressively propagate through intact rock connecting non-persistent discontinuities (Fischer *et al.*, 2010). Warming and thawing of rock permafrost and increasing rock weathering activity reduce the stability of rock slopes additionally (Ewald *et al.*, 2019).

Sliding or toppling are the most common failure mechanisms corresponding to jointed rock masses of steep slopes. Joint condition and orientation controls if rock blocks are kinematically free to fail as well as the size of mobilised rock blocks (Fiorucci *et al.*, 2018).

The Ödenwinkelkees, a glacier in the Glockner group in Salzburg is melting due to climate change (Slupetzky, 2020). A rock slope located in the proximity to the glacier was covered by ice for a long time, but now it is exposed to external influences. The discontinuity network within the rock mass is characterized, firstly to determine if the discontinuities have a glacier-related or tectonic origin; and secondary to evaluate potential failure mechanisms.

1.2 Aims of the thesis

The aim of this thesis is to investigate how glacial retreat is linked to rock slope instabilities in the area of the Ödenwinkelkees. Data of the rock mass is collected by using traditional field mapping methods in order to characterize the discontinuity sets and to generate information about:

- Which discontinuities developed due to glacier-related stress changes and which due to tectonic forces?
- What are the main potential failure mechanisms, as well as which discontinuities contribute to a higher probability of rock slope failure?
- How does the (de)glaciation affect the stability of the rock slope?
- Is there a spatial or temporal pattern of glacier-related discontinuities recognizable?

2 Background

2.1 Glacial history of the European Alps

The Pleistocene epoch was characterized by repeated glacial and interglacial cycles in the European Alps (Grämiger *et al.*, 2018). During this epoch, the Eemian interglacial with likely warmer and ice-free conditions was between ~130 to 114 kyr. The following Würmian glacial period lasted ~ 100 kyr and peaked at the last glacial maximum (LGM). Between 28 kyr and 18 kyr BP, the central alps were almost completely covered by glaciers. This time period was characterised by ice fields that fed an interconnected system of valley glaciers that reached the Alpine forelands. Strong glacier retreat occurred after the LGM by ~19 to 18 kyr, followed by some Late Glacial readvances. The next cold period, the Younger Dryas, was between 12.8 to 11.5 kyr. Afterwards a warmer period followed again, and glaciers retreated. During the Holocene time period, which begins 10.7 kyr BP several glacier retreats and readvances happened. The most recent period of glacier expansion, the Little Ice Age (LIA) was around 1500 to 1850, while a dramatic retreat of glaciers followed during the 20th century until today (Grämiger *et al.*, 2018).

2.2 Paraglacial factors of slope failure

Paraglacial slope failures are part of or influenced by the transition from glacial conditions to non-glacial conditions (McColl, 2012). The research work dealing with paraglacial processes increased in recent years. However, it is often difficult to determine if rock slope failures occurred because of deglaciation and which mechanisms are the most effective ones destabilizing the slope (Krautblatter *et al.*, 2013).

The stability of alpine rock walls is depending on several factors like the long-term geomorphic evolution of the slope, the topographic and geological setting, geotechnical properties of the rock mass and hydrogeology (Fischer et al., 2010). Due to glacial retreat an initially stable rock slope may destabilize because of changing boundary conditions (mechanical, thermal or hydrological) (Deline et al., 2015).

(McColl, 2012) established a concept of paraglacial instability assessment with three states of a rock slope: stable, marginally stable, and actively unstable. Different paraglacial processes determine the state of the rock slope and can be grouped into three types: preconditioning, preparatory and triggering factors, as labelled in Figure 1. Preconditioning factors are static. These factors determine the rock slope stability before glacial conditions occur and set the ability of a rock slope to resist dynamic destabilising forces (McColl, 2012).

Depending on the existing stability, rock slope failure can be influenced or triggered by glaciation and deglaciation processes. Preparatory factors are dynamic and reduce the stability of a slope over time. Triggering factors can change the slope from marginally stable to unstable by one single event (McColl, 2012).

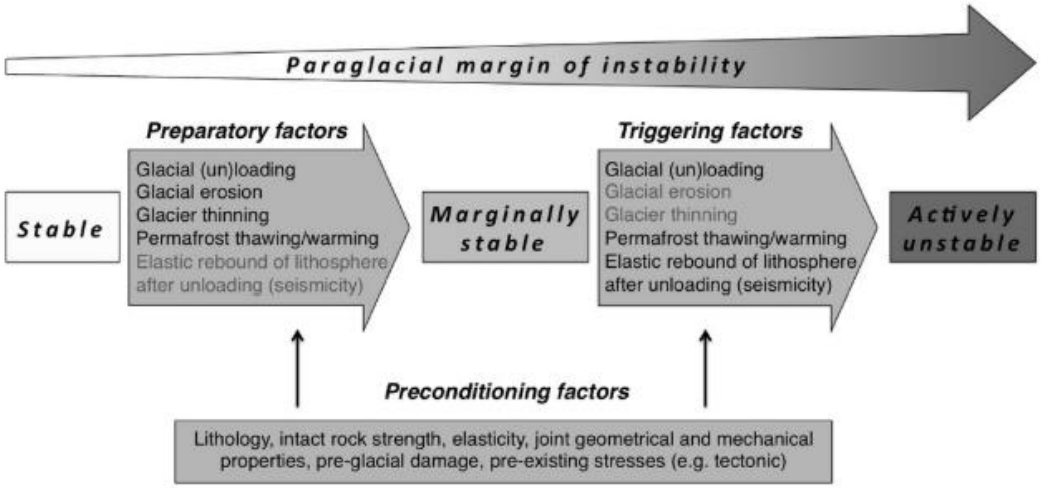

Figure 1 Preparatory, preconditioning, and triggering factors regarding to paraglacial rock slope stability taken from (McColl, 2012).

Lithology, rock structure (faults and fractures) and rock-mass properties like strength, deformability, foliation and joints and their orientation as well as their condition primarily control rock-slope stability. Glacier retreat and permafrost degradation are preconditioning rock slopes for failure by changing the in-situ stress conditions within a rock mass. The stress changes can be a result of topographic variations (change of surface geometry) by glacial and fluvial erosion, e.g. loading and unloading by ice, or changing hydro- and cryostatic pressure and thermal stresses by melt water infiltration or changes in subglacial temperatures. Conditioning processes occur in response to these changes and reduce the cohesive and frictional strength of a rock mass. That can happen due to the reactivation and dilation of existing fractures, propagation of new fractures, yielding of rock bridges or interlocking asperities, brittle-ductile block deformation, reduction of cohesive ice contacts and increased weathering (Krautblatter & Leith, 2015).

2.3 Mechanical processes

Rock slope glaciation and deglaciation imposes mechanical stress cycles on underlying bedrock and changes the in-situ stress field in the initially stable valley slopes. Induced mechanical stress changes can lead to elastic and inelastic deformations. The stress field redistribution can support the propagation of new fractures. Highly persistent discontinuity planes develop which finally can contribute to rock slope failure. Furthermore, stress redistribution can lead to slipping along existing joints, the degradation of asperities as well

as to smoothing of discontinuity surfaces due to shearing. These processes constitute rock slope damage and rock mass strength degradation conditioning slope instabilities (Hugentobler *et al.*, 2020).

2.3.1 Rock stress redistribution and jointing

Paraglacial slope failure surfaces are controlled by joint distributions. Joints weaken the rock mass, provide failure surfaces, and provide pathways for water and additional surface areas for weathering processes. Tectonic stresses are the most common cause of stress-induced rock mass jointing, usually forming two vertical orthogonal joint sets. But discontinuities can also have another origin and develop because of glaciation and deglaciation causing mechanically a redistribution of the in-situ stress pattern within a rock slope. High horizontal to vertical stress ratios lead to fracture propagation (McColl, 2012).

High horizontal versus vertical stress ratios can develop due to different processes as illustrated in Figure 2:

- Glacial oversteepening

Glacial erosion leads to changes in the slope geometry. It can produce deep valleys and oversteepened rock slopes. This process increases the self-weight (overburden) and shear stresses within the slopes. High stresses develop parallel to the steep rock slope (McColl, 2012).

- Glacial erosion of overburden

Glaciers can change the major principal stresses with the removal of overburden material. The erosion can release vertical stresses in the rock slope if the slope-parallel stresses remain at the same level due to lateral confinement of the surrounding rock mass. High horizontal to vertical stress ratios evolve. Glacial erosion may increase the stresses above a critical value but it also may expose (old) rock-mass defects of pre-glacial origin that are oriented in a way that failure becomes kinematically feasible (McColl, 2012).

- Stress release due to glacier unloading

The removal of confining glacial ice can cause a rebound of crustal material. Stresses normal to the rock slope decrease and lead to stress release. Fractures in the near-surface rock can develop, oriented parallel to its surface. These joints create potential failure planes for mass movements (McColl, 2012).

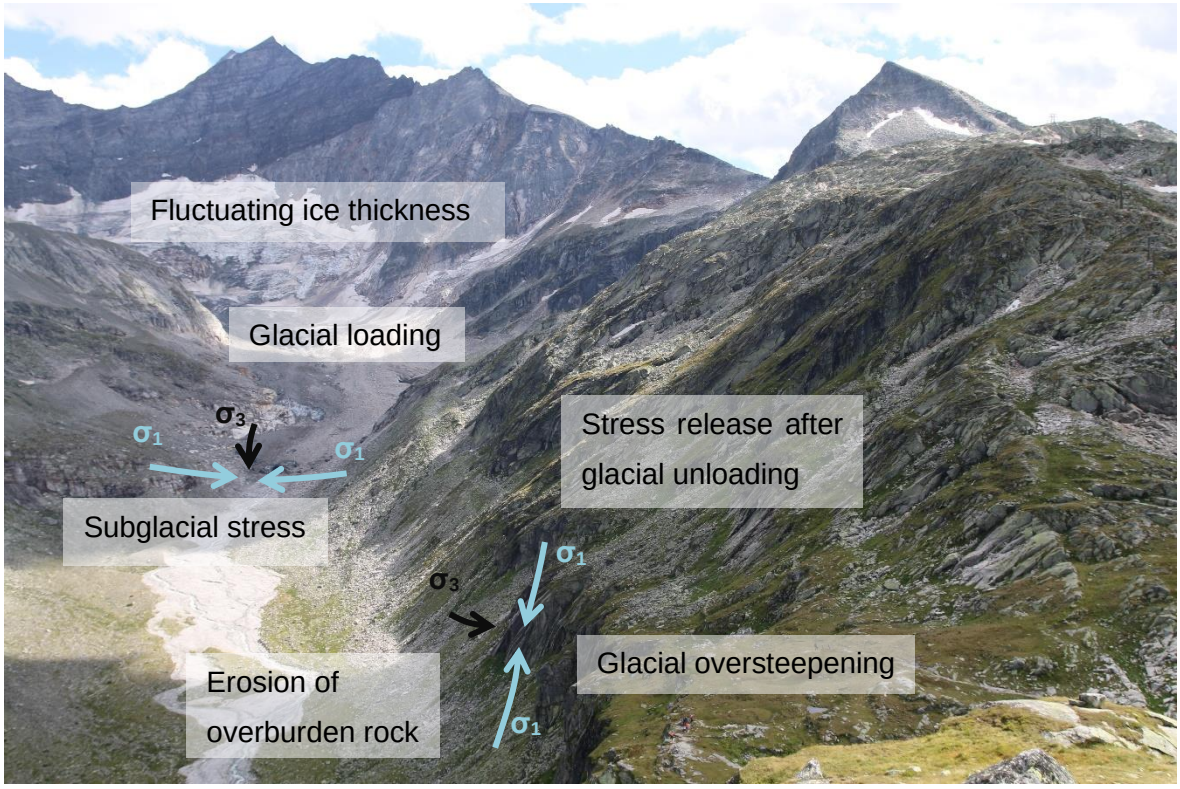

Figure 2 Mechanical processes leading to a stress field redistribution within the rock mass.

2.3.1 Glacial debuttressing

A slope is supported by normal stresses acting on the slope surface by the glacier ice through the static self-weight loading or the active flow of ice against the slope (Deline *et al.*, 2015). Glacial debuttressing describes the removal of this load and loss of slope support. Firstly, this mechanism creates a free space for the rock mass to move in and secondary, it can reduce the stability of the slope by removing the buttress of the mountain (McColl, 2012). However, (McColl, 2012) states that glacial debuttressing may not be sufficient to cause rock slope failure. Glaciers may not be able to buttress a slope, because of its ductile and highly viscos properties.

After simulations of (Grämiger *et al.*, 2018), glacial cycles as purely mechanical loading and unloading are of relatively low damage. Though ice fluctuations may increase the efficacy of fatigue processes. During the first deglaciation, bedrock erosion may cause significant damage and as a result the already weakened rock slope is more susceptible to potential failure. Furthermore, the stress conditions within a slope reach a critical state for the first time.

2.4 Hydrological processes

Repeated glacial cycles change the hydrological boundary conditions, which can lead to

hydro-mechanical rock slope damage. High water pressures beneath glacial ice affect the groundwater table in valley rock slopes over long time scales. The susceptibility of a slope failure triggered by hydrological conditions, depends on the strength, the hydraulic conductivity and the flow regime within the slope (Grämiger *et al.*, 2020).

Referring to modelling results of (Grämiger *et al.*, 2020) annual groundwater changes do affect effective stresses and therefore joint apertures, resulting in expansion and contraction of the rock mass. Annual groundwater changes because of seasonal snowmelt infiltration and additional changes in hillslope hydrogeology, result in a higher damage during glacier cycles.

The anisotropy of hydraulic permeability increases when it's frozen. Varying permeability in a rock mass can lead to build up pressure in discontinuities (Krautblatter *et al.*, 2013). Excess joint-water pressure is a potential trigger for rock slope failure. The water present in a rock joint exerts a hydrostatic pressure (if not flowing) and seepage pressure (if flowing) on the walls of the joint and an 'excess' pressure when the water pressure in the joint is greater than the water pressure in the surrounding (low-permeability) rock mass. High joint-water pressures develop where water inflow is larger than the outflow. Less outflow can be due to freezing condition in the joint network at slope surfaces. Water at the joint opening may freeze and as a result cannot drain and water pressure raises. Furthermore, a higher amount of water can infiltrate the rock slope caused by heavy rainfall events or increased snow melt (McColl, 2012). In fractured strong rock like granite, water movement is controlled by discontinuities because of the difference in permeability. Therefore, hydraulic conductivity can strongly vary with changing fracture characteristics, like frequency, orientation, aperture, interconnectivity, and persistence, etc. (Hugentobler *et al.*, 2020).

2.5 Thermal processes

Glacier retreat and advance cause subsurface temperature changes, which lead to thermo-mechanical stresses in the bedrock, generating damage to the rock mass. According to modelling results of (Grämiger *et al.*, 2018), long-term temperature changes on a glacial time scale affect the subsurface temperature regime of paraglacial valleys to depth exceeding 100 m. Damage induced by annual temperature changes is restricted to the upper 10 m.

After the glacier disappeared, the rock surface is exposed to direct atmospheric forcing (Figure 3) in terms of temperature variations for the first time, which causes strong thermo-mechanical stresses. The transition is termed as a paraglacial thermal shock and defines one single stress event elicited by a large and sudden temperature change (Grämiger *et*

al., 2018). It can produce deformations within the rock mass if the temperature-induced internal stresses suddenly exceed the capacity of the brittle material. These typically cut across pre-existing microcracks or crystal boundaries, contrary to thermal fatigue. A thermal shock can only occur if a specific rate of temperature change is exceeded and a suggested minimum rate is ≥ 2 °C/min. The fatigue behaviour of rock depends on factors like the duration of the rate of change, rock properties and the size of rock surface (Messenzehl, 2018).

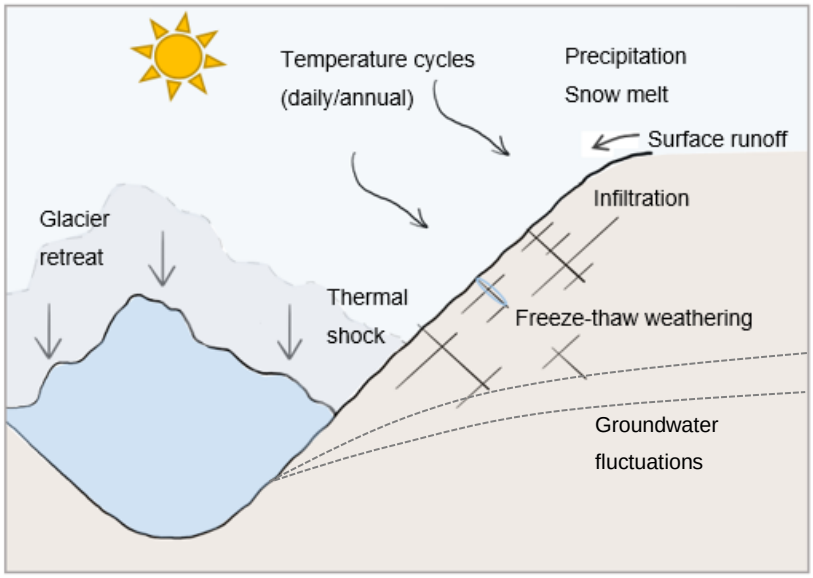

Figure 3 Thermal and hydrological processes after deglaciation. Modified from (Hugentobler et al., 2020).

After deglaciation, the rock slope is exposed to short- and long-term temperature cycles. The constant thermal regime during glaciation changes to diurnal and annual temperature variations, which induce significant thermomechanical stresses to paraglacial rock slopes and might be a reason for increased rockfall activity. Seasonal temperature cycles drive progressive failure in a critically stressed rock slope (Grämiger *et al.*, 2018). Whereas long-term temperature changes, as indicated by the modelling results of (Grämiger *et al.*, 2018), induce stresses sufficient for new rock fracturing. The highest damages occur during the first Holocene ice readvance while cooling of subglacial bedrock. Further, a temperature rise of a few degrees over thousand years after deglaciation can induce significant damage, even without glacier loading or unloading. As indicated by the modelling results, damage continues for ~ 3 kyr after the Egesen deglaciation with a temperature increase up to 4 °C during this time. Warming of bedrock after deglaciation can lead to postglacial rebound, the rise of earth's crust after the removal of glacial weight (Mey *et al.*, 2016). According to the modelling results of (Grämiger *et al.*, 2018) do long-term thermo-mechanical effects generate between 15 % and 19 % new damage (compared to the initial damage field) and annual thermo-mechanical cycles result in 10 % to 11 % new damage. Compared to a purely mechanical model described by glacier loading cycles only result in low new damage (1 %). Glacier fluctuations can produce considerable damage. Annual thermo-mechanical

cycles already induce incremental damage but thermal effects (long and short term) are most significant in conjunction with glacier loading cycles. (Draebing *et al.*, 2017) declared that thermal changes cause stresses sufficient for slow subcritical crack growth, depending on the moisture content. The involvement of meltwater by means of the transition from snow-covered to snow-free conditions may play an important role.

2.5.1 Cryogenic Processes

Cryogenic stresses develop due to the phase transition from water to ice and the corresponding volumetric expansion. They develop by ice segregation processes, which can lead to crack opening and propagation of pre-existing joints. Ice erosion or ice relaxation decline cryogenic stresses and result in crack closing (Draebing *et al.*, 2017). Ice pressure induced by volumetric expansion could derive stresses up to 207 MPa (Krautblatter *et al.*, 2013).

Ice segregation occurs in permeable and jointed bedrock and describes the migration of liquid water through a frozen fringe towards ice lenses in cracks, where it accretes. The water migrates along grain boundaries due to the temperature gradient-induced suction. Cryostatic pressure due to ice segregation requires a temperature gradient typically from -3 °C to – 6 °C and water supply (Krautblatter & Leith, 2015). Heaving pressures can cause crack propagation even in strong rocks like granite (Krautblatter *et al.*, 2013).

The repeated freezing and melting of water in rock masses is a process that may occur after permafrost degradation. Freeze-thaw weathering is most effective when there are regular fluctuations in temperature around the freezing point of water. It may extend and weaken the joints in pre-existing joint networks (McColl, 2012). These processes are only relevant in the upper part of the subsurface (< 10 m). With greater depth reduced temperature gradients and water availability, combined with increased normal load would prevent these processes (Krautblatter *et al.*, 2013).

Cyclic processes affect the rock slope either by hydro- or thermo-mechanical loading, whereas hydro-mechanical slope processes are thought to be more efficient. The modelling results of (Grämiger *et al.*, 2020) point out, that by comparing thermomechanical and hydromechanical paraglacial processes, glacial erosion and hydromechanical stress changes (especially annual melt infiltration cycles) are the most effective preparatory processes for rock mass damage during (de)glaciation. These mechanisms involve a pore pressure decrease, accompanied by an increase of effective normal stress, leading to fracture closure or a pore pressure increase causing fracture opening and a reduction of shear strength of a fracture.

(Draebing *et al.*, 2014) conclude that on a seasonal scale are two potential critical instability

time windows. One in early summer, where combined hydrostatic and cryostatic pressure cause a peak in shear force exceeding the shear resistance and one in autumn, where shear forces increase faster than the shear resistance. There might be increased damage owing to rapid refreezing and volumetric expansion of ice in discontinuities.

2.6 Spatial pattern of paraglacial rock slope failures

(Cossart *et al.*, 2008) suggest that major rock falls and avalanches are associated with areas bearing the highest decompression stresses. Their study showed that rock-slope failures are concentrated on lower valley-side slopes within the area occupied by ice at the Last Glacial Maximum, and that the locations coincide with zones of inferred high glacial loading stress. The study of (Leith *et al.,* 2010) shows that rockfall activity changes the position within the slope profile with time. It starts at the toe, where the maximum ice load resulted in highest erosion and stress redistribution (Messenzehl, 2018).
(Hartmeyer *et al.*, 2020) observed that rockfall activity is highest in recently deglaciated areas. 60 % of the rockfalls occurred in an area ten vertical meters above the present glacier surface and 75 % within twenty vertical meters above the glacier surface.

2.7 Permafrost

2.7.1 Definition

According to the International Permafrost Association (IPA) permafrost is defined as a ground (soil or rock and included ice or organic material) that remains at or below 0 °C for at least two consecutive years (van Everdigen *et al.*, 1998). A typical distinction is made between continuous permafrost in high altitudes, with a thickness of a few hundred meters, and discontinuous permafrost, the alpine permafrost in higher mountains, typically with a thickness of a few meters (Harris *et al.*, 2009).
The surface layer above the permanently frozen permafrost, is called the active layer. During the summer months the initially frozen ground is thawing. Due to seasonal temperature variations the thickness is changing, which depends on thermal properties of the subsurface. Furthermore, the thickness of snow cover has a high impact because of its insulating effect protecting the subsurface from solar radiation and air temperature variations (Dobinski, 2011).
The determination of permafrost in the subsurface is difficult considering that there is usually no evidence on the surface. Measurements need to be carried out with drillings or geophysical methods (Schrott *et al.*, 2012).

2.7.2 Stress changes due to permafrost thaw

In permafrost regions an increasing frequency and magnitude of rock slope failures is recognized since the end of the Little Ice Age (Draebing *et al.*, 2017), (Gruber & Haeberli, 2007). Rock slope stability is controlled by warming of the climate resulting from permafrost thaw. Although geologic and geometric conditions are most important for stability, permafrost can be an important element which is subject to change fast (Gruber & Haeberli, 2007).

Glaciation and deglaciation not only change the stress patterns within the rock mass, they cause also dynamic changes in glacier-permafrost interconnectivity. Changes in thermal, hydrological, mechanical, and chemical conditions in permafrost-affected bedrock can lead to rock slope failure. For example, due to meltwater infiltration into fractures, which provides a heat input, mechanical strength changes resulting from thawing bedrock, and new weathering conditions. At the surface where the protective ice cover disappeared rock weakening occurs. Mechanical properties of ice and water-saturated rock are highly susceptible to temperature changes when it's close to 0 °C (Krautblatter & Leith, 2015).

The presence of permafrost can increase shear stress due to changing hydrostatic pressure. Increase of hydrostatic pressure can be due to perched groundwater above permafrost bedrock (Fischer *et al.*, 2010). The permeability of frozen fissured rock is one to three magnitudes lower than of thawed rock. In addition, ice sealing of rock surfaces so that water cannot escape can increase hydrostatic pressures. Together with cryogenic weathering processes like ice segregation and volumetric expansion, stresses on the rock mass are elevated. At the same time thawing permafrost can decrease shear resistance of rock masses because it alters the mechanical behaviour of intact rock, crack propagation, and frictional processes of rock-rock contacts, rock-ice contacts, and ice/frozen fill-material (Krautblatter & Leith, 2015). (Krautblatter *et al.*, 2013) established a rock-ice mechanical model containing shear forces acting on the potential sliding plane and resisting forces provided by the frozen rock mass. The shear forces acting on a permafrost-affected bedrock which may lead to or resist slope failure are displayed in Figure 4.

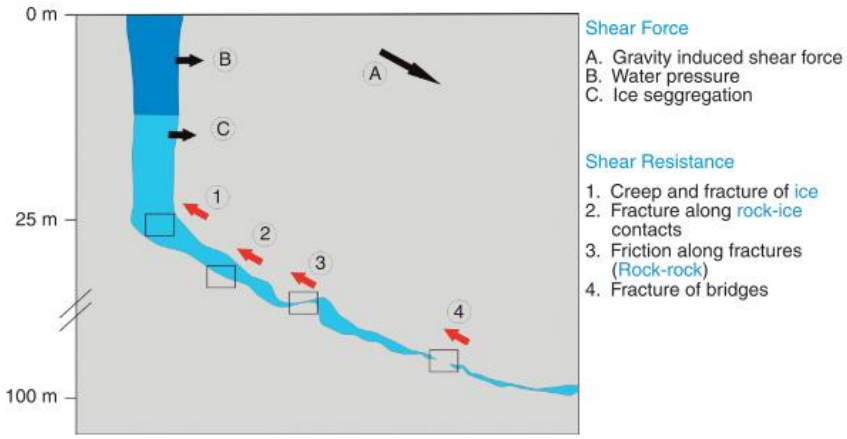

Figure 4 Shear forces and shear resistance acting on permafrost-affected bedrock. Taken from (Krautblatter & Leith, 2015).

Driving forces can be induced by the following three different processes in permafrost-affected bedrock: A. Gravity induced stresses due to the rock load and pre-existing tectonic stresses parallel to the shear surface, B. Hydrostatic pressure because joints are filled with water and C. Cryostatic pressure induced by ice segregation or ice expansion.

Restraining forces of ice-filled joints are induced by: 1. Creep and fracture of ice, 2. Failure of rock-ice contacts, 3. Friction of rough fracture surfaces while there is rock-rock contact, 4. Fracture of cohesive rock bridges.

The efficiency of processes controlling rock-slope stability changes with varying normal stress. As illustrated in Figure 5 ice-mechanical processes are more efficient in shallow depth and rock-mechanical processes play a major role for deep-seated rock-slope failures in warming permafrost rocks. Water pressure can induce stresses at all depths. For ice segregation exists a ‘shut off’ pressure that is equivalent to 20 m overburden. Below this depth it does not have an effect anymore. There is the same limit for rock-ice detachments and ice fracturing. These processes are dominant if the shear plane is below 20 m. On the other hand, rock friction and fracturing increase with higher normal stress and therefore with depth. The thresholds needed for fracture propagation along critical paths are often not reached in shallow depths (Krautblatter *et al.*, 2013).

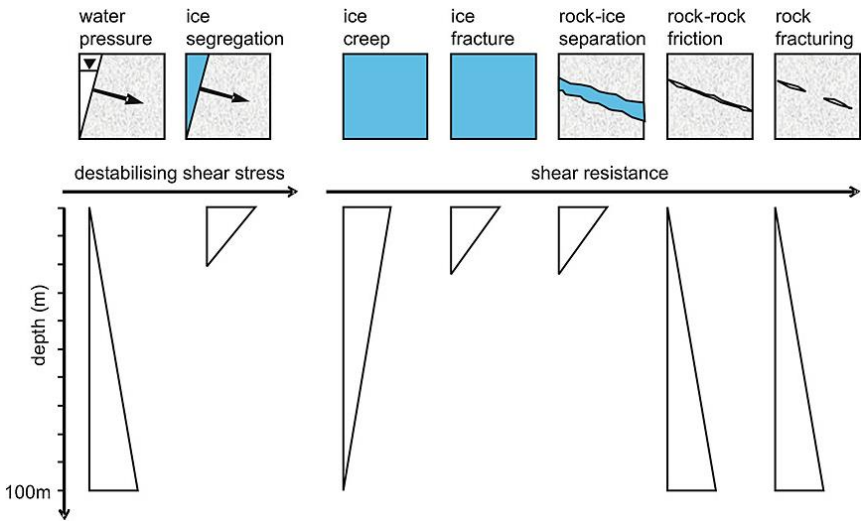

Figure 5 Changing efficiency of ice-mechanical and rock-mechanical processes with depth. Taken from (Krautblatter et al., 2013).

According to the results of laboratory experiments the friction of rock joints decreases by approximately 15 % without ice infill (Krautblatter *et al.*, 2013).

If the pore-water in high-altitude alpine rock remains permanently frozen as permafrost, the ice within the pores creates a more intact, stronger rock mass. After deglaciation, the permafrost level rises which reduces the strength of the rock mass that is left without permafrost (McColl, 2012). Therefore, the height of rockslides is mostly at the lower limit of the permafrost area, which is also a result of several studies in the Alps (Schoeneich *et al.*, 2011).

2.7.3 Permafrost in the Hohe Tauern Region

The distribution of permafrost is variable. (Schrott *et al.*, 2012) established a model of the permafrost distribution in Austria. They state that approximately 1600 km² of a surface in Austria is underlain by permafrost. In the Hohe Tauern mountain region, they expect extensive permafrost above 2500 m, exceeding the surface area of present glaciers, covering approximately 13 % of the entire area (Schrott *et al.*, 2012).

Permafrost occurrence in the Alps is influenced by different factors: climatic (air temperature and solar radiation), topographic (aspect and slope), and site-specific surface conditions (snow cover and duration, debris and boulder size). (Schrott *et al.*, 2012) determined a topoclimatic key, which assesses the probability of permafrost occurrence depending on the slope orientation and angle (Figure 6). They differentiate three different relief classes (rock slopes, steep slopes (> 11°) and slope foot-positions) which are subdivided into eight different aspects. As a rule of thumb, permafrost can be expected above 2500 m a.s.l. in northerly exposed slopes and above 3000 m a.s.l. in southerly exposed slopes. According to their modelling results of a simple scenario assuming a temperature increase of 1 and 2

K, the permafrost occurrence would shift 195 and 390 m in altitude. This would result in a potential permafrost degradation of 70 and 90 % (Schrott *et al.*, 2012).

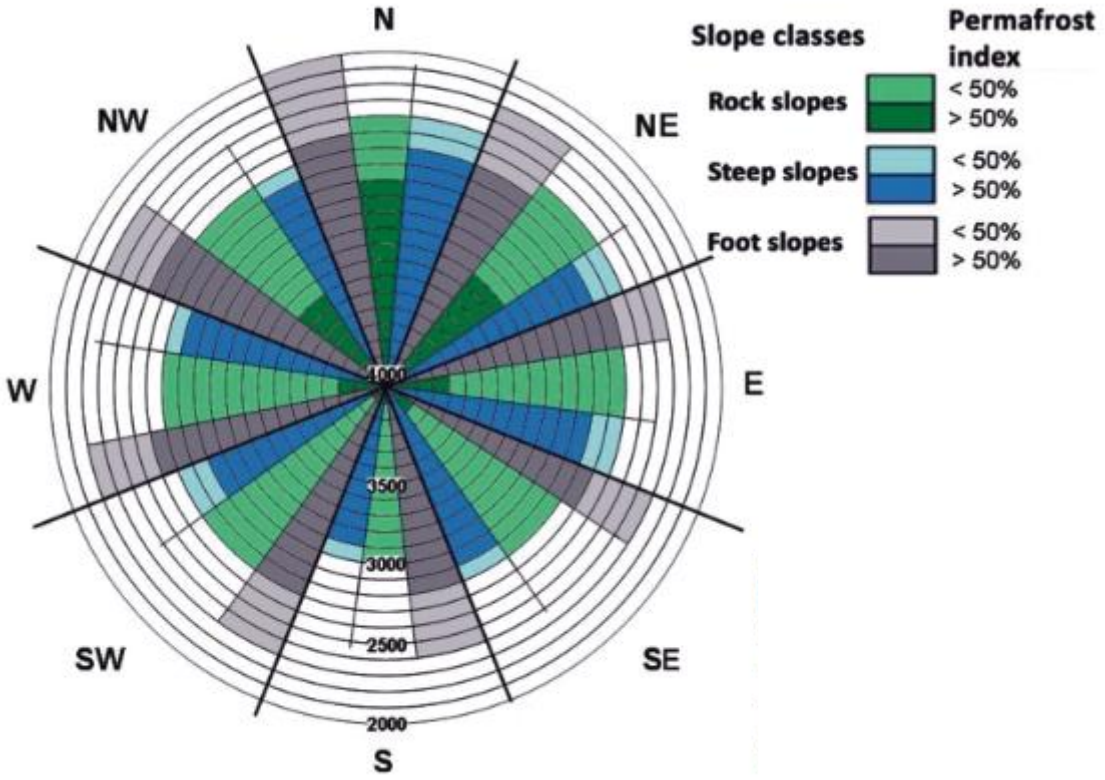

Figure 6 Topoclimatic key for permafrost occurrence in the Hohe Tauern region. Taken from (Schrott et al., 2012).

2.7.4 Reaction Time

The stability of rock slopes affected by changing thermal conditions changes on different timescales. On a scale of several decades there is an increased rockfall activity and on an annual scale increased rockfall activity during hot summer month is recognized (Draebing *et al.*, 2014).

The temporal pattern at permafrost rockwalls depends on different time-dependent ice-mechanical responses. The first rapid response directly after deglaciation occurs without rockfalls. This may be due to the increasing permafrost thickness after ice removal due to the bedrock exposure to cold atmospheric temperatures. Freezing of absorbed water in micro-cracks may result in a temporally increase of the slope stability and in a slope equilibrium. The second rapid response to the first thawing impulse occurs in form of creep and deformation of ice along existing failure planes. The time needed until this first failure occurs may be in a range of days to several decades. After the first rockfall peak, the

mechanical response of permafrost influenced bedrock to further warming might be slowly dominated by fracture propagation and failure of rock bridges. The final adjustment to non-glacial conditions might be after hundreds of years. At this point the bedrock has adapted to non-frozen strength conditions or the slope angle has adapted to the equilibrium angle of permafrost-free rock slopes (Krautblatter & Leith, 2015).

2.7.5 Permafrost induced rock slope failures

Research about the effects of permafrost on rock slope stability increased in the past 20 years. Mapping, geothermal monitoring, geophysical ground surveys, numerical modelling, energy balance measurements and laboratory tests were carried out for a better understanding of thermal, hydrological and mechanical processes of permafrost rockwalls (Deline *et al.*, 2015). Several studies about the influence of degrading permafrost on rock slope stability as a consequence of climate warming were performed (Krautblatter & Leith, 2015) (Draebing *et al.*, 2017) (Fischer *et al.*, 2010) (Gruber & Haeberli, 2007).

In the last decades, several large rock slope failures with volume of a few million to tens of million m^3 occurred. At the Pizzo Cengalo north-east oriented rock face a recent rock mass (3 million m^3) failure in 2017 was favoured by permafrost conditions (Walter *et al.*, 2020). At another location in switzerland, the Randa rock slope instability was also affected by retreating permafrost. Two rockslides occurred in April and May 1991 with a total amount of 30 million m^3 failed rock mass (Gischig *et al.*, 2011).

Additional to these large rock slope failures the amount of smaller rockfalls with volume from a few hundred to tens of thousands m^3 is significantly rising (Deline *et al.*, 2015). After a study at the Mont Blanc massif an increased number of rockfalls can be recognized. (Ravanel *et al.*, 2017) showed a strong correlation of an increase in the frequency of rock falls and the rising mean annual air temperature (Figure 7). Rockfalls in permafrost areas occur mainly in the summer month. The rock fall frequency was observed to be higher during the hot summers of 2003 and 2015. 97 % of the rockfalls detached from permafrost-affected rock-walls and mostly from the lower limit of the permafrost. The authors suggest three potential triggers related to permafrost degradation: active layer thickening, hydrostatic pressure caused by thaw or rainfall events, and advective heat transport at depth by water percolation along discontinuities (Deline *et al.*, 2015).

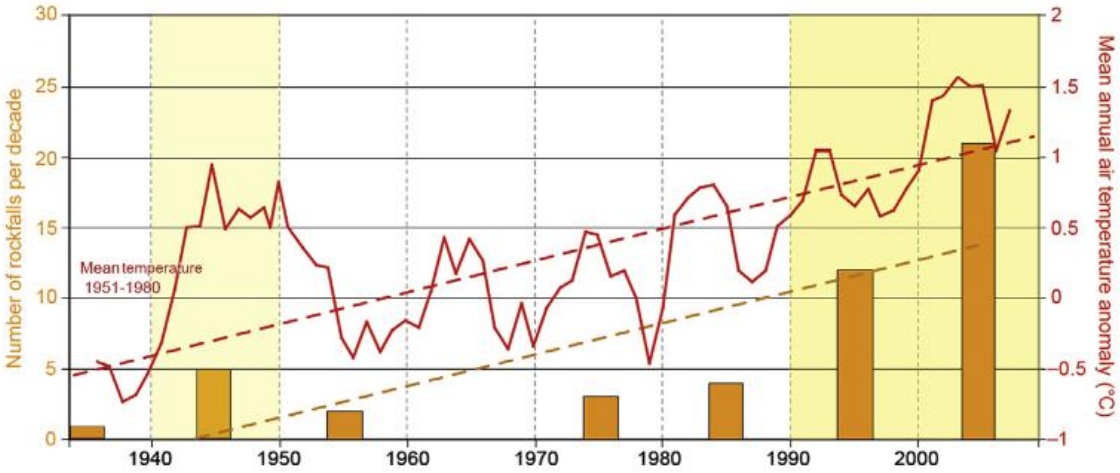

Figure 7 Mean annual temperature in Chamonix and number of rock falls per decade in the Mont Blanc massif, France (Deline et al., 2015).

3 Rock mass characterization

3.1 Anisotropy of rock masses

A rock mass is typically heterogeneous and anisotropic. To be able to evaluate the engineering behaviour the properties of the following three rock mass elements need to be determined: 1. intact rock, 2. discontinuities (joints), and 3. fault zones. Intact rock is part of a rock block not cut by any fracture. It can be characterised by its physical characteristics like mineral composition, colour, texture, grain size and porosity and by its mechanical characteristics like strength, hardness, brittle behaviour or plasticity (Singh & Goel, 1999).
Rock slope stability highly depends on the three-dimensional structures of discontinuities. Their geometrical and mechanical properties need to be characterized in order to understand the overall rock mass behaviour. The key geometrical properties of discontinuities are orientation, spacing, roughness and persistence (Hudson, 1989). These and other are illustrated in Figure 8.

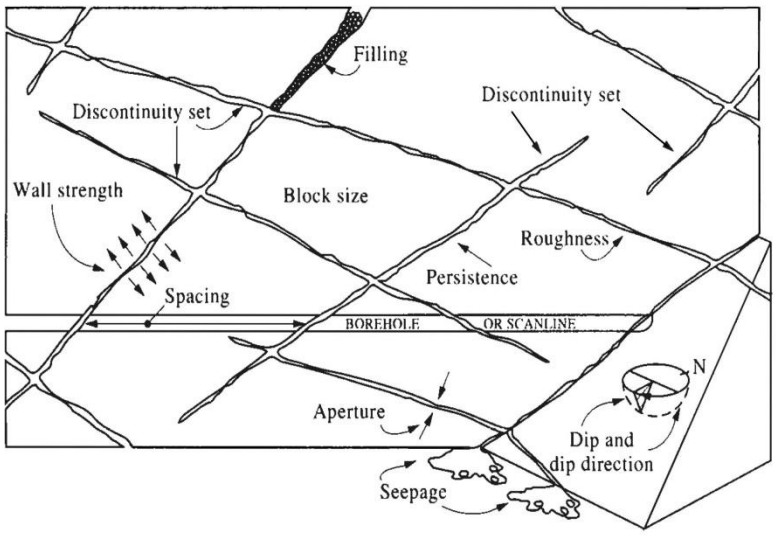

Figure 8 Rock mass geometrical properties taken from (Hudson, 1989).

3.2 In-situ stress field

The in-situ stress field highly affects the evolution of joints, erosion processes and the deformation behaviour of a rock mass. The description of the stress distribution can therefore help to determine site and mechanism of joint opening and landform development of rock slopes. It is described by the orientation and magnitude of the vertical and horizontal

component of the principal stresses. The major principal stress σ_1 is always parallel to the surface and equal to the weight of the overburden rock.

$$\sigma_1 = \gamma_r H \quad (1)$$

Where γ_r is the unit weight of the rock [MN/m^3] and H [m] is the depth. Equation 1 indicates that the horizontal stress magnitude σ_1 increases linearly with depth. The minor principal stress σ_3 acts perpendicular to the rock slope in vertical direction and is dependent on the lateral confinement by the surrounding rock mass (Wyllie & Mah, 2005).

The in-situ stress field defines the ratio between the horizontal and vertical stress and is controlled by the slope topography and discontinuity pattern within the rock mass. The long-term geological, tectonic, and glacial history also have high influence on the stress trajectories (Hencher *et al.*, 2011), (McColl, 2012). High horizontal to vertical stress ratios can lead to the development of sheeting joints (Hencher *et al.*, 2011). Brittle fractures develop with release of the internal rock stresses. There are four major sources of stress in a rock mass at shallow depth: residual, gravitational, tectonic and thermal (Augustinus, 1995). The in-situ stress state influences the type of fracturing that occurs, creating zones of weakness, which are prone to glacial erosion processes. Deglaciated mountains owe their form to the stress patterns in the rock and the fractures that develop. The in-situ stress field influences destabilization, modification, and development of the glacial valley cross-profiles. High rock mass strength allows the maintenance of high stresses and therefore steep slopes in strength equilibrium. Gravitational stress in combination with tectonic and thermal stress influence rock slope failure and so may control the location and direction of the modifying geomorphic processes (Augustinus, 1995).

3.3 Discontinuity persistence and intact rock bridges

A rock bridge is defined as an area of intact rock separating discontinuities in rock masses. As illustrated in Figure 9 a, rock bridges usually occupy a part of the planar joint plane. This is defined as the areal discontinuity persistence, reflecting the three-dimensional nature of discontinuities. In Figure 9 b the linear persistence is shown, where the rock bridges are coplanar to the joint plane (Shang *et al.*, 2018).

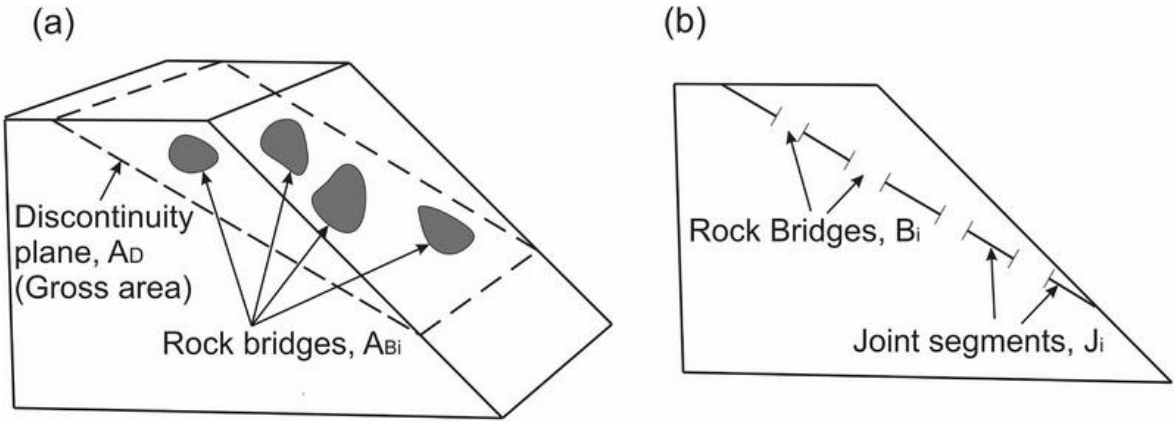

Figure 9 Definitions of rock discontinuity persistence. (a) Persistence as a fraction of joint surface area and (b) persistence as a fraction of joint length. Taken from (Shang et al., 2018).

Rock slope stability is controlled by rock bridges. They produce a strength reserve by adding cohesion and tensile strength of an incipient failure surface, which must be destructed before failure occurs (Shang *et al.*, 2018). The shear strength of intact rock is typically two or more orders of magnitude greater than the shear strength of pre-existing discontinuity interfaces (Kemeny, 2005). A small content of rock bridges (1% - 3%), favourably distributed within the rock mass can significantly increase the stability of a slope (Tuckey, et al., 2016). The stability can be reduced over time by progressive damage induced by effective stress concentrations. It is essential to take step-path failures into account when evaluation rock slope behaviour. However, the measurement of rock bridges within the rock mass is difficult, because they are not visible prior to failures like rock falls (Shang *et al.*, 2018).

3.4 Fracture propagation

3.4.1 Step-path failure of rock slopes

For rock slope stability assessment, it is essential to know if the discontinuities will connect with each other (Xu & Li, 2019). Step-path failure is a typical mechanism if intermittent joints are present. Crack propagation and coalescence or connection of different discontinuities may lead to the instability of a rock slope (Huang *et al.*, 2014).

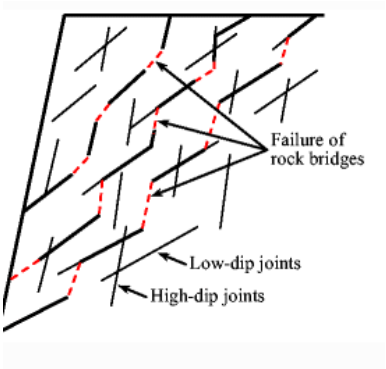

Figure 10 Slope with intermittent joints, which may be connected because joint propagation and resulting rock bridge failure. Taken from (Huang et al., 2014).

Tensile cracks are generated mostly from the tips of joints connecting pre-existing discontinuities as illustrated in Figure 10. The step-path failure in a rock slope is a progressive process, where rock bridges fail one by one from the bottom up under the action of gravity (Huang *et al.*, 2014).

If the rock slope is subjected to uniaxial compression little defects in the rock mass can lead to fan-shaped fracture structures. Due to bending of the rock, tensile stress increases which leads to progressive fracture propagation. The connection of these little fan-shaped structures can result in one persistent longitudinal joint in the direction of the maximal stress (or: normal to minimal stress). Crack propagation results from stress concentration around defects. These defects may result from the rock loading history. Wing cracks are localized crack patterns propagating along the most compressive stress direction from the flaw tips as illustrated in Figure 11. A tensile nature is associated to wing cracks, whereas secondary cracks arise from a shear mechanism (Duriez *et al.*, 2016).

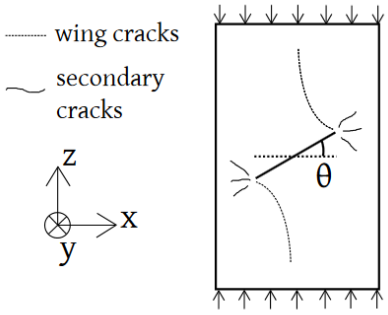

Figure 11 Compression of a pre-cracked sample. Taken from (Duriez et al., 2016).

When there is one isolated flaw, step-path failure is more likely to be caused by wing cracks that initiate at the tip of a flaw. They propagate along a curvilinear direction becoming roughly parallel to the maximum compression. Wing cracks can initiate at a pre-existing flaw when the inclination angle is less than 15°, secondary cracks usually form at the tip of a pre-existing flaw in the horizontal direction. The closer the inclination angle is to 90°, the harder the secondary cracks initiates. (Xu & Li, 2019) observed in laboratory experiments that there are three possible directions of secondary crack propagation: 1) in the horizontal

direction, 2) coplanar or quasi-coplanar to the pre-existing flaw, 3) in the direction perpendicular to that of wing crack propagation. The propagation of secondary cracks varies. Paths of the wing cracks are smooth whereas the paths of secondary cracks are sinuous and have many kinks, the surface is often uneven and rugged. Once a secondary crack connects with another secondary crack or wing crack, spalling occurs (Xu & Li, 2019).

3.4.2 Glacial erosion

Glacial erosion are processes including abrasion, quarrying (or plucking), incision of meltwater channels, and chemical weathering or dissolution. Bedrock surfaces polished through abrasion are characteristic of formerly glaciated landscapes (Leith *et al.*, 2014b).
Abrasion and quarrying are the dominant mechanisms by which glaciers erode bedrock. Quarrying happens if the bedrock is sufficiently cracked so that rock fragments can be dislocated by the sliding glacier ice. The pre-existing fracture networks strongly control glacial quarrying process and the destruction of intact rock bridges is the principal subglacial fracturing mechanism (Leith *et al.*, 2014b). Therefore, slow (subcritical) crack growth under glacial loading is thought to be an essential mechanism before quarrying. As proposed by (Leith *et al.*, 2014b), the bedrock stresses beneath a glacier are sufficient enough to induce fracturing.
Roches moutonnee is a typical bedrock formation in glaciated regions. They usually consist of a smooth, rounded back on the uphill side of the rock mass, whereas the downhill face is rough and stepped. Joints are usually perpendicular to the glacier flow direction and only rarely parallel to it. If a glacier flows over a large rock mass it does not immediately re-conform (Carol, 1947). Therefore, cavities are built on the lee side of a rock mass, where the ice separates from the rock as illustrated in Figure 12. Large stress differences evolve between the normal stress that ice and water apply on top and the lee surface of the rock mass. The deviatoric stresses are highest on the lee side of the rock mass where it leads to increased fracturing (Hooyer *et al.*, 2012). Freeze-thaw processes may also play a dominant role on the downhill face of the rock mass. The temperatures in the subglacial cavities are close to freezing-point. Therefore it seems probable that melt water infiltrates into the discontinuities on the downhill side, where it refreezes after pressure release. The volumetric expansion leads to further fracture propagation and rock burst (Carol, 1947).

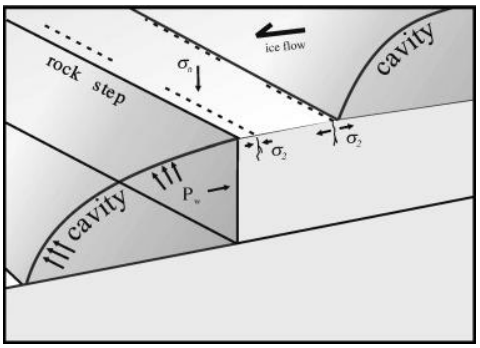

Figure 12 Geometry of a glacier bed with water-filled cavities in the lee of two-dimensional bedrock steps. Subcritical crack growth of small, isolated cracks results from stress differences between the water pressure in the cavity and the normal stress exerted by the overlying ice. Taken from (Hooyer et al., 2012).

The orientations of potential quarried surfaces reflect those of principal stresses. The least principal stress (least compressive or more tensile), σ_2 is compressive and roughly parallel to the glacier flow direction (Hooyer *et al.*, 2012). The model of (Leith *et al.*, 2014b) suggests that quarrying is relevant across a region close to the axis of the valley.

3.5 Sheeting joints

Sheeting joints are extensive fractures that develop parallel to natural slopes and divide large rock masses into thin layers. They generally develop in shallow depths. They are rough and wavy, which contributes to their shear strength and improve their stability. Sheeting joints can often be traced for hundreds of metres. Due to their orientation and long persistency without rock bridges, the joint planes are often favourably located for rock slope failures. Therefore they play a dominant role for rock slope stability assessments (Hencher *et al.*, 2011). Following terms are synonymously used: exfoliation joint, pressure-release, unloading joint, post-uplift joint, Talklüftung (Ger.) und Talbankungen (Ger.). Whereas, sheeting and exfoliation joints are preferably used, because the mechanical process of formation is still discussed (Ziegler *et al.*, 2013). Sheeting joints are extensive fractures that develop parallel to natural slopes and divide large rock masses into thin layers. They generally develop in shallow depths. They are rough and wavy, which contributes to their shear strength and improve their stability. Sheeting joints can often be traced for hundreds of metres. Due to their orientation and long persistency without rock bridges, the joint planes are often favourably located for rock slope failures. Therefore they play a dominant role for rock slope stability assessments (Hencher *et al.*, 2011).

Sheeting joints can form in response to the evolution of high stress ratios with high compressive stresses parallel to the surface and weak compressive stress (or tensile stress) perpendicular to the surface. These can develop because of erosion or glacial unloading and the associated reduction in vertical compressive stress (Martel, 2017). While

the maximum compressive stress is reoriented to run parallel to the topographic surface, for example due to oversteepened slopes after glacial erosion. The mechanism is similar to a uniaxial compressive strength test where tensile fracture propagates parallel to the maximum principal stress (σ_1) (Hencher *et al.*, 2011). They develop parallel to stress trajectories that curve under valleys as illustrated in Figure 13 (Hencher *et al.*, 2011). Sheeting joints develop in many kinds of high-strength rocks, such as granite and gneiss, because the rock slope needs to withstand large differential stress ratios (Hencher *et al.*, 2011).

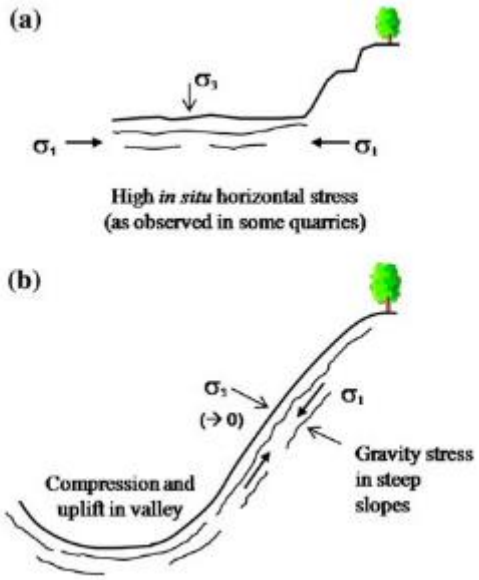

Figure 13 Stress conditions for the formation of sheeting joints in steep slopes and relatively strong, unfractured rock. (Hencher et al., 2011)

Sheeting joints occur between valley bottoms and mountain crests within glacial landforms. Thermal stresses contribute to the development of sheeting joints very near the ground surface. They reflect a fracture process involving the shape, slope, and scale of the topography, the regional horizontal stress, the effect of gravity, and groundwater pressure (Hencher *et al.*, 2011).

3.5.1 Characteristics

Sheeting joints rarely occur individually but in collections that exhibit systematic patterns of spacing and overlap. With increasing depth beneath the surface, the spacing, length and radii of curvature increases (Martel, 2017). Sheeting joints commonly display a plumose surface texture consisting of arrest lines (ribs) and hackles. They typically cut all other geologic structures in a rock mass, such as foliation, geologic contacts, and other fractures (Martel, 2017). Sheeting joints that develop in steep rock slopes where they owe their origin

to gravitational stresses are typically rough and wavy. They often show broad waves with an amplitude of approximately 1 to 10 m. The fractures often terminate against pre-existing cross joints or intact rock. Steps are due to intersections with cross joints as illustrated in Figure 14 (Hencher *et al.*, 2011). They enable water flow inside the rock mass because of their typical immense length, large aperture and connection to other fractures that result in integrated hydraulic systems. It may allow water pressures to develop rapidly. Additionally, water flow may reduce roughness and waviness of sheeting joints. Water pressure in the joint network may reduce effective stresses, which can lead to slope failure along sheeting joints. This failure may occur as translational sliding (Hencher *et al.*, 2011).

Sheeting joints can be classified by following features: orientation to current landscape surface, joint surface weathering, glacial polish, spacing, visible length and joint set curvature. For stability assessment key factors are geometry (orientation and roughness), shear strength and potential for ingress and development of adverse water pressure (Ziegler *et al.*, 2013).

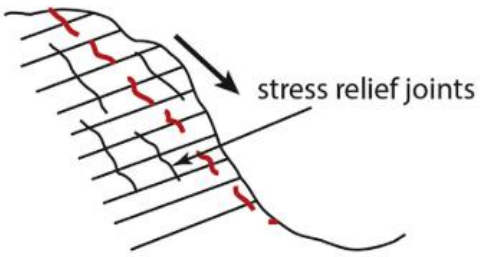

Figure 14 Failure along stress relief joints (Stead & Wolter, 2015).

3.5.2 Difference to other joints

Sheeting joints have similar geometric, textural and kinematic properties to other joints. The most apparent difference is that they open near to and subparallel to the topographic surface (Martel, 2017). Parallelism between fracture orientation, glacier bed topography and former direction of glacier movement is an important indication of joint formation trough paraglacial stress release (Cossart *et al.*, 2008). In addition, they can exceed the typical dimensions of many other joints. Large apertures, which are typical for sheeting joints, are rarely observed along other kinds of joints. Furthermore, the ends of sheeting joint traces typically do not have “tail cracks” commonly observed near the ends of sheared joints and faults. Sheeting joints may occur characteristically curved, by forming a splay-shaped pattern independent from the alignment of natural joint sets (Martel, 2017).

Tectonic joints are generally planar, show smooth to slightly rough joint surfaces, slickensides and have a prominent hydrothermal mineralisation. The orientation is

independent from topography and the joints have non-uniform aperture. The characterization after the parallelism to the surface can be challenging as the joint might change orientation with respect to the slope surface after fluvial, glacial and gravitational erosion (Martel, 2017).

3.6 Kinematic analyses

Kinematic analyses are useful to identify joints that are critical for mass movements, the potential failure mode, the shape of block release and the fall direction (Wyllie & Mah, 2005). To understand the kinematics of the unstable rock mass, stereographic analysis of the structural data can be implemented. The method assumes that discontinuities are cohesionless, dry and fully persistent and the blocks are rigid. Lateral constraints and stresses on the block are not considered. The method indicates what kinematic modes are feasible for a certain discontinuity plane orientation, their friction angle and rock slope orientation (Gischig *et al.*, 2011).

The three most common structurally controlled failure mechanisms as illustrated in Figure 15 are planar sliding, wedge sliding, and toppling (Wyllie & Mah, 2005).

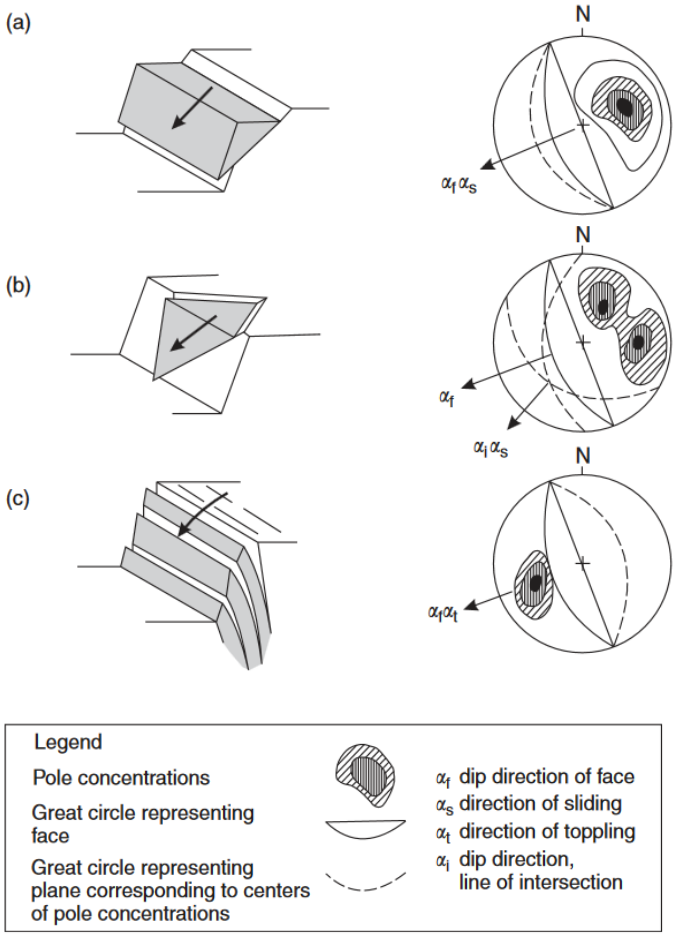

Figure 15 Main types of block failure. a) plane failure on a persistent plane dipping out of the slope surface and striking parallel to the face. b) wedge failure on the intersection of two planes; c) toppling failure with discontinuities dipping steeply into the face. Taken from (Wyllie & Mah, 2005).

Planar sliding is possible if a potentially unstable block is formed by a single persistent plane, which daylights on the slope surface and dips at a flatter angle than the face: $\Psi_P < \Psi_S$. The daylight envelope can be used in a stereonet to quickly identify potentially unstable blocks. The dip direction also limits the critically oriented discontinuities prone to planar sliding. The failure is not possible if the dip direction of the discontinuity differs from the dip direction of the face by more than 20°. Therefore, the block will be stable if $|\alpha_P - \alpha_S| > 20°$, because there will be an increasing thickness of intact rock at one end of the block which will have sufficient strength to resist failure. On the stereonet these restrictions of the dip direction are marked by two lines which designate the lateral limits of the daylight envelope. The kinematic analysis of wedge failures is similar to that of plane failures. Sliding is possible if the line of intersection of two discontinuities daylights on the face: $\Psi_i < \Psi_S$. The direction of sliding is less restrictive than that of plane failures on account of two planes forming release surfaces. The daylighting envelope for the line of intersection is wider than that for planar failures.

Toppling failure occurs if the discontinuities' dip direction is dipping into the slope within 10° of the dip direction of the slope surface. The rock mass is prone to fail if a series of rock layers are formed parallel to the slope surface and if the discontinuities are steeply oriented slip between the layers may occur. Slip only occurs if direction of the applied compressive stress is at angle greater than the friction angle ϕ_j of the discontinuity surface. Toppling failure occurs on planes with dip Ψ_P when the following condition is fulfilled: $(90° - \Psi_S) + \phi_j < \Psi_P$ (Wyllie & Mah, 2005).

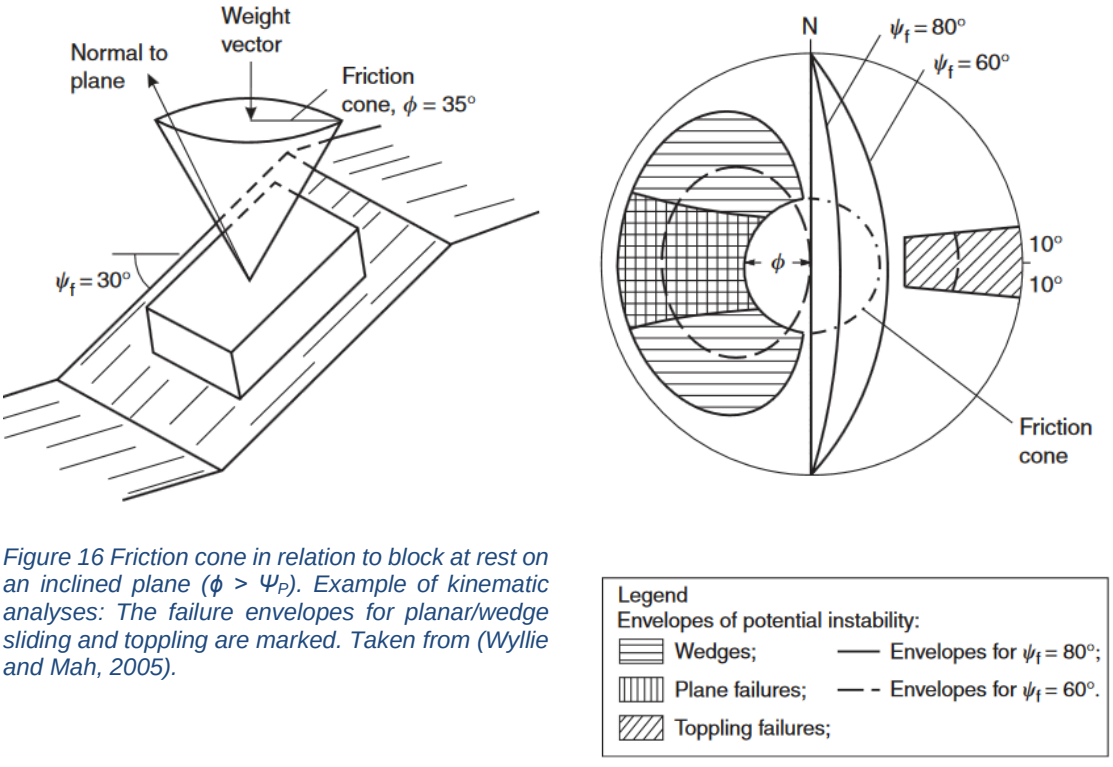

Figure 16 Friction cone in relation to block at rest on an inclined plane ($\phi > \Psi_P$). Example of kinematic analyses: The failure envelopes for planar/wedge sliding and toppling are marked. Taken from (Wyllie and Mah, 2005).

If a rock block is kinematically permissible, stable conditions can be determined by using a friction cone. This analysis assumes that the sliding surface comprises only friction and the cohesion is zero. It is based on a rock block on an inclined plane with a friction angle of ϕ_j between block and plane. The rock block is at rest if the force vector normal to the plane lies within the friction cone. If the force is acting from a direction outward of the friction cone the block starts to move. As illustrated in Figure 16 the failure envelope changes with different slope angle and friction cone. The risk of instability increases with a steeper slope as illustrated with the larger envelope. Moreover, a smaller friction angle enlarges the failure envelope (Wyllie & Mah, 2005).

4 Methods of geomechanical analyses

Rock slope stability is influenced by the topography, the rock mass conditions including orientation and frequency of discontinuities and water infiltration. To be able to detect the potentially more hazardous rock mass portions, determine their volume, and collect all the required geomechanical and geometrical parameters a three-dimensional rock mass characterization is necessary. The analysis of different rupture surfaces can help to indicate the subsurface fracture patterns in the 3D rock mass space and to differentiate between tectonic fractures and gravitational fractures (Gschwind *et al.*, 2019).
Postglacial rockfall studies were performed in the European alps using traditional mapping methods (Gischig *et al.*, 2011), terrestrial laser scanning and photogrammetry (Matasci *et al.*, 2017), (Gigli *et al.*, 2014), (Strunden *et al.*, 2015), borehole logging and geophysical surveys (Willenberg *et al.*, 2008), (Hugentobler *et al.*, 2020). Crackmeter measurements and total stations were used to determine fracture dynamics in a rock slope in Switzerland (Gschwind *et al.*, 2019) and on the north face of the Kitzsteinhorn, an unstable and deglaciated headwall in Austria (Ewald *et al.*, 2019), (Hartmeyer *et al.*, 2020).

4.1 Scanline and window mapping

The two most often used methods to determine discontinuity properties from exposed rock masses are scanline mapping and window mapping. Scanline mapping is a one-dimensional mapping technique, while window mapping occurs on a two-dimensional area. A rock mass characterization and description of discontinuities can be obtained according to the suggested methods by (ISRM, 1978). Following geomechanical properties of the rock mass discontinuities can be determined with field surveys: dip and dip direction, spacing, persistence, aperture, roughness (JRC) and weathering.

4.1.1 Scanline mapping

The scanline is placed on the exposed rock mass surface and discontinuities intersecting the scanline are recorded. The position and properties of the discontinuities are determined. There are several sources of bias and error during the field measurements of discontinuity persistence, which can result in under- or over-estimation of persistence (Shang *et al.*, 2018).

Sources, which may lead to a measurement bias, are (Shang *et al.*, 2018):

- Size: If discontinuities are too small or too short to measure, they are not included in the mapping. Additionally, longer discontinuities are more likely to intersect the scanline than smaller ones. Censoring occurs if discontinuities extend the sampling region or because the discontinuity end is covered by overburden or vegetation. Furthermore, length bias occurs because longer discontinuities are more likely to intersect the scanline than smaller ones.
- Orientation: Discontinuities striking roughly parallel to the scanline are not recorded.
- Censoring: Discontinuities may extend the sampling region, or the ends may be covered by overburden or vegetation, which may lead to a censoring of major joints.

To minimise the orientation bias, the scanline should be perpendicular orientated to the main discontinuity set. (Shang *et al.*, 2018) recommend establishing at least three scanlines along a rock exposure with right angles from each other. For example, one horizontally and two vertical scanlines. Moreover, the mapping should be undertaken at two mutually perpendicular rock faces to be able to record discontinuities which are parallel directed to the rock face.

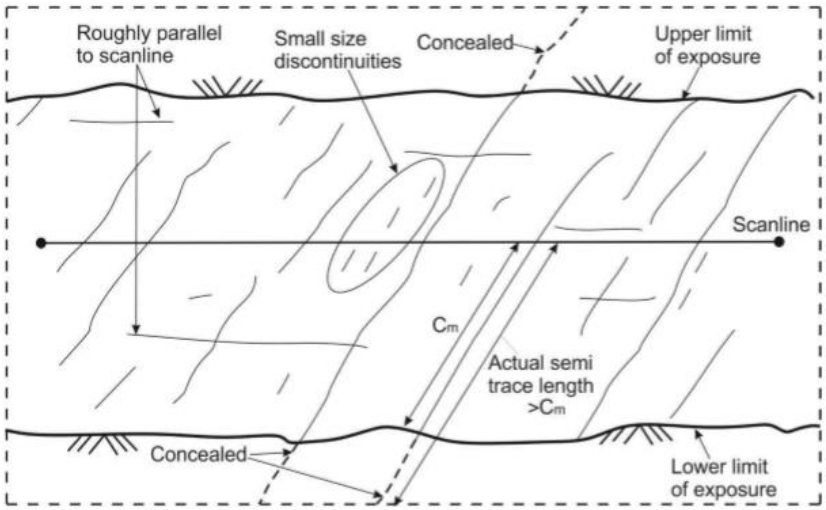

Figure 17 Major sources of bias and error in discontinuity length while field mapping. Truncation due to small discontinuities, censoring due to discontinuities extending the sampling region, Orientation bias if discontinuities strike parallel. Taken from (Shang et al. 2018).

4.1.2 Window mapping

A rectangle or circular area is defined on the outcrop. The sampling area should be sufficiently spacious to reduce the sampling bias, which means that each side intersects between 30 and 100 discontinuities (Shang *et al.*, 2018).

Discontinuities are categorised by three categories:

(1) Discontinuities included in the window, where both endings are visible within the

sampling domain.
(2) Discontinuities, which transect the window, meaning that both endings are invisible in the sampling domain because they end beyond the limits of the sampling window.
(3) Window intersecting discontinuities: One end is visible within the window and the other is ending beyond the limits of the window.
This method eliminates size and orientation bias because all orientations are represented equally within the window. However, this technique still suffers from the censoring issue. Thus, it does not provide any information about orientation or surface geometry for individual discontinuities (Shang *et al.*, 2018).

4.2 Remote sensing methods

Remote sensing methods can be used to investigate dangerous or inaccessible slopes (Tuckey & Stead, 2016). Several methods are suitable to establish three-dimensional models of rock exposures. These are important to quantify the activity of rockfall sources, estimate potential unstable volumes, and measuring the orientations of the main joint sets, serving to destabilize rock masses (Matasci *et al.*, 2017).

4.2.1 Digital photogrammetry and terrestrial laser scanning

Digital photogrammetry and terrestrial laser scanning allow a detailed three-dimensional assessment of fracturing pattern of rockwalls prone to rockfall. (Matasci *et al.*, 2017) quantified the fracture patterns at the Mt Blanc massive, by measuring the orientations of the main joint sets, and determined the type of failure mechanism according to the interaction between discontinuities and the local slope orientation. Discontinuity spacing and trace length data can also be quantified on terrestrial point clouds. The method is effective for identifying the most probable future rockfall sources, but temporal forecasting of rockfalls is still very difficult. Furthermore, sheeting joints within a rock mass are hard to detect with remote sensing methods because they run parallel to the cliff face and are therefore hidden.

4.2.2 Terrestrial infrared thermography (TIR)

Terrestrial infrared thermography (TIR) is a low cost, portable, non-destructive, and fast measurement method. The data can be used coupled with other remote sensing techniques (e.g. laser scanning), providing useful information about the rock mass (Fiorucci *et al.*,

2018).

Using TIR the temperature of the rock wall can be determined by capturing its emitted infrared radiation building images based on this data. Infrared thermal imaging is a method to detect intact rock bridges prior to failure. Compact rocks show a higher thermal inertia than fractured rocks. Therefore, fractured rocks should experience temperature variations faster. By repeating TIR surveys during cooling and heating phases, it is possible to highlight thermal anomalies. This approach was applied for the mapping of open fractures and features such as rock cavities, seepage, highly fractured zones, and weathered zones. Cold thermal signatures are expected for the surface of granitic exfoliation sheets because air circulation cools the back of the partially detached sheets. Warm temperature anomalies on the same sheets indicates rock attachment via rock bridges (Guerin *et al.*, 2019).

The measurements are affected by direct sun radiation because shaded areas typically have cold thermal anomalies. Therefore, TIR acquisitions should be obtained during night. Further, natural elements along a rock slope (vegetation, debris, talus, intact rock, weathered and fractured rock) affect the thermal signature. Thermal imaging combined with high-resolution 3d topography has significant potential for rockfall susceptibility and hazard analysis (Guerin *et al.*, 2019). Nevertheless, utilizing this method needs some investment in instrument as well as a calibration of the study area. The resulting thermal images must be superimposed with digital photographs to surely determine partially detached flakes reasoning in the fact that cold thermal anomalies can also exist for other reasons. In addition, image rectification and topographic corrections must be applied to thermograms to account for the influence of lens distortion, incidence angle, spatial orientation, and emissivity for each pixel (Guerin *et al.*, 2019).

Due to the investment, this method might be used for long-term hazard assessment on a smaller scale. Repeated surveys of the same area might show trends in rock bridge area reduction induced by fracture growth. Coupled with a stability analysis, it may be possible to forecast when rock bridge area decreases, thus the attachment length indicates fracture instability (Guerin *et al.*, 2019).

4.1 Literature review of deglaciated rock wall failures

4.1.1 Randa Rock slope failure (Switzerland)

The Randa rock slope instability in Switzerland results of two rockslides that occurred in April and May, 1991. A total amount of 30 million m³ crystalline rock failed within three weeks. The rock slope kinematics were analysed based on remote sensing and numerical modelling. A 3D model of the major rock structures was created by combining data from geological mapping, deep borehole logging, and geophysical imaging. Outcrop mapping of

the fracture network and additionally, scanline measurements along four lines of 40 – 140 m length on large rock faces in various lithologies was performed (Willenberg *et al.*, 2008). Seismic refraction was used to detect faults and fracture zones within the rock mass. The model includes the subsurface extent, orientation, and minimum persistence of major discontinuities for the uppermost 120 m of the cliff. The lower part of the 800 m high cliff is difficult to access. Therefore, structural analysis was performed by means of helicopter-based LiDAR and photogrammetry data. To create a kinematic model of the instability, the structural model was combined with displacement data measured at the surface with geodetic data, crack extensometers and benchmarks. In three deep boreholes inclinometer and extensometer measurements were conducted. The data was used to define discontinuity sets and the main kinematic failure mechanisms (Gischig *et al.*, 2011).

4.1.2 Tschierva rock avalanche (Switzerland)

(Fischer *et al.*, 2010) established a model of the effects of glacier retreat influencing rock slope instability. Based on geological mapping, different joint sets can be determined and kinematic analyses were performed to investigate the main failure mechanisms. A model of the ground temperature distribution was established based on climatic and topographic data. The analysis of the 1988 Tschierva rock avalanche suggested that many factors contributed to the rock slope failure. Rock mass properties, the geometry of two prominent joint sets with respect to the slope orientation and the fault zone with increased joining, were key factors. Progressive development of laterally persistent discontinuities after glacier retreat and debuttressing caused long-term rock mass weakening. Heavy precipitation may have been the final trigger (Fischer *et al.*, 2010).

4.1.3 Aar massive (Switzerland)

(Ziegler *et al.*, 2013) characterized exfoliation joints in the Aar Granite of the central Swiss Alp using the traditional field mapping and additionally computer-based mapping. A laser rangefinder, high resolution orthophotos and LiDAR-based digital terrain models were used to determine exfoliation occurrence and characteristics, such as joint orientation, visible length, spacing, surface weathering and roughness. For subsurface observation data from three boreholes was used (drill core and borehole image interpretation). Three vertical 50 m deep boreholes were drilled to continuously monitor groundwater pressure, temperature and deformation to investigate thermo-hydro-mechanical mechanisms coupled to slope processes that drive rock mass damage. As a result, they state that exfoliation joints are best developed in massive granitic or gneissic rocks. They distinguished different exfoliation

joint generations based on their geometric properties and characteristics.

4.1.4 Kitzsteinhorn (Austria)

To be able to determine processes destabilising recently deglaciated rockwalls the dynamics of a fracture at the north face of the Kitzsteinhorn (3202 m a.s.l.) was monitored over a period of 2.5 years. Horizontal and vertical deformation is measured with two crackmeters. The resulting data implies that fracture dynamics are dominated by freeze-thaw action during spring and summer rather than hydrostatic pressure. Vertical deformation is triggered by rainfall events providing liquid water into the fracture system. Lower magnitude horizontal deformation occurs in autumn and early winter due to ice segregation. (Ewald *et al.*, 2019) highlighted the importance of liquid water intake in combination with temperatures below 0°C on the destabilisation of glacier headwalls. Further, frost action and ice segregation are important preparatory factors of paraglacial slope instability. After deglaciation, the rock wall is exposed to direct atmospheric forcing. The formerly constant thermal regime is disturbed by diurnal to annual temperature cycles, termed as ‘paraglacial thermal shock’. A long-term LiDAR study from the Kitzsteinhorn found dramatically increased rockfall activity, which may be due to paraglacial response (Hartmeyer *et al.*, 2020).

4.1.5 Adamello Group (Italy)

The Adamello-Presanelly Group is the southernmost massif of the central Italian Alps.
The engineering geological surveys focused on measuring the rock mass jointing in suitable exposures using data from geomechanical scanline measurements in accessible outcrops. On inaccessible cliff walls, joints were remotely identified using high-resolution digital camera analysis. The jointing conditions were determined by directly measuring following variables: joint attitude (dip direction and dip angle), number of discontinuities per m^3, the average dimension of an equivalent cubic block representative of the joint-bounded rock mass, joint aperture, uniaxial compressive strength (which was obtained using the Schmidt hammer). Stereonet plots of the joint sets were obtained. Afterwards a thermomechanical numerical model was established based on geomechanical field measurements. The combination of field observations and numerical simulations gives more information about the effects of thermomechanical loading and gravitiy-induced processes that affect the slopes (Baroni *et al.*, 2014).

5 Field site Ödenwinkelkees

5.1 Location

The Ödenwinkelkees is a glacier in the high mountains of the Austrian Central Alps in the Austrian province Salzburg. The Ödenwinkel valley is a southern valley of the Stubach valley in the High Tauern range. The Stubach valley on the border to the Granatspitzgroup and the glaciated Glocknergroup (Figure 18).
The field site is located in the Hohe Tauern National Park. The study location is well known for the nearby Rudolfshütte Alpinzentrum at 2315 m above sea level, which can be reached with the cable car from Enzinger Boden. In addition, a large construction site to build the Tauernmoos pumped-storage power station from ÖBB-Infrastruktur is planned there (ÖBB-Infrastruktur AG, 2021).

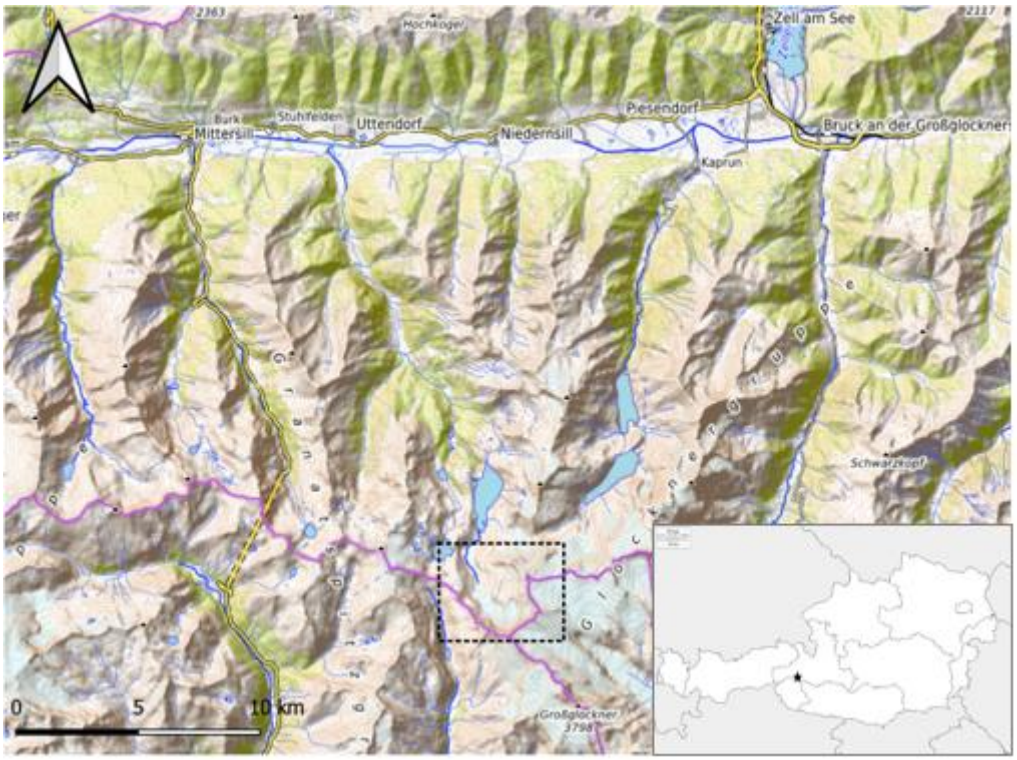

Figure 18 Location of the study area, which is accessible from Uttendorf. Basemap taken from (OpenTopoMap, 2020).

The Ödenwinkelkees is a valley glacier drifting from south-east of the Stubach valley between Johannisberg and Eiskögele into north-western direction into the valley. In the south the glacier is restricted by a up to 600 - 800 m high, steep and north facing cirque-shaped headwall formed by the peaks of Hoher Kasten (3189 m a.s.l.), Eiskögele (3423 m

a.s.l.), and Johannisberg (3453 m a.s.l.) (Figure 19). This high and steep north-facing headwall clearly favoured the conditions for the glacier to form. The glacier has an area of 1.9 km² and is mainly covered by the avalanches from the headwall. It is the largest glacier of the Stubachtal and the catchment area reaches from 1790 to 3490 m asl. (Carrivick *et al.*, 2013).

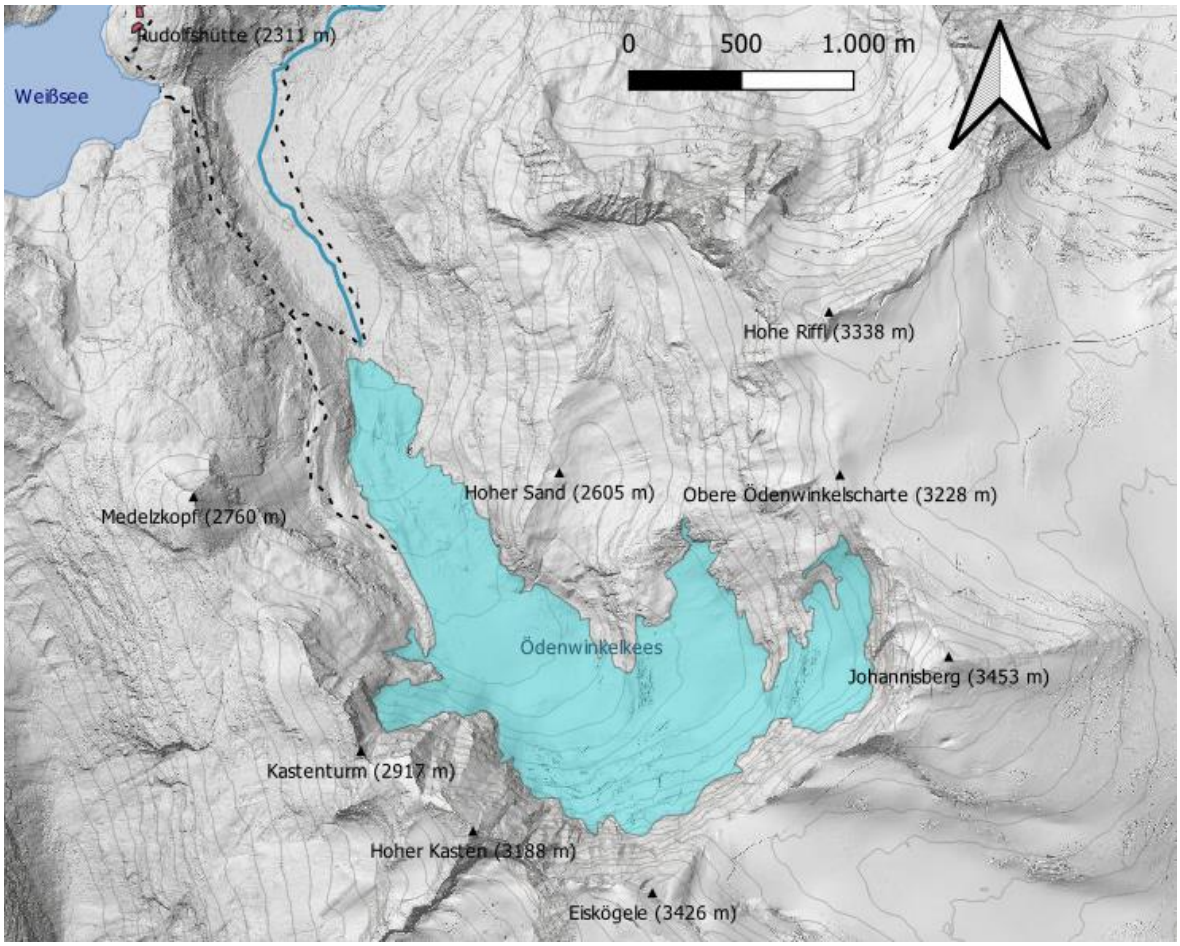

Figure 19 Area around the Ödenwinkelkees. Corresponds to dashed square in Figure 18. Basemap taken from (Basemap, 2020) and modified with QGIS (QGIS, 2020).

This thesis deals with the stability analysis of the rockwalls on the western side (right sight on Figure 20) of the valley along the hiking trail (dashed black line). The study area is considered to be ice free since 1850 (Carrivick *et al.*, 2015).

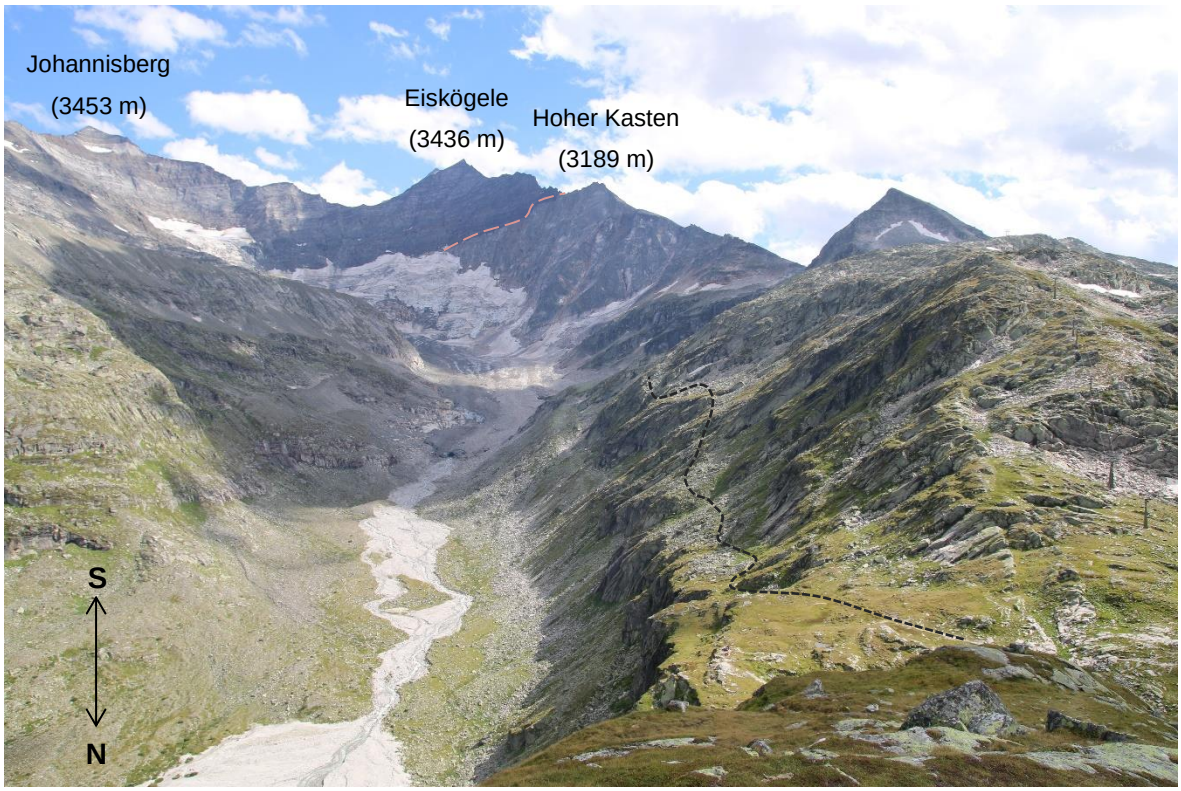

Figure 20 View of the Ödenwinkelkees and its glacier forfield in southern direction in August 2020. The hiking trail is sketched (dashed black line). The lithological border at the headwall in the south is marked in red.

5.2 Geology

5.2.1 The Tauern Window

The Ödenwinkel valley is located within the Tauern Window. A geological structure in the Austrian Central Eastern Alps. The Tauern Window is 160 km long, 30 km wide and strikes subparallel to the Eastern Alpine orogeny. It exposes high-grade metamorphic rocks from a deep structural level of the Alpine orogeny. Underlying penninic and sub-penninic nappes are uncovered by a combination of tectonic and erosional unroofing (Schmid *et al.*, 2013).

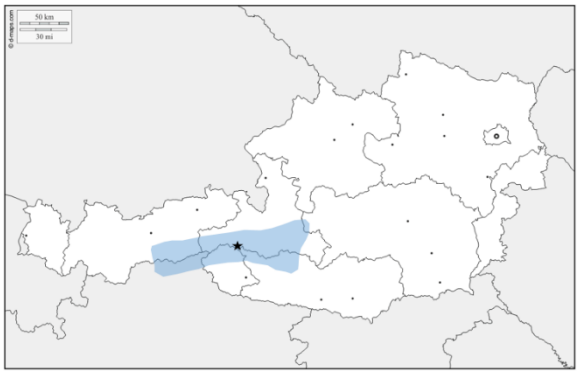

Figure 21 Map of Austria (d-maps, 2021) with the Tauern Window and location of study area.

The Tauern Window is primarily characterized by a crustal-scale duplex, the Venediger Duplex, formed during the Oligocene. It is overprinted by doming and lateral extrusion during the Miocene. Approximately half of the Tauern Window is made up of Permo-

Mesozoic formations, the other half consist of pre-Permian rocks.

The Venediger Duplex mainly consists of orthogneisses (“Zentralgneis”) composed of Variscan granitoids, micaschists, and metavolcanic sediments of the post-Variscan cover. The Modereck nappe is situated above this duplex structure and is composed of micaschists, marbles, and quarzites as well as gneisses and amphibolites silvers. Above these units the Glockner nappe system, derived from the Valais Ocean can be found. It is composed of calcshists and metapelites intercalated with prasinites, amphibolites, and phyllites. Surrounding the Tauern Window and structurally overlying all other units described above are the Austroalpine units. They are derived from the Adriatic Plate and largely consisting of a metamorphic basement of the Variscan age that cooled below 300°C in the Cretaceous (Schmid *et al.*, 2013).

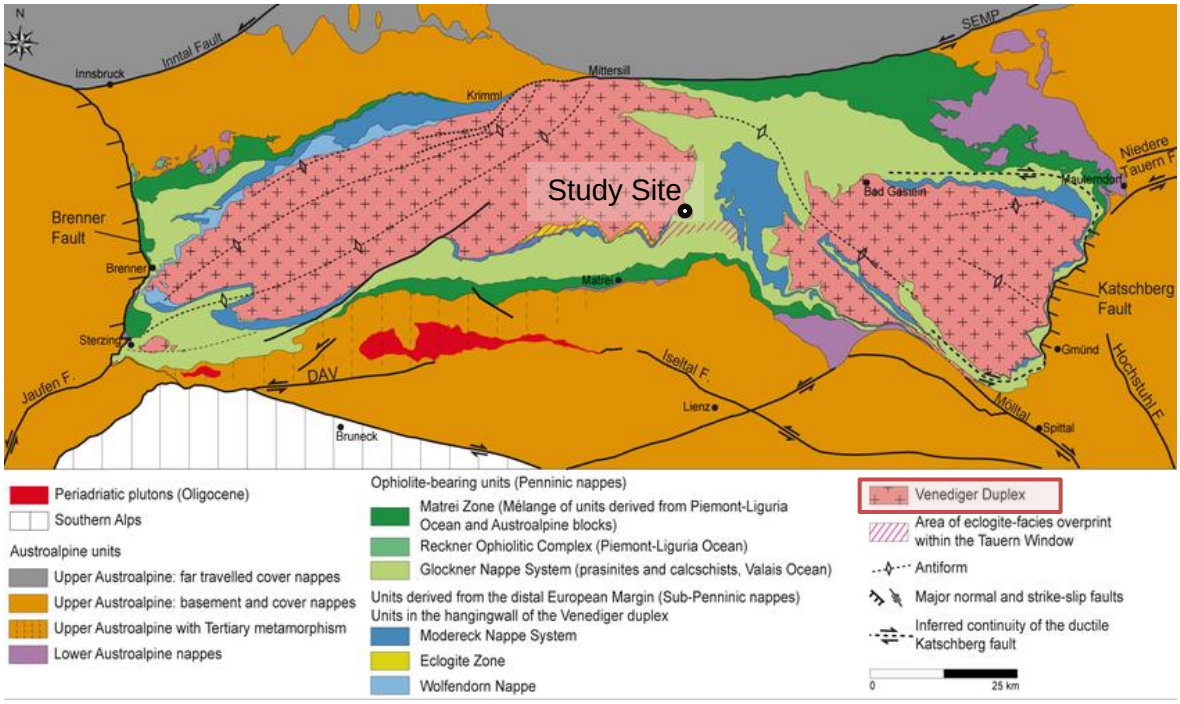

Figure 22 Tectonic map of the Tauern Window based on (Schmid et al., 2013) and modified by (Bertrand, 2013).

The rock slopes in the study area are composed of “Zentralgneis” which corresponds to granitic gneiss (Carrivick *et al.*, 2013). The “Zentralgneis” is an alpine metamorphic, late postvariscian (335 Ma to 292 Ma) granitoid intrusion (Veselá *et al.*, 2011). The rock is light grey, and consists of feldspar, quartz and glimmer. The foliation can be determined due to regulated mica layers, which are roughly horizontal.

South of the Ödenwinkel glacier, the lithological border of the upper lying Riffldecke (penninic mica schists and amphibolites) and the underlain granitic gneisses is visible (sub-penninic). The border between the peaks of Hoher Kasten and Eiskögele is well recognizable reasoning in the darker colour of schists and amphibolites of the Riffldecke compared to the typically brighter granitic gneisses as marked in Figure 20. The hillslopes

and the valley floor are partly covered by debris as mapped in Figure 23 (yellow area) (Höck & Pestal, 1994). They result from glacial, fluvial or gravitational processes.

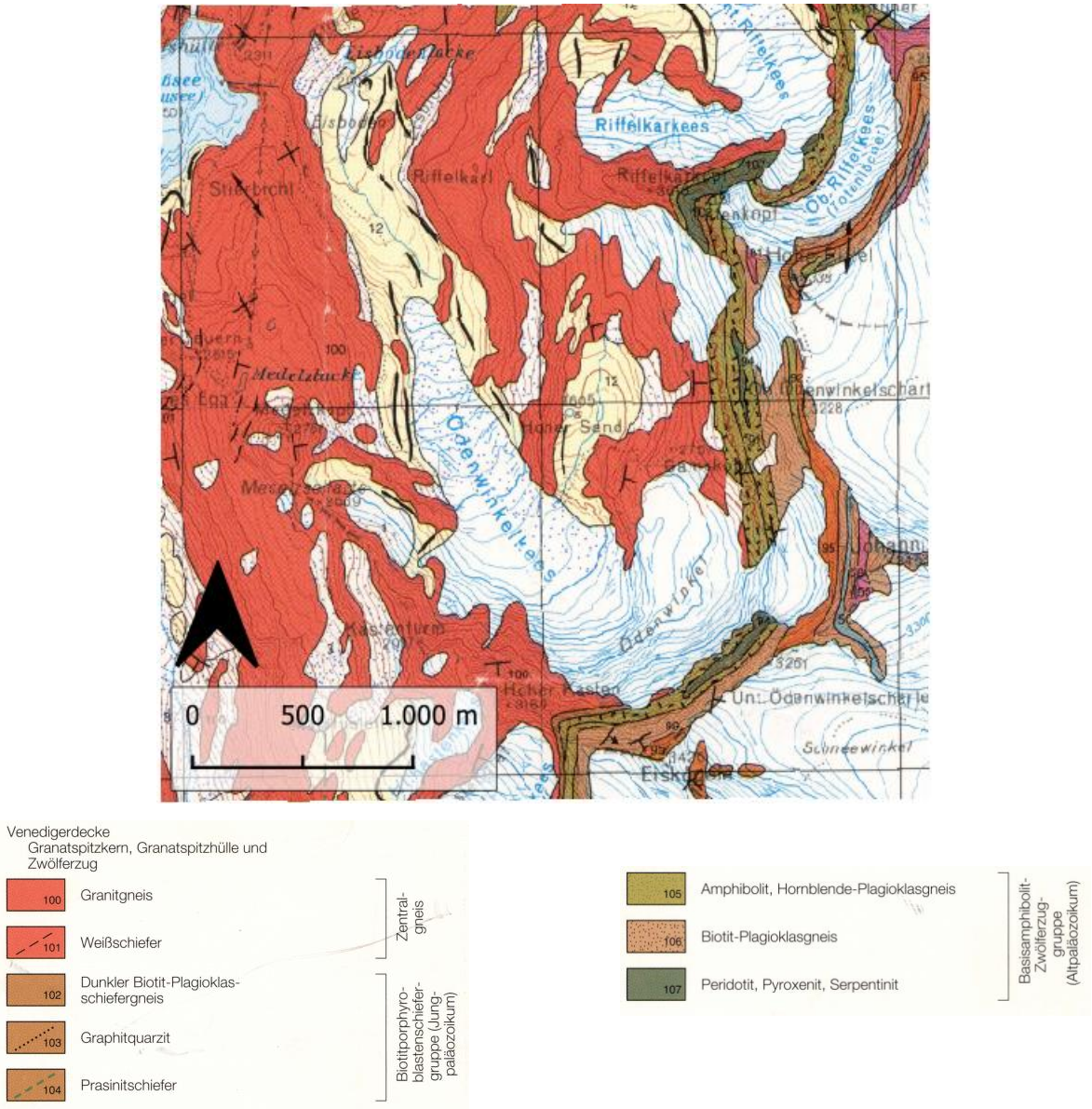

Figure 23 Geological map of the study area (GK50 153-Großglockner (Höck & Pestal, 1994)).

5.3 Climate

A weather station is located on the Rudolfshütte (2317 m). Access to climate data is provided by the ZAMG (“Zentralanstalt für Meteorologie und Geodynamik”) (ZAMG, 2021). Data of the air temperature is available since 1990 and displayed in Figure 24. As Figure 24 shows, a rise of temperature is recognizable. During the time period from 1990 to 2019 the mean annual air temperature increased by 1.2 °C. The mean annual temperature in 1990 was -0.5 °C and rose until 2019 reaching an average temperature of almost 0.7 °C.

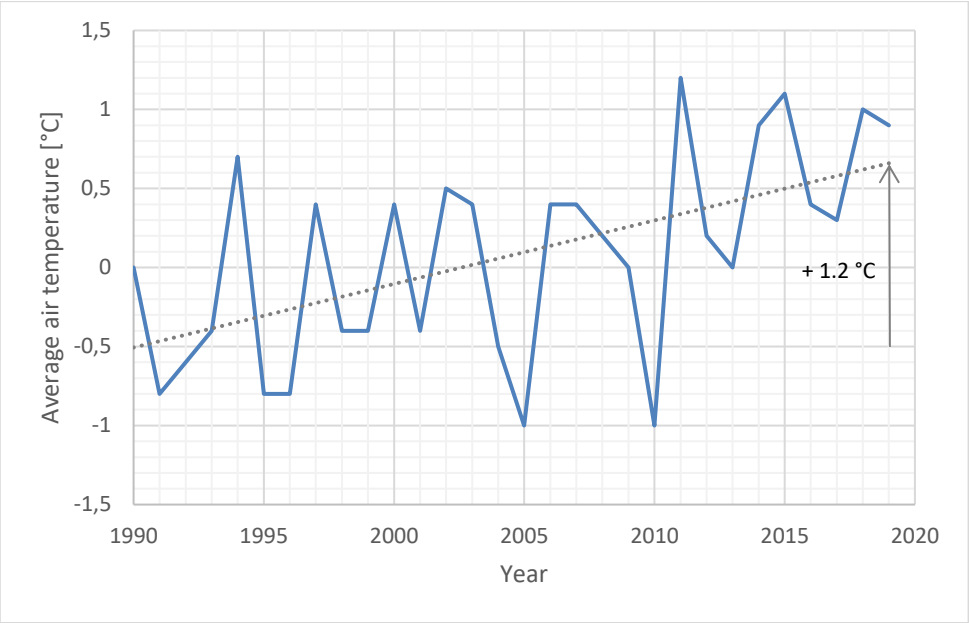

Figure 24 Average air temperature at Rudolfshütte from 1990 to 2019.

The total annual precipitation during the same time period (1990 to 2019) at Rudolfshütte is between 2000 mm/year and 3000 mm/year (Figure 25). Only in 2003 was less precipitation (1548 mm/year), because of an extremely dry summer. At Rudolfshütte a high amount of precipitation can generally be recognized. However, in the time period of 1990 to 2019 a decrease of total precipitation is observed.

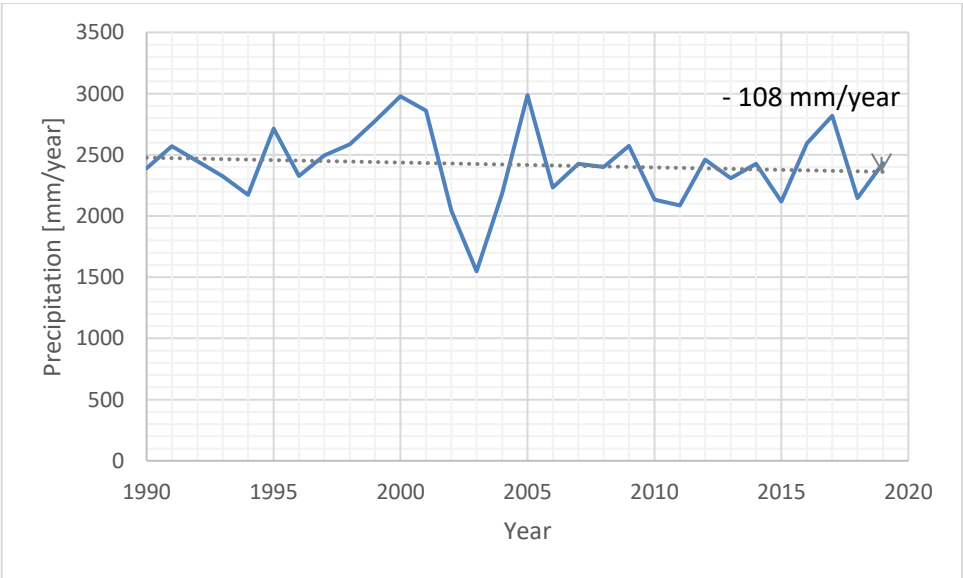

Figure 25 Total precipitation per year at Rudolfshütte from 1990 to 2019.

In Figure 26 the number of days of each year with closed snow cover are displayed. A decrease of in average 35 days per year during the last 30 years is recognizable.

Snow cover can act as a shield and protect the rock mass against direct atmospheric forces like solar radiation. Thus, less days with a snow cover, results in an increasing exposition of the rock mass to weathering processes and the rock mass alters faster.

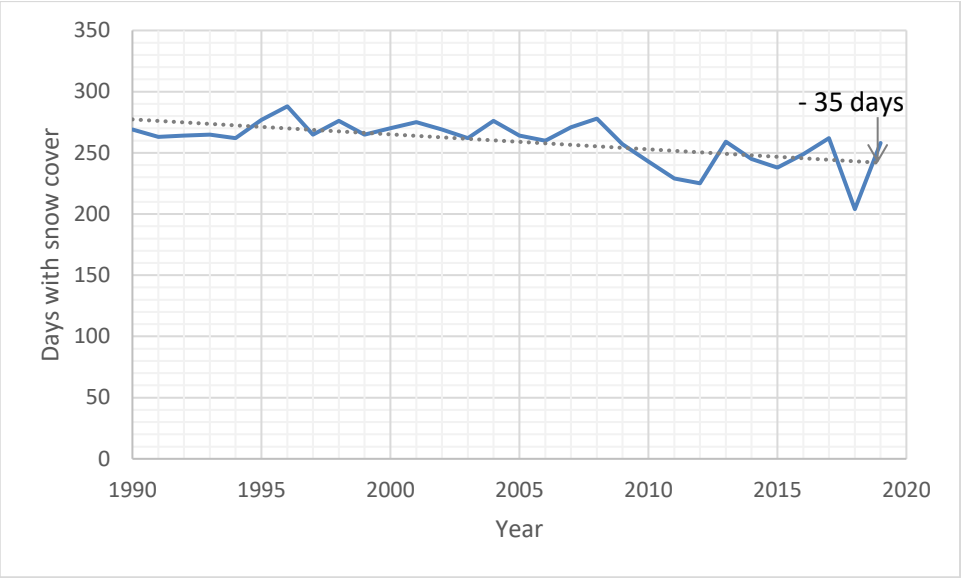

Figure 26 Days with snow cover at Rudolfshütte from 1990 to 2019.

Further, the days with a temperature below 0 °C decrease (Figure 27). Instead of steady freezing conditions there might be more fluctuations with temperatures slightly above 0 °C. This may lead to enhanced weathering because of freeze-thaw processes. The ice within pores close to the surface will melt more often and therefore, the rock mass is subjected to higher thermo-mechanical stresses. This trend additionally leads to permafrost thaw.

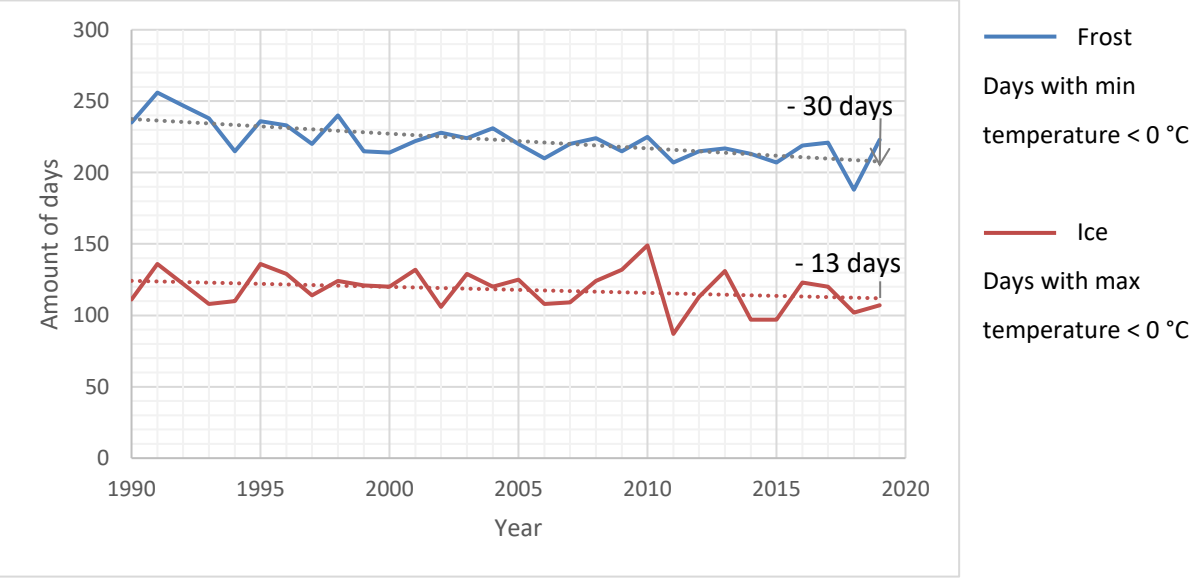

Figure 27 Days with minimum air temperature (frost) or maximum air temperature (ice) of < 0°C at Rudolfshütte (from 1990 to 2019).

5.4 Glacial history

The Little Ice Age describes a climatic interval with the most extensive recent period of mountain glacier expansion (Munn, 2002). After the maximum ice extent in 1850 warmer summers and less ice accumulation caused glaciers to shrink. The impact of global warming is obvious at the Ödenwinkelkees. The glacier lost 40% of its area and 75% of its volume

since 1850 (Carrivick *et al.*, 2015).

During 1920 – 1945 temperatures increased, and a significant mass loss of ice occurred. The degradation continued due to melting, unevenly descending glacier surface and simultaneously undermining of the glacier. During 1965 – 1981 a colder period prevented a continuous melting of the glacier. In the mid-60s the mass balance was positive, which means an expansion of the glacier. With a time lap of 20 years the deglaciation stopped around 1985 and the glacial border almost did not move until 1995/96. In-between 1991 and 1997 the length only decreased by 5 m. Since 1982 a time period of warm summers started. In 2014 the large retreating rates started again after a time period of 30 years. At the weather station of the Rudolfshütte the mean annual temperature increased by 1.7°C from 1960 to 2018. Therefore, the ablation of the Ödenwinkelkees increased despite the debris cover and a larger amount of ice melted than was generated. Measurements of length and velocity are conducted at the Ödenwinkelkees since several decades. The glacial length decreased 500 m (until 2019) since the observation started in 1960. Before, the change of glacial length is assessed based on photographs. Between 1850 and 2019 the length decreased by 1585 m (these and more values are summarized in Table 1). The ice thickness was estimated in 1998 using radar techniques, which resulted in a mean value of 50 ± 3 m. The loss of mass between 1946 and 2019 is equal to 67.4 Mio m³. The glacier equilibrium line altitude increased by 90 m between 1850 and 2008. If the present linear trend in declining ice volume continues, then the Ödenwinkelkees will disappear by the year 2040 (Slupetzky, 2020).

The glacier retreat can be seen in the two comparing photographs of the Ödenwinkelkees from 1929 and 2015 (Figure 28).

Table 1 Change of glacier length of the Ödenwinkelkees (1850 - 2019) adapted from (H. Slupetzky, 2020).

Year	Time Interval [Years]	Change of glacier length [m]
1850 – 1900	10	- 460
1900 – 1925	25	- 150
1960 – 2017	57	- 490 (measured)
1850 – 2019	129	- 1585

Figure 28 The Ödenwinkelkees 1929 (Photo: E. Baumann) and 2015 (Photo: H. Slupetzky). The strong glacier retreat is obvious.

In the present, the glacier tongue is stagnated, and the collapse of hollow spaces is starting because of subglacial melting and a resulting thinning of the glacier. Since 2010 a glacier mouth forms, where typically the ice accumulates, but almost no movement happens anymore. Therefore, dead ice may form soon and the glacier retreats further (Slupetzky, 2020).

During the loss of ice lateral and frontal moraines were formed. The Holocene glacial history can well be retraced by the moraines, which are still discernible as marked in Figure 29.

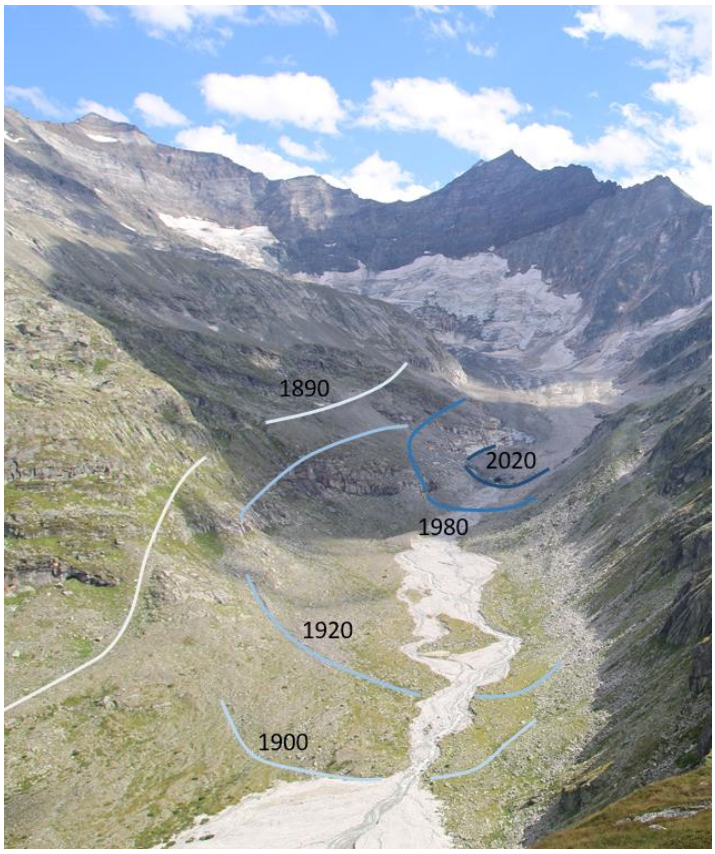

Figure 29 The location of the moraines recognizable in the field. Since 1850 the glacier length decreased by appox. 1500 m.

6 Methodology

6.1 Data acquisition

Discontinuities in the rock mass are mapped in-situ following traditional geomechanical field surveys. Therefore, scanline surveys and discontinuity orientation measurements are performed. Measurements are mainly conducted along the hiking trail leading from the Rudolfshütte in the direction of the Ödenwinkelkees on the western side of the glacier forefield. The measurement points along a total distance of 1200 m are marked in the map in Figure 30. It must be noted that only joints that are clearly visible at the slope surface are included. At all locations joint orientations (dip and dip direction) are determined using the geological compass. Additionally, scanline measurements are carried out at the measurement points 4, 5 and 8. Six scanlines of 1.5 m to 10.5 m length are installed with different orientations. Two are roughly striking N-S, three W-E and one is vertically. The scanline mapping followed procedures recommended by (ISRM, 1978). After installing the scanline at the outcrop, trend and plunge of the tape is measured. Afterwards following joint characteristics can be determined:

1) Spacing can be measured by determining the distance between the starting point of the scanline and the intersection point of the joint plane and scanline.
2) Semi-trace length is measured from the intersection point on the scanline to the end of the joint on one side of the scanline.
3) Persistency describes how continuous the fractures are, or if any rock bridges are present and can be defined as persistent, intermittent, or non-persistent
4) Termination: A joint can terminate into another joint (J), it can be obscured (O), when the ends of the joint exceed the outcrop, or terminate in the intact rock (R).
5) Roughness are small scale undulations. The Shape of the fracture surface is compared to the standard roughness profiles to get the Joint Roughness Coefficient (JCR).
6) Waviness are large scale undulations. Can be describes as stepped, undulating, curved or planar.
7) Aperture: the perpendicular distance separating the rock walls of a discontinuity
8) Weathering of the joint surface can be assessed visually, for example according to the color.

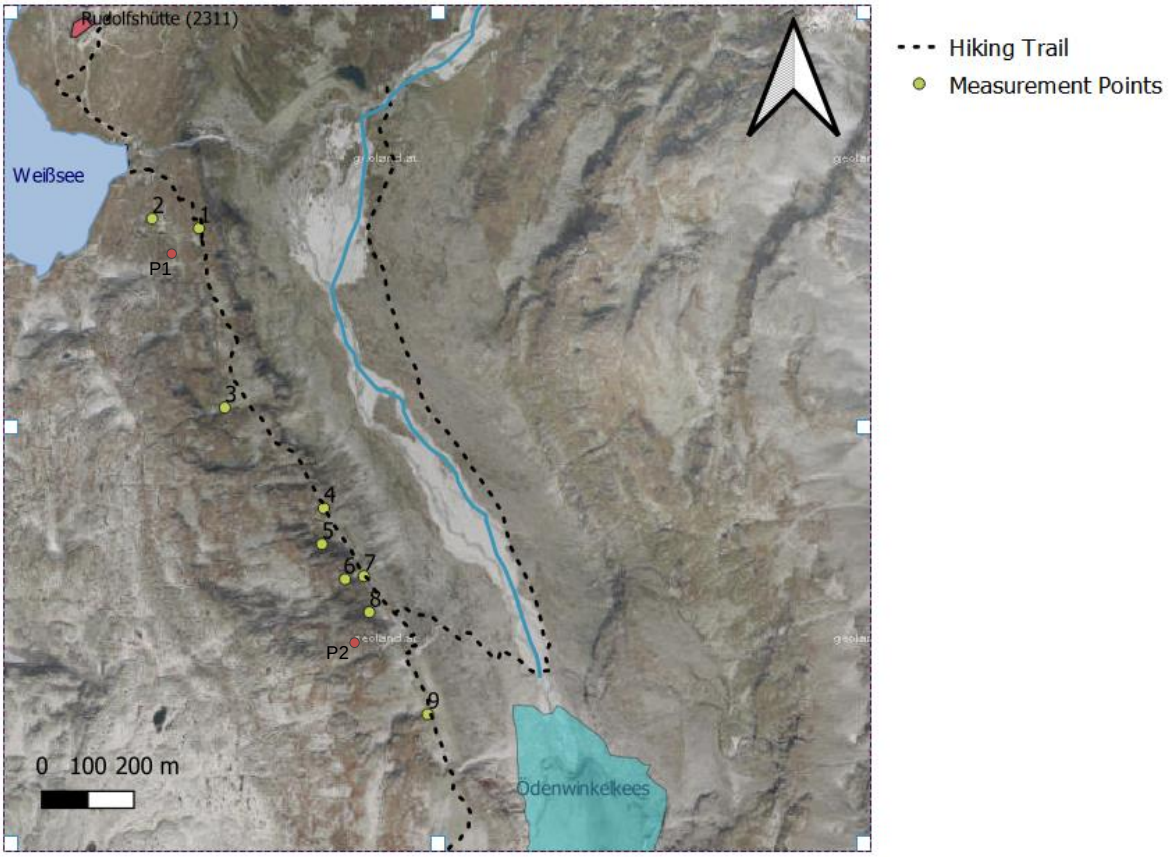

Figure 30 Location of measurement points (1-9) and of the photographic analysis (P1 & P2) within the study area north of the Ödenwinkelkees. The basemap is taken from (SAGIS, 2020).

6.2 Analysis

6.2.1 Kinematic Analysis

With the data obtained during the field work and photographs of the study area a statistical analysis was carried out to be able to characterize different joint sets. Joints can be grouped in different sets after geometrical classification and differences in spacing, curvature, visible trace length and weathering. The aim is to distinguish tectonic joints and exfoliation joints, which developed due to the deglaciation. Therefore, the spatial distribution of the joints at the slope surface and characteristics of joints are observed.

For the analysis of potential failure mechanisms of the rock slope a detailed knowledge of the kinematic behaviour of the rock mass is required. Kinematic analyses are conducted in order to indicate failure potential and feasible failure modes. Assumptions for this analysis are fully persistent, cohesionless and dry discontinuities, a rigid block behaviour and a planar slope morphology. Therefore, this method simply indicates the kinematically feasible modes for a certain slope and joint set angles. Key parameters are the slope orientation, the dip angle of discontinuities and their friction angle. The orientation data obtained during the field work was analysed using Dips 7.0 (Rocscience, 2020). A stereonet-based

kinematic analysis of planar sliding, wedge sliding, flexural toppling and direct toppling, was performed comparing orientation data of the joints to the surface slope orientation. The proportions of joints critical oriented for sliding or toppling are evaluated. The analyses assumed a friction angle of 30°. For direct toppling and sliding to occur, a horizontal deviation from the mean slope dip direction of ± 20° (lateral limits) was considered. Stereographic kinematic analysis techniques as described by (Goodman, 1976) and (Wyllie & Mah, 2005) are used. Further explanation of the basics of this technique is provided in section 3.6. For kinematic analyses of planar sliding and flexural toppling the pole points of all measured discontinuities are used. For wedge sliding, direct, and oblique toppling, the intersections between the discontinuities are needed. A sensitivity analysis was conducted to observe the impact of a changing dip angle of the slope surface. By inputting a range of values for the dip angle of the rock slope, its effect on critically oriented discontinuity planes can be determined.

The software QGIS (QGIS, 2020) was used to analyse the digital elevation model (DEM) of the study area. The mean slope orientation of the rock wall is determined with several cross profiles.

6.2.2 Photographic Analysis

In order to determine the spatial pattern of discontinuities photographic analyses are carried out. It provides more information about the statistical distribution of the joint sets in the study area. Additional information about characteristics like persistency, termination and spacing can be checked by visual assessment. At location points P1 and P2 (marked in Figure 30) photographic analyses of the rock slopes are carried out. Therefore, photos of the rock wall were made during field work. After the stereographic projection of the joints with Dips 7.0 (Rocscience, 2020) was made, the joints can be divided in different groups. According to this result the joints on the photograph are coloured using the open source image editor GIMP (GIMP, 2020). The edited photo is helpful to recognize which joints belong to which set. The spatial pattern of the discontinuity network can be marked within the photograph. Properties like spacing and persistence can be determined in a larger scale than with a scanline. Also, the surface texture of joint planes can be described. The photographic analysis was also used for comparison of the discontinuities on the opposite valley side. Due to difficult accessibility no measurements were conducted. With the photographs the pattern of discontinuities can be evaluated on both valley sides. Photographs were also used to assess the time pattern of the formation of joints and how much time after deglaciation is needed for joints to propagate. This is based on the discontinuities that can be seen on the rock mass surface.

7 Results

In the following chapter resulting data of the compass and scanline measurements are presented. The detailed orientation and scanline data can be found in Appendix A. The locations of the outcrops are marked in Figure 30. The measurement points in the figure correspond to the outcrop number.

7.1 Outcrop 1

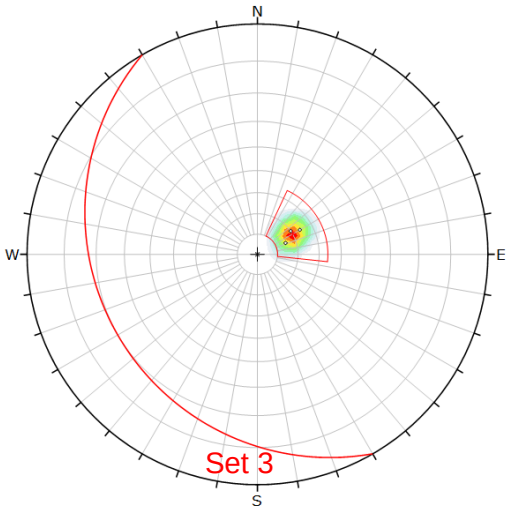

At the first measurement point, three orientation measurements with the compass were conducted. The values are similar and correspond to the same Joint Set as illustrated in Figure 31. The mean orientation of this set is 240/20.

Figure 31 Stereographic projection of plane orientation measurements conducted at outcrop 1.

7.2 Outcrop 2

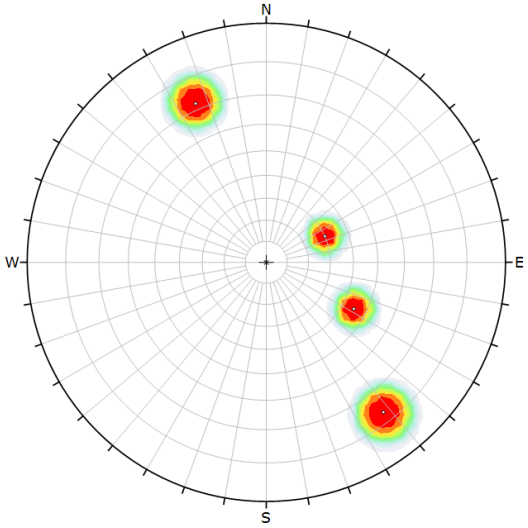

At the second outcrop four measurements were carried out. These are variable and cannot be related to the same joint sets as illustrated in Figure 32.

Figure 32 Stereographic projection of plane orientation data.

7.3 Outcrop 3

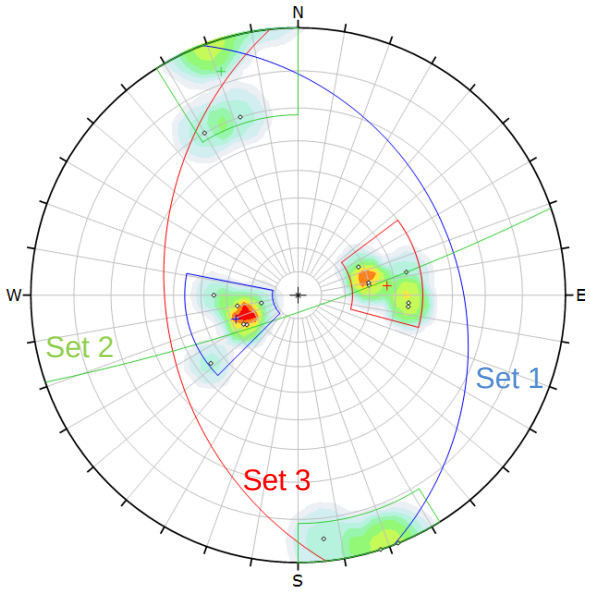

As is can be seen in Figure 33, 17 measurements were carried out at outcrop 3. They can be divided into three different joint sets. The mean set plane orientation for each set is 069/28 (Set 1), 161/83 (Set 2) and 264/37 (Set 3).

Figure 33 Stereographic projection of orientation data at outcrop 3.

7.4 Outcrop 4

7.4.1 Scanline 4

At outcrop 4 scanline mapping was conducted. One scanline was installed roughly striking north-south. Data like length and orientation of the scanline and size of the outcrop is summarized in Table 2. In Figure 34 photographs of the scanline can be seen.

Table 2 Set up data of outcrop and scanline 4.

Scanline 4			Outcrop			
Trend	Plunge	Length (m)	Dip Direction	Dip	Height (m)	Width (m)
340	90	10.5	080	30	20	10.5

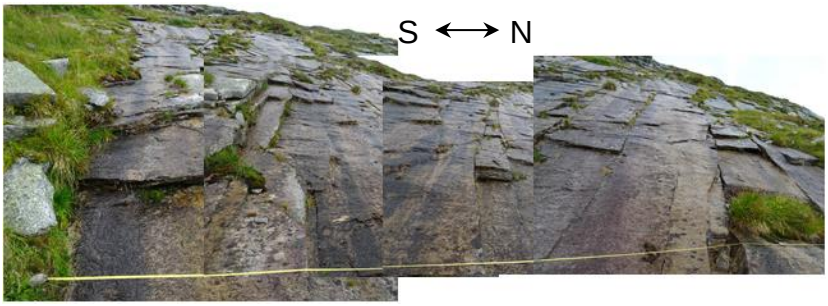

Figure 34 Set up of Scanline 4

During scanline mapping 4 joint properties of the roughly east-west striking, steeply dipping joint set is determined. 13 joint planes cross the scanline with a length of 10.5 m and the spacing varies between 0.1 and 1.55 m. The joints are persistent or intermittent as the joint plane surface is often stepped. The aperture varies between 1 and 10 mm.

7.4.2 Stereonet projection

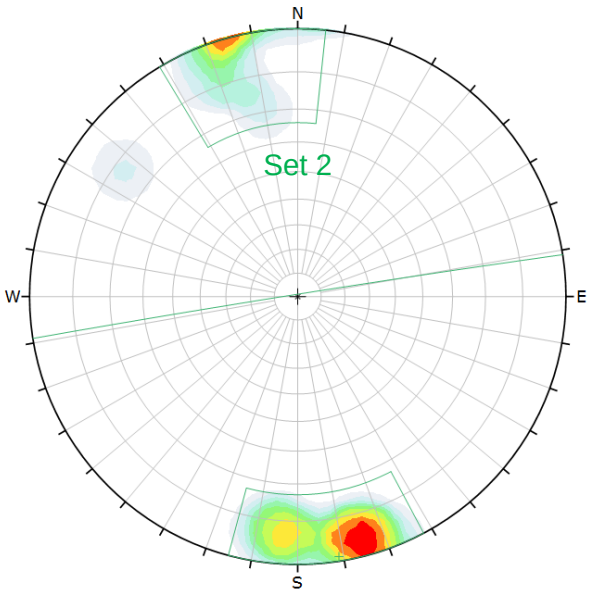

As a result of the scanline mapping 13 measurements of joint planes are determined. The orientation data is displayed in Figure 35. The points can be summarized to one joint set with a mean set plane orientation of 351/89.

Figure 35 Stereographic projection of measurements of scanline 4.

Additionally, six measurements with the compass were carried out at the same location. The measurements can be divided into two different joint sets (Figure 36). The mean orientation of each set plane is 074/39 for Set 1 and 348/87 for Set 2.

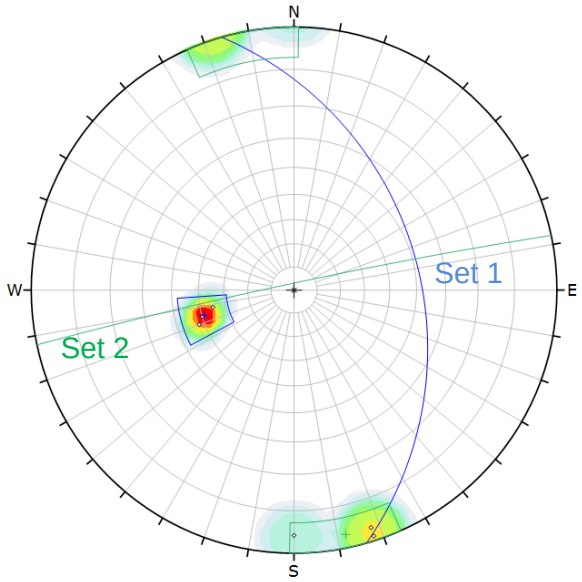

Figure 36 Stereographic projection of planes measured with the compass at outcrop 4.

7.5 Outcrop 5

7.5.1 Scanline 1-3

The scanlines were set up at the location point 5 (in Figure 30). Scanline 2 and 3 are parallel to each other striking east-west and Scanline 1 is oriented normal to 2 and 3 striking north-south. The set-up data of each scanline is summarized in Table 3, Table 4 and Table 5.

Table 3 Set up data of outcrop and scanline 1.

Scanline 1			Outcrop			
Trend	Plunge	Length (m)	Dip Direction	Dip	Height (m)	Width (m)
342	8	5,6	072	70	10	6

Figure 37 Outcrop at scanline 1.

The outcrop of scanline 1 is displayed in Figure 37. Properties of the vertical joint planes are determined using this scanline (in Figure 40 defined as Set 2). Five joint planes cross the scanline. The spacing varies between 0.3 and 2.1 m. The mean set plane orientation is 345/86. The joints are persistent, wavy, and rough as they often are stepped. Aperture was recognizable to be between 2 and 10 mm.

Table 4 Set up data of outcrop and scanline 2.

Scanline 2			Outcrop			
Trend	Plunge	Length (m)	Dip Direction	Dip	Height (m)	Width (m)
164	10	5	162	85	10	5

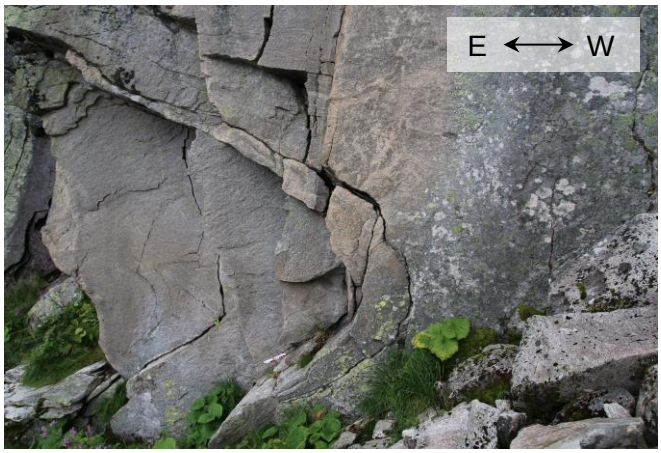

Figure 38 Outcrop at scanline 2.

Table 5 Set up data of outcrop and scanline 3.

Scanline 3			Outcrop			
Trend	Plunge	Length (m)	Dip Direction	Dip	Height (m)	Width (m)
342	15	5,3	350	75	20	6

Figure 39 Set up of scanline 3.

During scanline mapping 2 and 3, properties of joint planes steeply dipping in eastern direction are determined (later defined as Set 4). At scanline 2 six measurements were made. The spacing varies between 0.13 and 1.14 m. The mean orientation is 261/87. The joints are less persistent terminating into other joints. Most of the joints are very rough and wavy. At scanline 3 eight joint planes cross the scanline with a spacing between 0.05 and 1. 55 m and a mean orientation of 266/63. The joint planes are less wavy and rough but aperture with up to 10 mm and bend joints are recognizable.

7.5.2 Stereographic projection

In total 14 measurements were conducted during scanline mapping 1 – 3 and are illustrated in Figure 40. Two different joint sets can be differentiated and the mean orientation of each is 345/86 for Set 2 and 264/82 for Set 4.

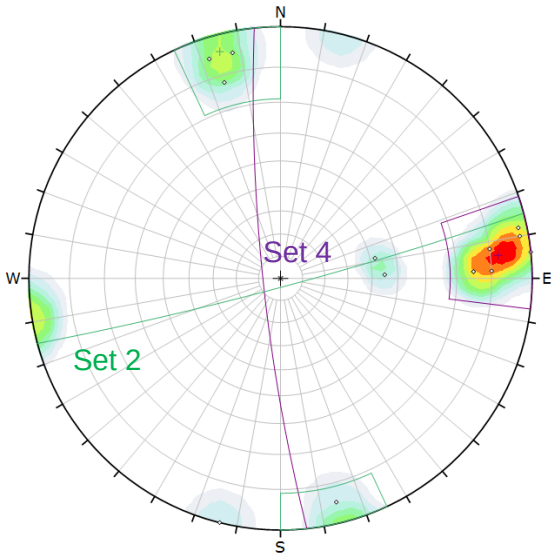

Figure 40 Stereographic projection of scanline measurements 1 - 3.

7.6 Outcrop 6

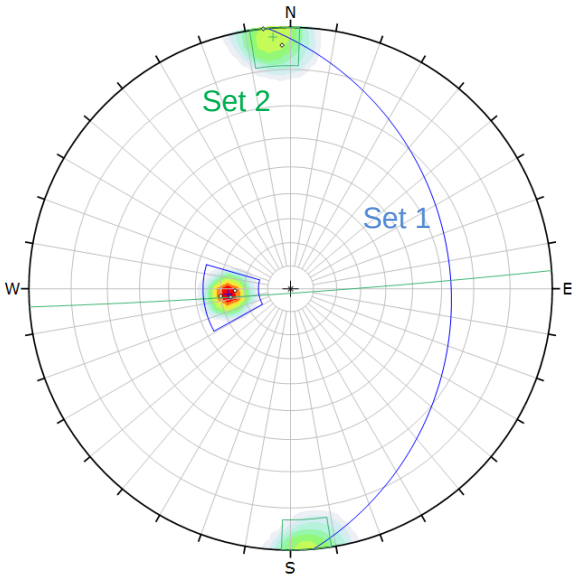

At outcrop 6, five measurements were conducted. These can be differentiated into two joint sets as illustrated in Figure 41. The mean orientation of each set is 085/27 for Set 1 and 358/88 for Set 2.

Figure 41 Stereonet projection of orientation measurements at outcrop 6.

7.7 Outcrop 7

At outcrop 7, five measurements were carried out. These can split up into two different joint sets (Figure 42). The mean orientation of Set 1 is 071/37 and of Set 2 002/89.

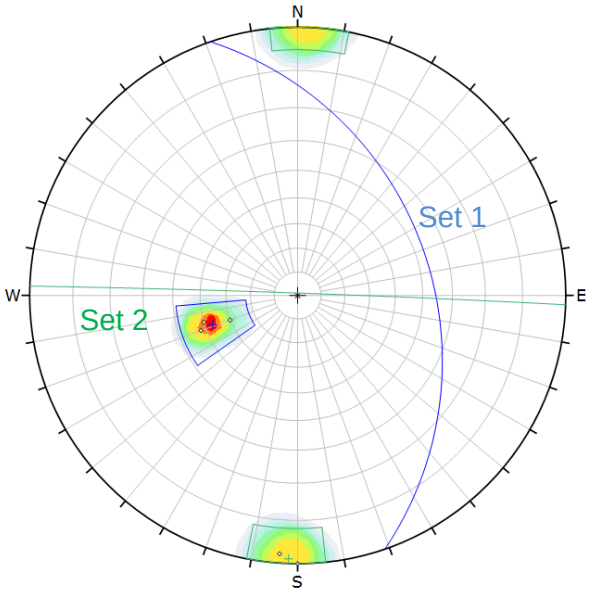

Figure 42 Stereonet projection of orientation data measured at outcrop 7.

7.8 Outcrop 8

At outcrop 8, two scanline measurements were carried out. One horizontal striking east-west and one vertical scanline. The set-up data are summarized in Table 6 and Table 7.

7.8.1 Scanline 5 and 6

Table 6 Set up data of scanline 5.

Scanline 5			Outcrop			
Trend	Plunge	Length (m)	Dip Direction	Dip	Height (m)	Width (m)
280	35	7.6	174	82	2	40

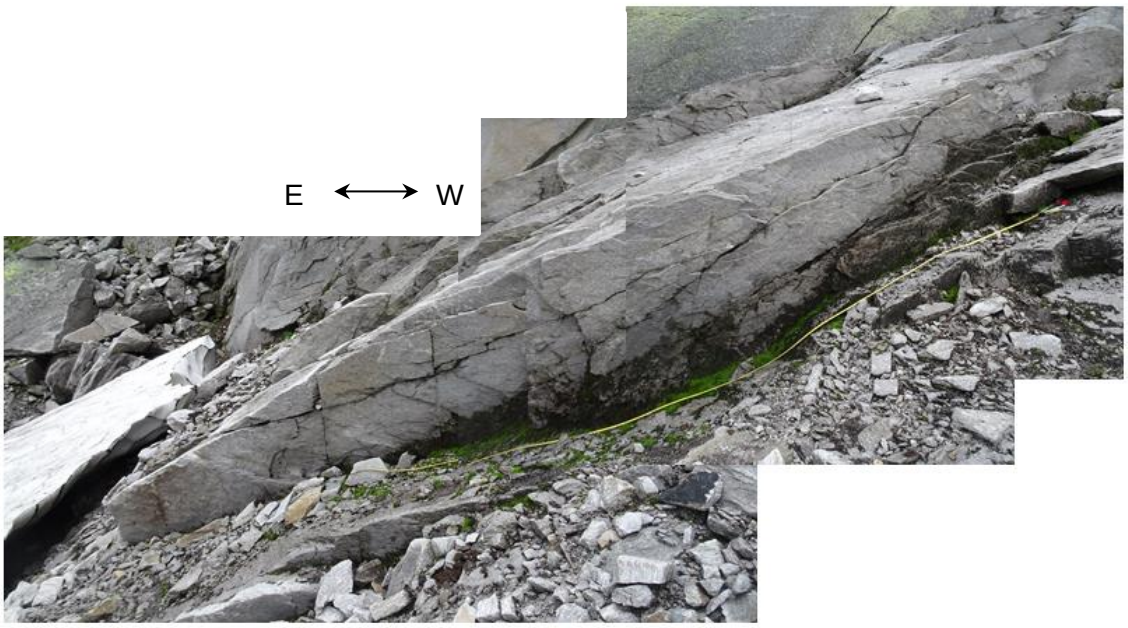

Figure 43 Set up of scanline 5.

In Figure 43 a photograph of the outcrop of scanline 5 can be seen. The scanline mapping aimed to characterize the steeply dipping joints roughly striking north-south (later defined as JS4). Seven joint planes cross the scanline with a length of 7.6 m and the spacing varies between 0.6 and 2.1 m. The mean orientation of the joint planes is 281/86. The joints are persistent as they run across the whole outcrop, which has a height of 2 m. The joint surface is planar.

Table 7 Set up data of scanline 6.

Scanline 6			Outcrop			
Trend	Plunge	Length (m)	Dip Direction	Dip	Height (m)	Width (m)
340	90	1.5	174	82	2	40

Figure 44 Setup of scanline 6, which is vertically oriented.

In Figure 44 the setup of scanline 6 is illustrated. The scanline is vertically oriented and therefore aims to characterize the joints, which run parallel to the ground surface. The scanline has a length of 1.25 m and the spacing of the joints varies between 0.15 and 0.5 m. The mean orientation of the joint set is 086/36 and the joints are persistent and are wavy.

7.8.2 Stereonet projection

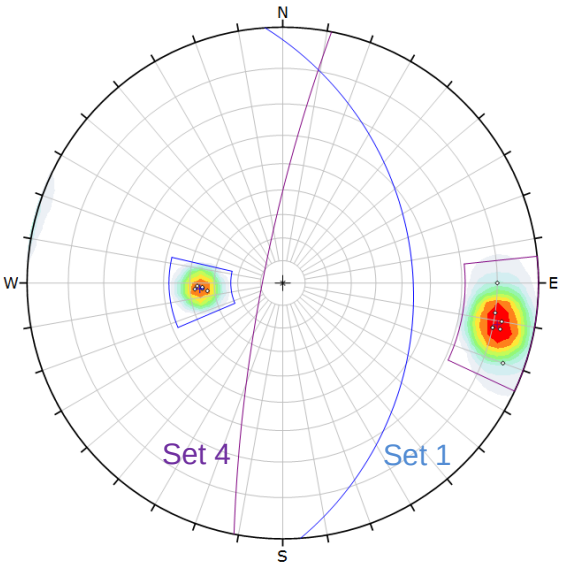

The orientation data obtained during scanline mapping 5 and 6 is displayed in Figure 45.The pole points belonging to Set 4 are measured during mapping of scanline 5 and the data belonging to Set 1 correspond to the vertically oriented scanline 6. The mean orientation data of Set 1 is 086/36 and of Set 4 281/86.

Figure 45 Stereonet projection of orientation data measured during scanline mapping 5 and 6.

7.9 Outcrop 9

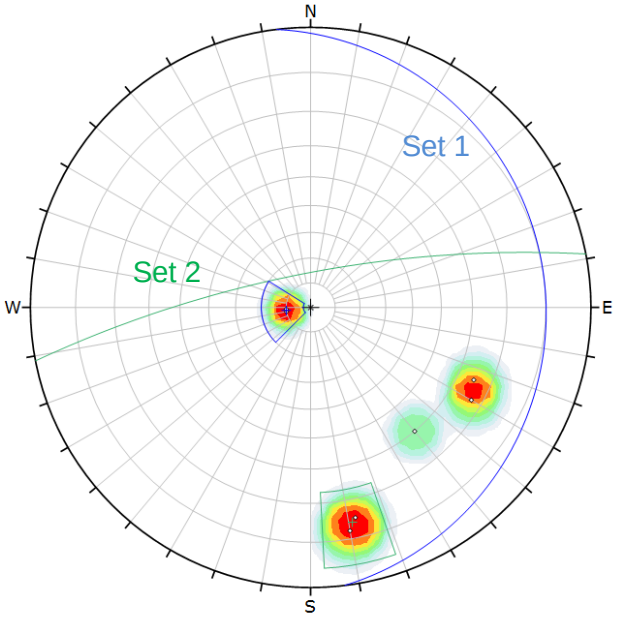

Figure 46 Stereonet projection of orientation data measured at outcrop 9.

At outcrop 9 seven measurements were conducted. Two sets can be defined, but three measurements cannot be assigned to a specific joint set. The mean orientations of the sets are 083/10 (Set 1) and 349/76 (Set 2).

7.10 Statistical assessment and summarizing description of results

Four dominant joint sets (JS) could be defined using the data obtained during the field survey:

Table 8 Joint Set characteristics.

	JS1	JS2	JS3	JS4
Dip direction [°]	78 ± 20	170 ± 20	259 ± 20	276 ± 15
Dip [°]	31 ± 15	89 ± 20	33 ± 15	81 ± 10
Spacing [m]	0.15 - 0.35	0.1 - 2.1	0.4 - 1.5 (5)	0.13 - 2.1
Persistence [m]	0.1 – 0.3	0.2 – 15	1 – 1.5	0.1 – 8
Lithology	Granitic Gneiss			
Surface Morphology	Rough and undulating (cm scale)	Slightly rough, stepped	Planar surface, not rough	Slightly rough
Surface Weathering	Slightly	Slightly	Slightly	Slightly
Aperture [mm]	Visible, 1- 10	Visible, 0 - 10	Very low aperture, 1 - 2	Visible, 2 - 10
Set color	Blue	Green	Red	Purple

7.10.1 Joint Set 1

Joint set 1 is moderately dipping to ENE with a mean dip direction and dip of 078/31. The joints are parallel or nearly parallel to the ground surface of the valley. The spacing is relatively low with a few cm to 0.3 m (Figure 47 A, B and F) and it seems to decrease while getting closer to the surface. The persistence ranges between a few decimetres. After visual assessment, the persistence can be up to 30 m (Figure 47 D). The joint set is therefore very persistent. The joint surface is curved (Figure 47 A), has a high roughness and is undulating in a cm scale. Aperture between the joint surfaces is often visible with a length of up to 1-2 cm. Most surfaces are weathered, but some fresh surfaces could be detected were planar

sliding probably just exposed the rock surface (Figure 47 D). At some locations, water flow through the joints is recognizable. JS1 is the most frequent joint set and therefore very dominant in the landscape scenery. The joints cut most other geological structures and seem to have a high impact on the landscape evolution.

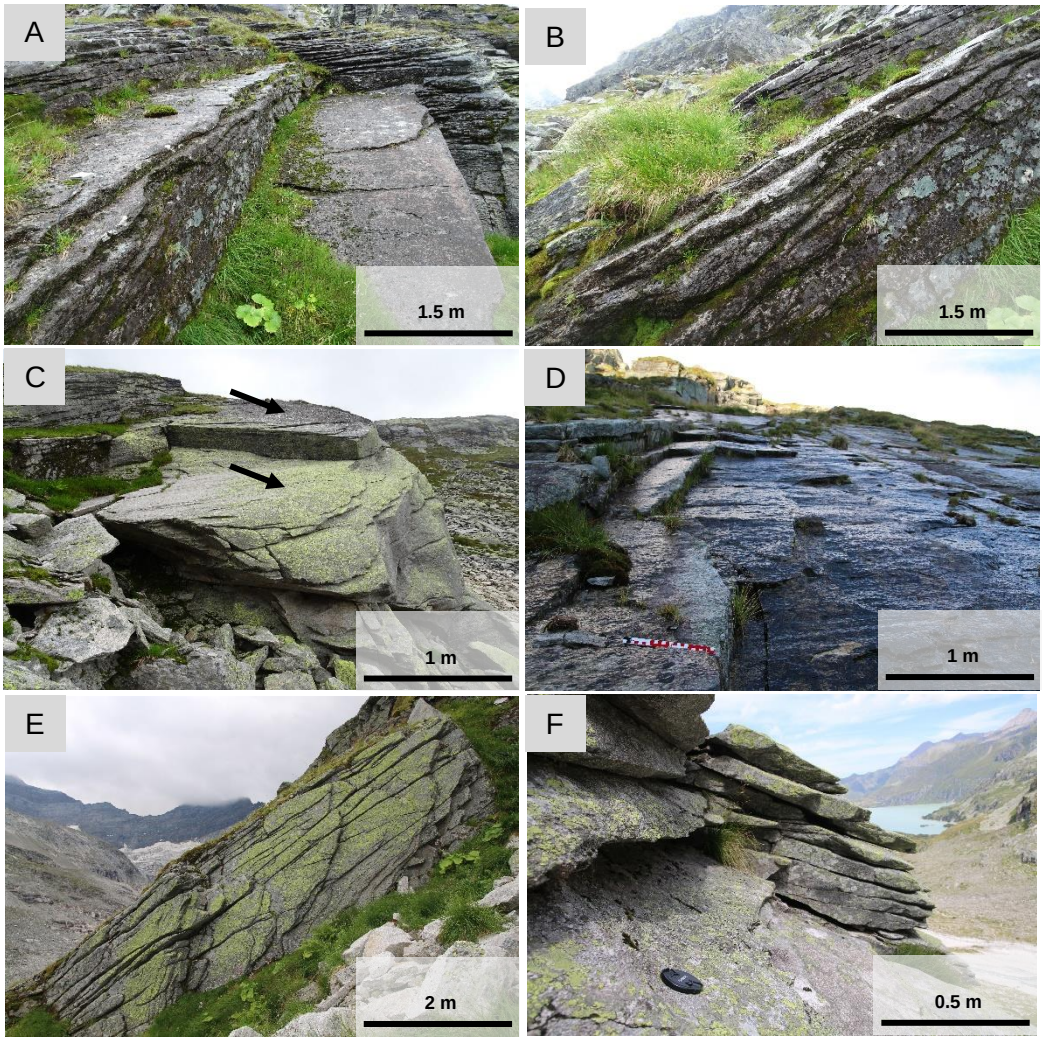

Figure 47 Photographs of Joint Set 1 characteristics.

7.10.2 Joint Set 2

Joint Set 2 is perpendicularly oriented to the valley axis (and JS 1) and steeply dipping with a mean dip direction and dip of 190/89. The persistence ranged between a few decimetres to 15 m. After visual assessment, the persistence can reach up to 40 m. The spacing is very variable. Sometimes the set occurs in clusters of several joints with an interval of a few cm (Figure 48 A), but in other locations a single joint is recognizable with a spacing of 2 m (Figure 48 C). The surface is rough and often stepped (Figure 48 D). The joint surface is weathered and often covered with lichens. The aperture is variable in a range of 1 mm (Figure 48 A and B) to 1 cm (Figure 48 C). JS2 also (like JS1) cuts most of the other

geological structures. Further, water flow through the joints was noticeable in some locations.

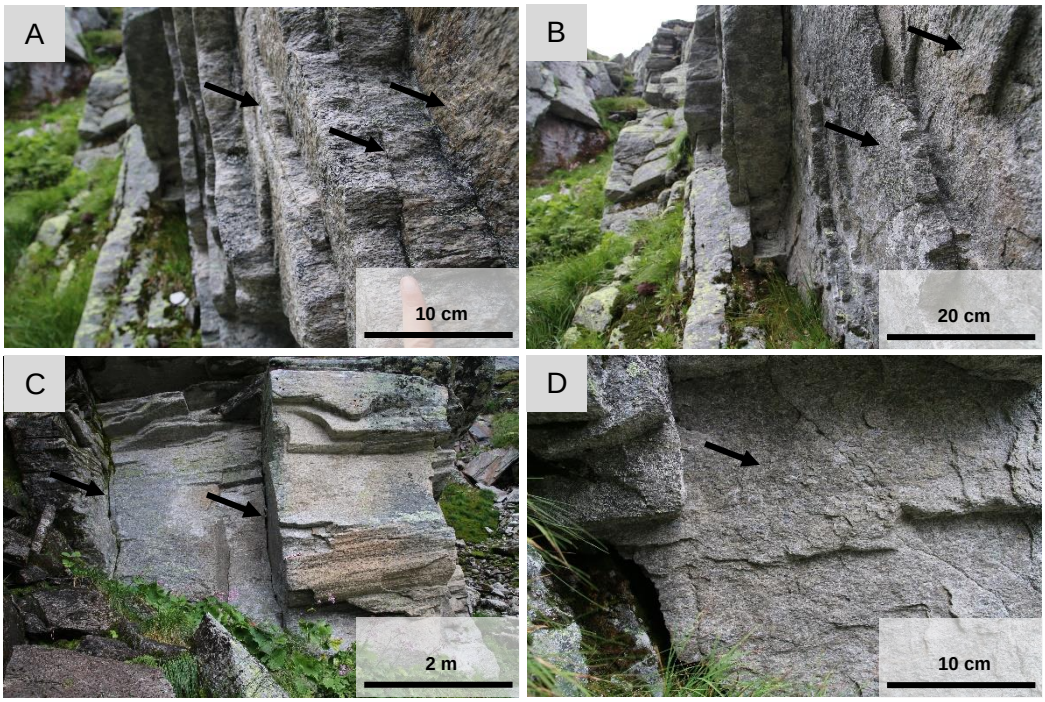

Figure 48 Photographs of Joint Set 2 characteristics.

7.10.3 Joint Set 3

Joint Set 3 has a mean dip direction and dip angle of 259/33 and is oppositely oriented to JS1. The fracture surface has a lower roughness compared to the other joint sets. It is also less persistent, and the aperture is small (approximately 1 mm). Compared to JS1 and JS2 the joints are not curved and JS3 is generally less frequent. The measured spacing is between 0.5 to 1.5 m. The joints are terminating mostly into other joints. This joint set was less prominently recognizable and therefore less fractures were measured. Not enough measurements of spacing and persistency were made to be able to consider these as representative. After visual assessment, the spacing is assumed to be up to 5 m.

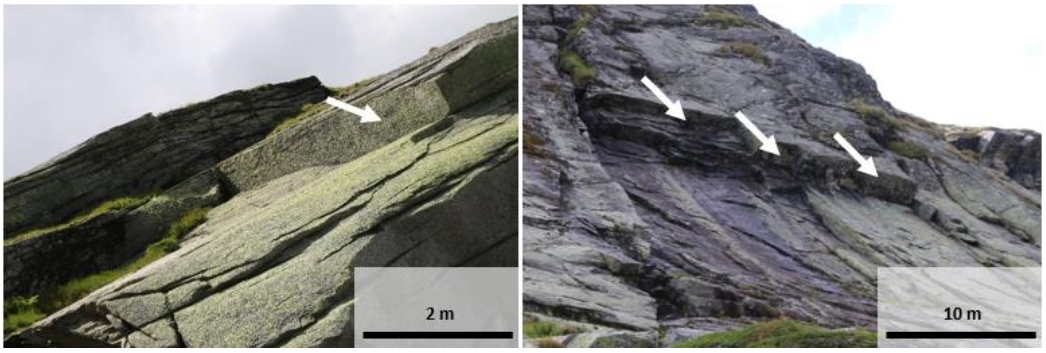

Figure 49 Photographs of Joint Set 3 characteristics.

7.10.4 Joint Set 4

Joint Set 4 is parallel to the valley axis and steeply dipping to NNE. The mean dip direction and dip is 276/81. The persistence ranges between 0.1 m to 1.5 m and termination of the joints is either obscured or in another joint. The spacing varies from 0.1 to 2 m. The surface is planar and slightly rough. Aperture was visible and ranged between 1 to 10 mm. This joint set was only at some rock exposures noticeable, also because of its orientation parallel to the valley axis.

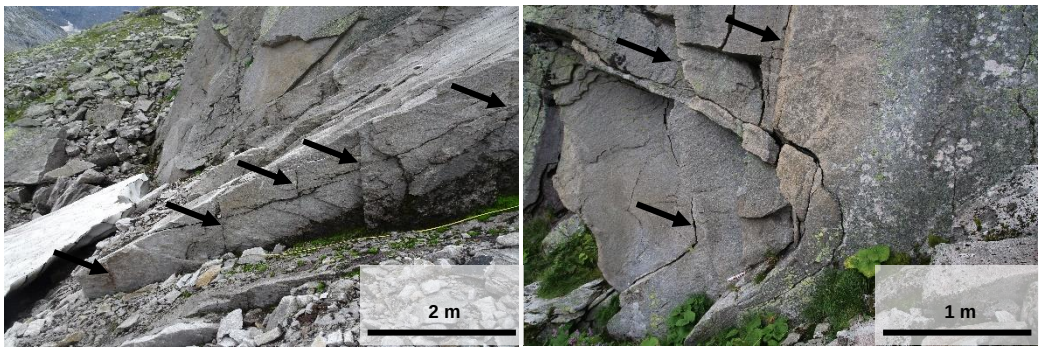

Figure 50 Photographs of Joint Set 4 characteristics.

7.10.5 Relative spatial pattern of Joint Sets 1 - 4

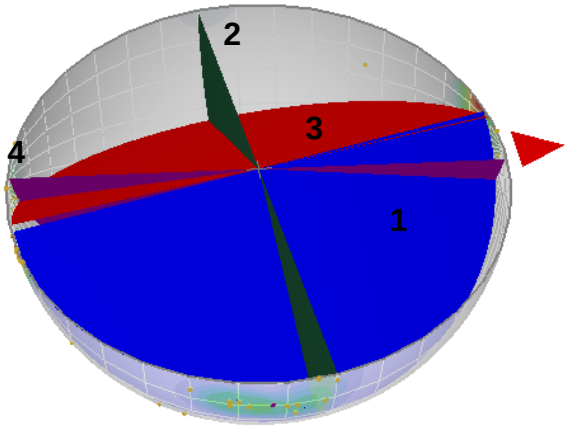

Figure 51 3D Plot of Joint Sets 1-4.

In Figure 51 a 3D plot of the joint sets is displayed to demonstrate the spatial pattern of the discontinuities. The blue plane indicates JS1, which is roughly parallel to the valley surface. JS3 (red plane) is dipping in eastern direction, roughly orthogonal to the slope surface. The green plane represents JS2, which is steeply dipping and intersects JS1 and JS3 perpendicularly. JS4 is roughly equally oriented like JS1 and JS3 but a bit more in eastern direction. It strikes roughly parallel to the valley axis and is dipping steep. The intersection angle of JS1 and JS3 is roughly 90°. The rock mass is generally blocky and undisturbed. The blocks are dominantly rectangular shaped.

7.11 Photographic Analysis

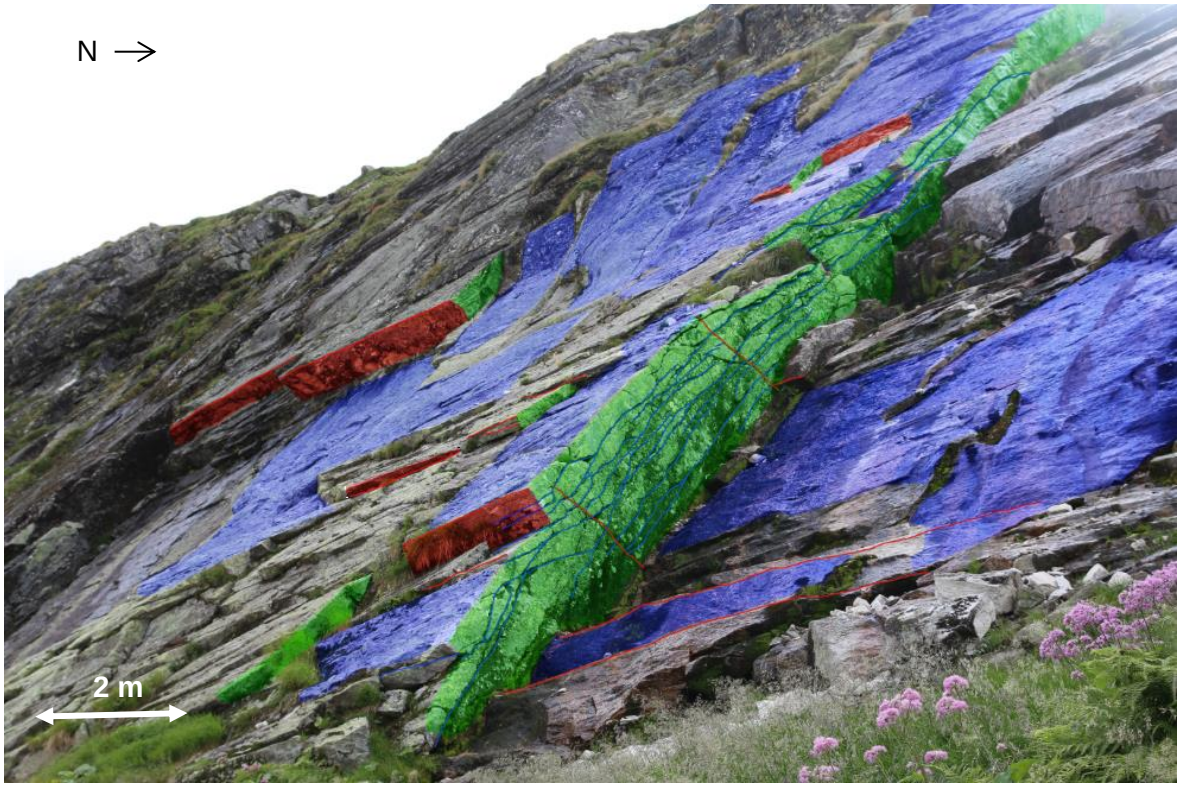

Figure 52 Local pattern of Joint Sets displayed in the 3D plot (same color).

In Figure 52 a slope facing NEE is displayed. The location is marked (red dot: P1) in the map of Figure 30. JS1 (blue) is the most dominant joint set, running roughly parallel to the ground surface. The curvature and the stepped joint surface can be seen on the photo. The joints are cutting the rock mass in elongated rock slabs, which are irregularly shaped. JS3 (red) includes more planar joint surfaces and is less frequent. JS2 (green) is cutting the joint sets perpendicularly. JS1 and JS2 are very persistent with up to 50 m. The lowest spacing corresponds to JS1 with an average length of 10 cm. The spacing of JS2 is on average a bit larger with around 1 m.

Figure 53 Photographic analysis of the joint network.

The slope shown in Figure 53 is marked in the map (P2) in Figure 30. It is located further south and closer to today's glacier, facing east. The landscape scenery is dominantly embossed by JS1 (blue) and JS2 (green) with JS1 forming the cross-profile shape of the valley and JS2 cutting the rock mass vertically. Many steps are recognizable on the surface of JS1. Changing frequency of JS2 can be noted with higher frequency in the middle part forming thin vertical layers. The frequency is decreasing in the direction of both sides.

7.12 Digital Elevation Model Analysis

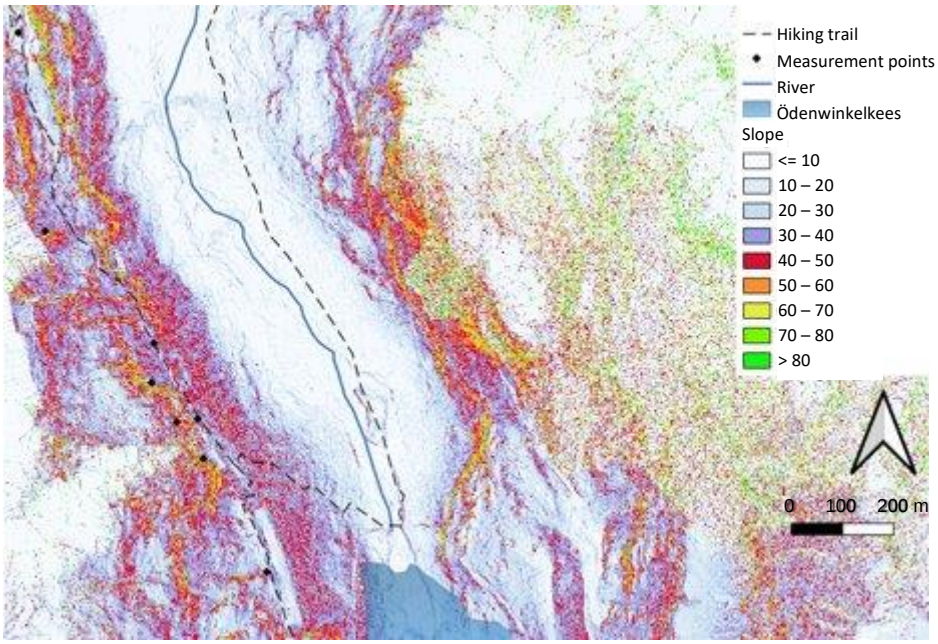

Figure 54 The dip angle of the slope. The DEM, used as base data, is provided by Georesearch mbH.

The DEM is provided by Georesearch Forschungsgesellschaft mbH, a non-profit, non-university research institution based in Puch/Hallein. They gathered surface elevation data by photogrammetric data from UAS flights for one of their research projects to get more information about the influence of glacier randkluft systems on rockfall (Georesearch, 2020). With the data a high-resolution DEM can be created. The DEM was then analysed using the Open-Source-Program QGIS (QGIS, 2020). Raster point information can be used to calculate the slope angle in the study area. This is convenient to determine steep parts of the rock wall as these locations may be more susceptible to rock slope failure. For the kinematic analysis, the mean slope angle is defined using interpolated profiles of the valley. Steeper steps of rock walls formed by erosion and a resulting change of relative orientation between rock slope and joint surfaces are neglected. The mean surface angle is equal to 30°, but there are steeper rockwalls within the study area. In Figure 54 these areas are marked as the slope angle below 40° is coloured blueish, above 40° is coloured red and steep rockwalls with 60 to 90° are coloured yellow and green. These areas may be of special interest for the stability assessment because the probability of failure is higher. Steep rockwalls within the study area are shown on the photograph in Figure 55.

Figure 55 The mean slope angle might be stable but there are steep and exposed rock walls that may be prone to fail. For example, the highlighted areas.

7.13 Kinematic Analysis

The densities are highest for JS1 and JS2, which implies that most of the measurements can be related to these JS (Figure 56). For the stereoplots, all projections are lower hemisphere and equal angle, a friction angle of 30° was estimated and lateral limits of ± 20° from the slope orientation are assumed for both planar sliding and toppling.

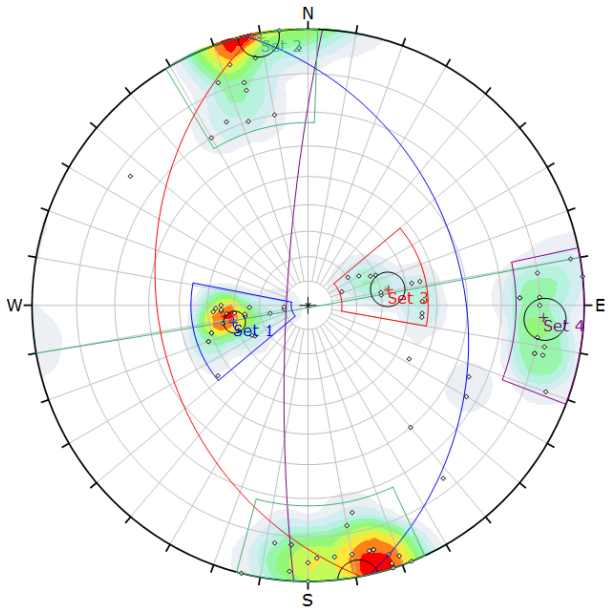

Figure 56 Stereographic pole plots of Joint Sets 1-4. The projections are lower hemisphere. Density concentrations are colored in steps of 1.3%. Confidence cones for two standard deviations (95%) are given for each set.

The stereographic plots of Figure 57 show the critical zones (highlighted in red) for planar sliding, wedge failure, flexural toppling and direct toppling. For planar sliding and flexural toppling, the pole vectors of the planes are used. For wedge sliding and direct toppling the intersection points are displayed. The average slope angle determined with the DEM using QGIS (QGIS, 2020) is 30°. The stereoplots displayed in Figure 57 were conducted assuming a slope angle of 40° and 50°. Kinematic analysis is also conducted for higher slope angles because there is a prominent area with a steeper slope (> 30°) as it can be seen in Figure 54. Further, the maximum measured dip angle of the slope parallel joint set (JS1) was 45°. Steeper parts of the rock wall are neglected using the average slope angle. Erosion can lead to angular unconformities and steep rock steps that might especially be prone to fail. For the assessment of the stability of steep rockwalls a kinematic analysis with a maximum slope surface angle of 50° was conducted.

Table 9 summarizes the resulting percentages of critical discontinuities for each kinematic failure mode for slope angles of 30°, 40° and 50°. Additionally, a sensitivity analysis for a varying slope dip was conducted, which is displayed in Figure 58.

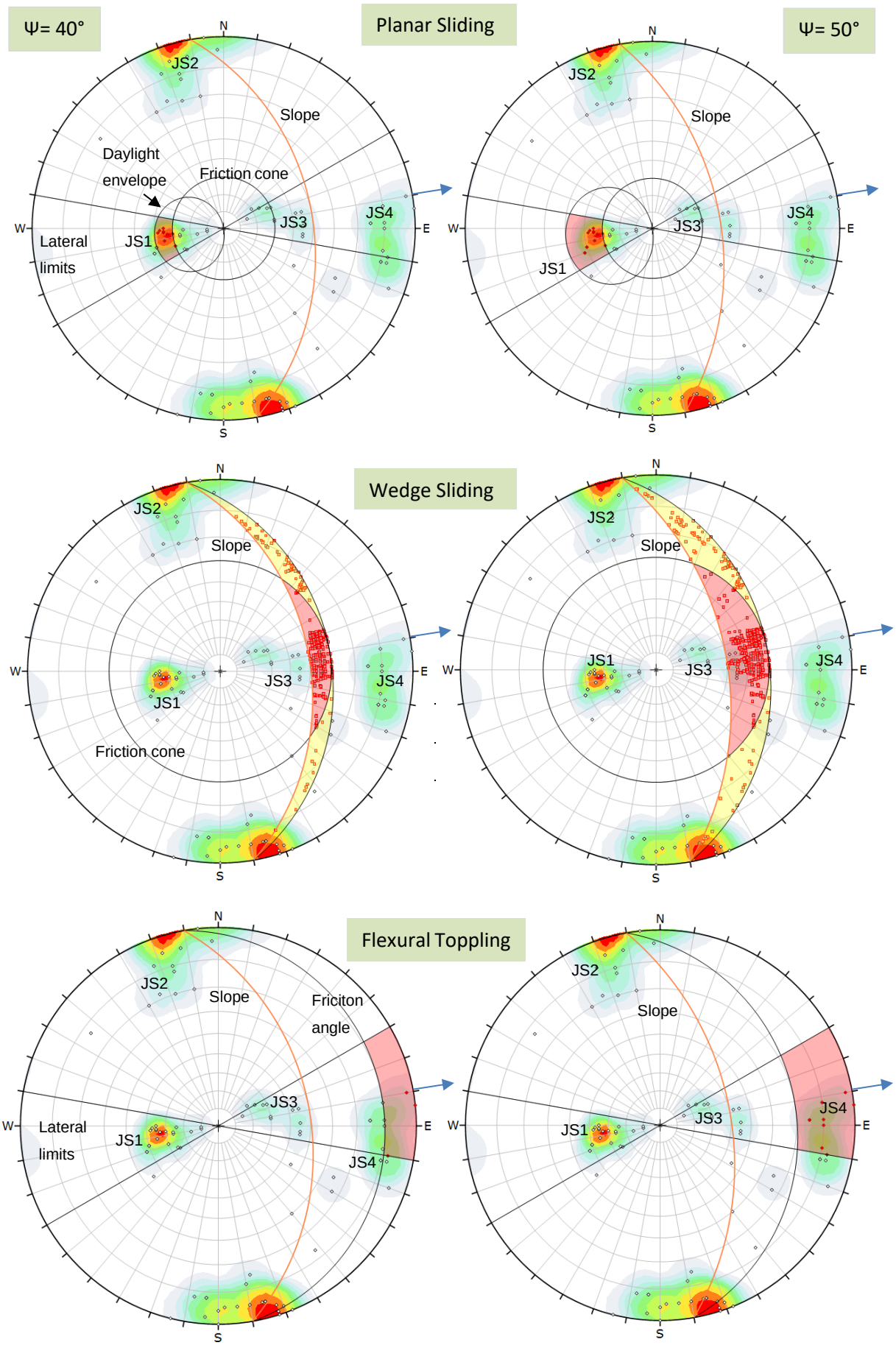
Ψ= 40°
Planar Sliding
Ψ= 50°
N
S
W
E
JS1
JS2
JS3
JS4
Slope
Daylight
envelope
Friction cone
Lateral
limits
Wedge Sliding
Friction cone
Flexural Toppling
Friciton
angle

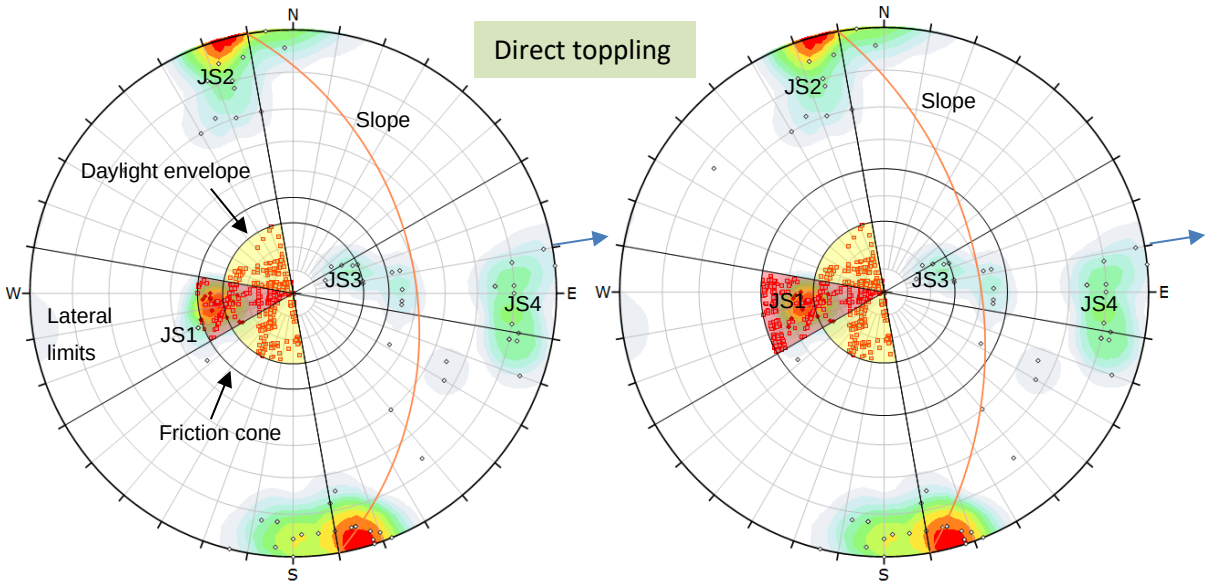

Figure 57 Kinematic analyses. With a slope dip direction of 80° and dip angle of 40° and 50°. A friction angle of 30° and lateral limits of 20° is assumed. The projections are lower hemisphere and equal angle. Critical zones are highlighted. The direction of movement is marked with the blue arrow.

Table 9 Percentage of critically oriented discontinuities resulting from the stereographic kinematic analysis.

Failure Mechanism	Slope Dip = 30°	Slope Dip = 40°	Slope Dip = 50°
Planar Failure (JS1)	0 %	10.59 %	15.29 %
Wedge Failure	0 %	13.05 %	18.95 %
Direct Toppling direct/oblique/base plane (JS1)	4.86 % 11.51 % 11.76 %	5.92 % 11.51 % 22.35%	10.72 % 11.51 % 24.71 %
Flexural Toppling	0 %	3.58 %	10.59 %

Table 9 shows that there are no critically oriented discontinuities for planar/wedge sliding and flexural toppling with an average slope angle of 30°. For direct toppling 4.86 % of the discontinuities are critically oriented. JS1 builds the base plane and 11.76 % of its discontinuities are critically oriented. Assuming a slope dip of 40° the number of critically oriented joints is increasing. For planar failure it is 10.59 % and only discontinuities of JS1 are critical base planes. Under the assumption of a slope dip of 50° it is further increasing with a maximum of 15.29 %. For wedge failure the critically oriented discontinuities are increasing by 13.05 % using a slope angle of 40° and by 18.95 % for a slope angle of 50°. It is noticeable from the stereoplot that wedge sliding occurs on the intersection plane from JS1 and JS2 (Figure 57 B). The intersection points of JS1 and JS4 are critically oriented for

direct toppling. The percentage is slightly increasing for a slope angle of 40° by approximately 1 %. Joint planes from JS1 are working as base planes for this failure mechanism. 22.35 % of JS1 are favourably oriented for direct toppling. The number of critical discontinuities for flexural toppling is increasing by 3.58 % due to the orientation of JS4. For a slope angle of 50° it is further increasing to a maximum of 10.59 %.

A sensitivity analysis for the different failure mechanisms was conducted to observe the influence of the slope dip angle to the percentage of critically oriented discontinuity planes (Figure 58). For planar sliding a recognizable step of increase can be noted between a dip angle of 35° to 40°. The total increase of 15.3 % is reached at an angle of 43°. A further increase of the dip angle up to 50° does not have an impact on the percentage of critically oriented discontinuities. For wedge sliding the biggest incline is recognizable within a slope dip angle interval of 35° to 43°. For flexural toppling the critical percentage starts to increase recognizable with a slope angle of 40° and higher. The critical percentage for direct toppling increases at a slope angle of 45° and higher.

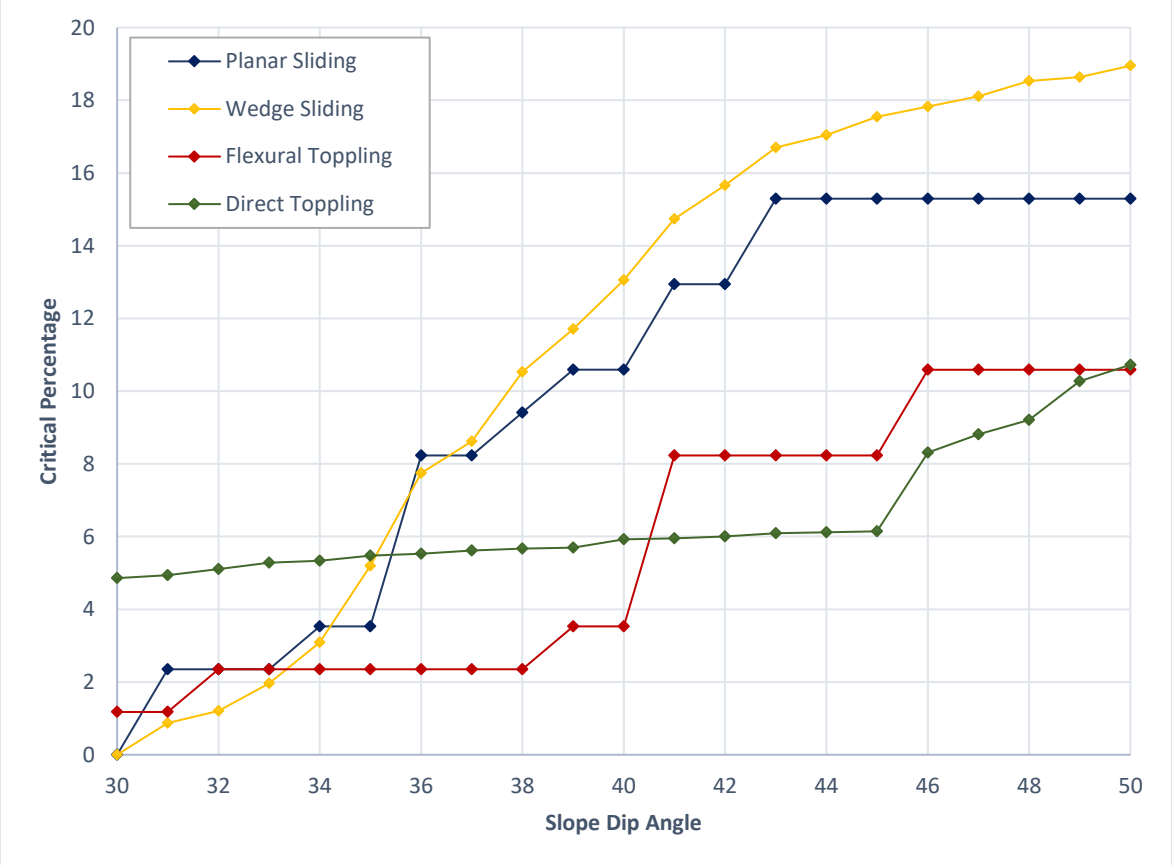

Figure 58 Sensitivity analysis of the slope angle varying from 30° to 50°.

8 Discussion and Interpretation

8.1 Exfoliation joints

JS1 and JS2 are more dominant in the landscape scenery than JS3 and JS4. Further they show a higher persistency. The surface is extremely rough and curved, which cannot be related to tectonic joints. JS1 and JS2 cut most other geological structures and the joint network produces a blocky rock mass. Increasing spacing with increasing depth below the slope surface is typical for exfoliation joints. To be able to determine these properties, discontinuities must be mapped in greater depth, for example using borehole data. However, the tendency of increasing spacing of JS1 was recognizable during fieldwork, but this observation is only based on exposed rock masses. The variation of aperture is characteristic for exfoliation joints. Apertures larger than a centimetre are rarely observed along other kinds of joints (Martel, 2017). Apertures of up to 1 cm were only recognizable for JS1 and JS2. The other two JS had low apertures with up to 1 mm. They cut all other geologic structures in a rock mass and no relative displacement can normally be observed, which is also true for JS1 and JS2. In some locations, JS1 has a splay shaped pattern as marked in Figure 59.

Figure 59 Splay shaped pattern of JS1.

Exfoliation joints typically have water running through their joints because of their high persistence, aperture, and connection to other joint sets. The pictures in Figure 60 show water flow through the joints of JS1 and JS2, which could be recognized at several locations within the study area.

Figure 60 Water flow through very persistent joints. Left through JS1 (Outcrop 4) and right through JS2 (Outcrop 5).

Changing orientation dependent on the valley surface is typical for exfoliation joints and excludes a tectonic origin. To proof this, measurements of the discontinuities on the opposite valley side would be necessary. Reaching the opposite side was difficult during the field work. Therefore, the comparison of the valley sides is based on photographic analysis even though the rock slope was mostly covered by debris (Figure 61).

Figure 61 The opposite side of the valley is mostly covered by debris.

In Figure 62 photographs of the east side of the valley (opposite side of the study area) is illustrated. Joints which formed parallel to the slope surface can be recognized (Figure 62 A) and these are changing the orientation dependent on the surface geometry. This joint set is equivalent to JS1 on the western valley side. Therefore, this is an additional indication, designating JS1 as exfoliation joints.

JS2 is more difficult to detect on a photograph of the opposite valley side. On Figure 62 B discontinuities can be seen which roughly striking east west and steeply dipping. To surely indicate if these discontinuities correspond to JS2, compass or scanline measurements are needed. It has to be checked if these discontinuities change their orientation, probably so that they are always roughly perpendicular oriented to the glacier flow direction.

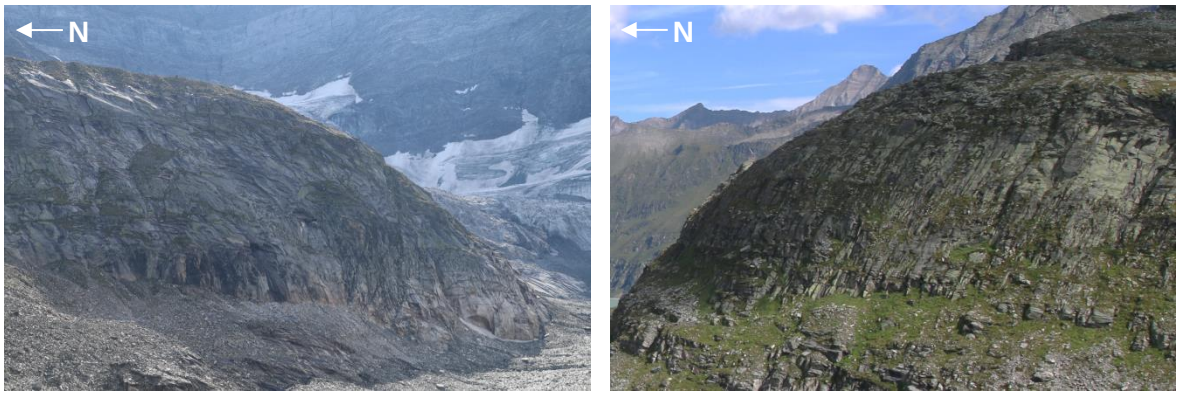

Figure 62 Photographs of the rock slope on the opposite side of the valley. (A) Left: The same slope parallel joints can be recognized. (B) Right: Steeply dipping joints that may be equivalent to JS2.

8.2 Failure Mechanisms

Glacial erosion leads to very steep slopes right after deglaciation. In order to reach an equilibrium, gravitational failure mechanisms occurred, which contributes to valley widening and slope angle decrease (Hartmeyer *et al.*, 2020). In hard-rock slopes the joint geometry controls the dominant failure mode. Key parameters for hazard assessment are the angle between the discontinuities and the slope, coupled with the trace length and spacing of the discontinuities (Wyllie & Mah, 2005).

Kinematic analyses derive that planar and wedge sliding are the dominant failure modes in the study area. The moderately dipping and daylighting joints of JS1, parallel or nearly parallel to the slope surface, create favourable planes for sliding. The formation of JS1 is contributing to an increasing probability of planar failure as only joint planes from this joint set are critically oriented. In total, 60 % (at a slope angle of 50°; 40 % at a slope angle of 40°) of the planes of JS1 are critical to planar failure. In Figure 63 a photograph of joint surfaces of JS1 as planar sliding planes are illustrated.

Figure 63 Planar sliding surface on JS1.

It shows that the rock mass in the middle section of the photo is still stable but may be also prone to fail. It is obvious that in the study area planar sliding on JS1 occurred and dominantly formed the landscape. The joints are roughly parallel to the slope surface and as soon as the joints are daylighting failure might occur. Therefore, the orientation of the joint set relative to the slope surface is an important factor. Minor changes in the slope angle have a high impact on the occurrence of daylighting discontinuities. The orientation of JS1 and the slope surface varies over short distances leading to either favourable to unfavourable stability conditions as it can be seen in Figure 64. The average dip angle of JS1 is 31°. If the slope angle is steeper than 31° the joints are daylighting and create an unfavourable stability condition. If the slope angle is lower the joints are in dipping.

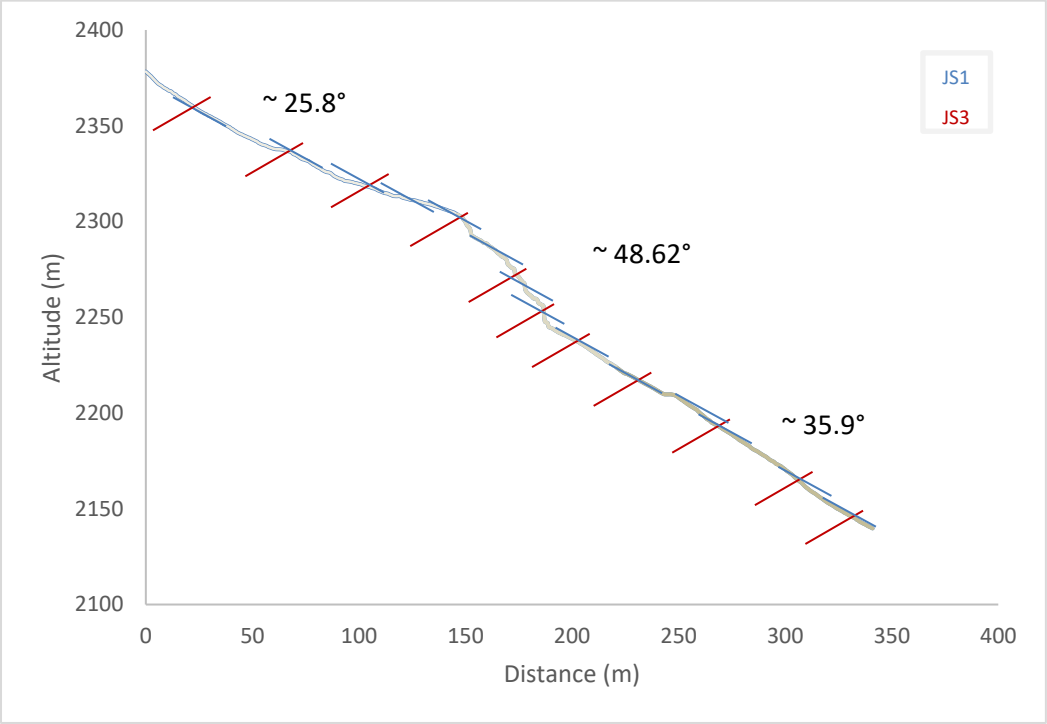

Figure 64 Cross Profile of the slope with the mean orientation of JS1 (blue) and JS3 (red) relative to the slope.

There are also daylighting joints from JS1 recognizable (which can also be seen in Figure 63), where failure haven't occurred yet. These rock blocks might be stable due to intact rock bridges. The stepped surface of JS1 is, especially on the left side, visible, which is an indication of rock bridge failure. After failure the amount of rock bridges initially stabilizing the rock mass can be assessed. JS1 sets up the base for release planes of potential rockslides and rockfalls. Thus, JS1 modified the general shape of the valley morphology. JS3 builds the tear-off edge of rock masses during planar sliding failure along JS1. The intersection plane of JS1 and JS2 is most critical for wedge sliding.

Toppling is another failure mode that can occur in the study area. The kinematic analysis indicates that direct toppling occurs on critical oriented intersections of JS1 and JS4. Flexural toppling might occur at joints of JS4. This might be theoretically feasible but unlikely to occur because the spacing of JS4 is too large for toppling to occur.

In Figure 65, a rock mass in the study area that is prone to toppling is shown. There slope parallel joints which appear curved, favour the instability in the upper part. Fracture propagation through intact rock may have played a dominant role creating this potential failure mechanism. In the bottom of the rock mass, these joints connect to discontinuities of JS3 and build a persistent discontinuity. JS3 terminate again in slope parallel joints which are dipping less steep. In the upper part of the rock mass the joint's aperture is in a range of a few cm (white arrows in Figure 65) and therefore prone to fail. The dominant failure mechanism differs with changing orientation and frequency of JS1. As Figure 65 shows,

JS1 is less frequent, bigger, and less flat-shaped rock blocks are generated. JS1 is curved and dipping steeper, compared to Figure 63. The joint sets 1 and 2, and the surface geometry play key roles in controlling the failure mechanisms. Kinematic analyses show the high influence of JS1 and JS2 on the slope instability as failure just depends on the orientation of these joint sets.

Figure 65 Rock mass prone to direct toppling.

The joint sets developed due to the deglaciation process contribute a lot to an increasing probability of failure. The relative orientation of the joints of JS1 to the slope orientation may have the highest impact on the failure mechanisms. The dominant failure mechanism differs with changing orientation and frequency of JS1. Figure 65 points out that, JS1 is less frequent and therefore bigger and more rectangular rock blocks are generated. JS1 is curved and dipping steeper, compared to Figure 63. The joint sets 1 and 2, and the surface geometry play key roles in controlling the failure mechanisms. Kinematic analyses show the high influence of JS1 and JS2 on the slope instability as failure mostly depends on the orientation of these joint sets.

The rock mass may not have failed yet because of intact rock bridges. The deglaciation process formed intermittent joints. The different joint sets are creating separated intact rock blocks. These blocks can be kinematically free but still do not fail due to the presence of intact rock bridges. With time after deglaciation the stress distribution in the rock mass changes, joints propagate, which can lead to intact rock bridges failure. Further, the rock blocks are stable because of increased friction.

In Figure 66, buckling of the rock mass can be observed. The principal stress σ1, parallel to the rock surface, is high compared to the confining horizontal stress σ3. JS2 formed thin layers and because of the high stress ratios that is acting on the rock mass it starts to buckle.

Figure 66 Buckling of rock slabs bounded by sheeting joints.

8.3 Joint propagation

The surface parallel joint sets (JS1) formed due to large in-situ stress ratios. Principal stresses parallel to the slope surface are large compared to low principal stress normal to it. The analysis of fracture surfaces suggest that intact rock bridges are present before failure occurs. High joint surface roughness and steps indicate rock bridge failure. An irregular geometry of joint surfaces can be observed on joint surfaces corresponding to JS1 and JS2, especially where JS2 is very frequent. The irregular geometry is at a scale of dm to a few m. This pattern indicates rock bridge failures caused by the propagation of wing cracks. Wing cracks form typically perpendicular to the pre-existing cracks and are curved (Duriez *et al.*, 2016). This can be a reason for a stepped rupture surface. Step-path failure connects pre-existing joint planes through the previously intact rock. This process progressively weakens the rock slope and can lead to failure even if it is initially stable (Huang *et al.*, 2014).

JS1 and JS2 are very persistent discontinuities and therefore prone to fail. There must be a sufficient amount of rock bridges, which stabilize the rock block and prevent failure.

8.4 Time pattern of joint development after deglaciation

The rock slope characterized in the following part is on the eastern side of the valley oppositely located to the rock slopes discussed earlier.

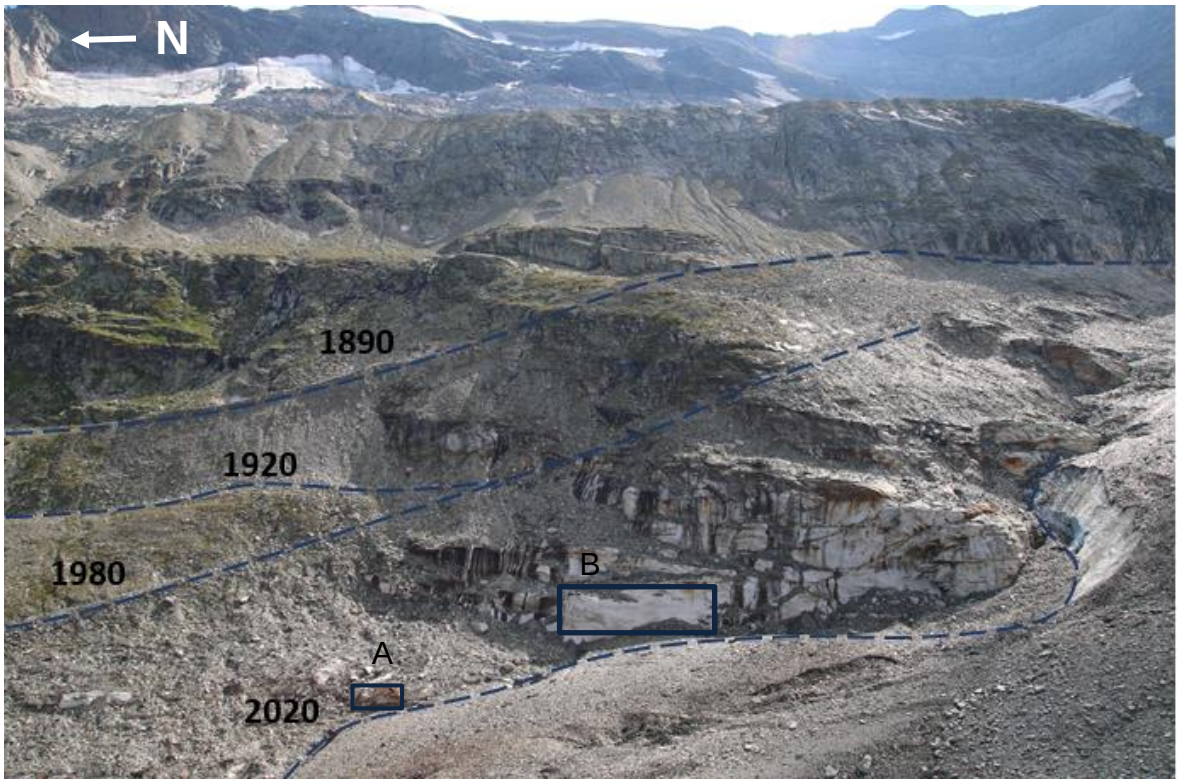

Figure 67 The different moraines and the corresponding times are marked. The white rock mass is exposed from the glacier during the last 40 years. A and B mark locations where glacial marks can be seen on the rock surface.

For the assessment of time needed for the propagation of the exfoliation joint network, photographic analyses were conducted. The rock mass that is illustrated in Figure 67 became ice-free during the last 40 years. Glacial marks are recognizable on the surface of the rock wall (Figure 68), which indicates an even shorter ice-free time period of a few years at the bottom of the rock wall. No discontinuities are recognizable on the rock mass surface.

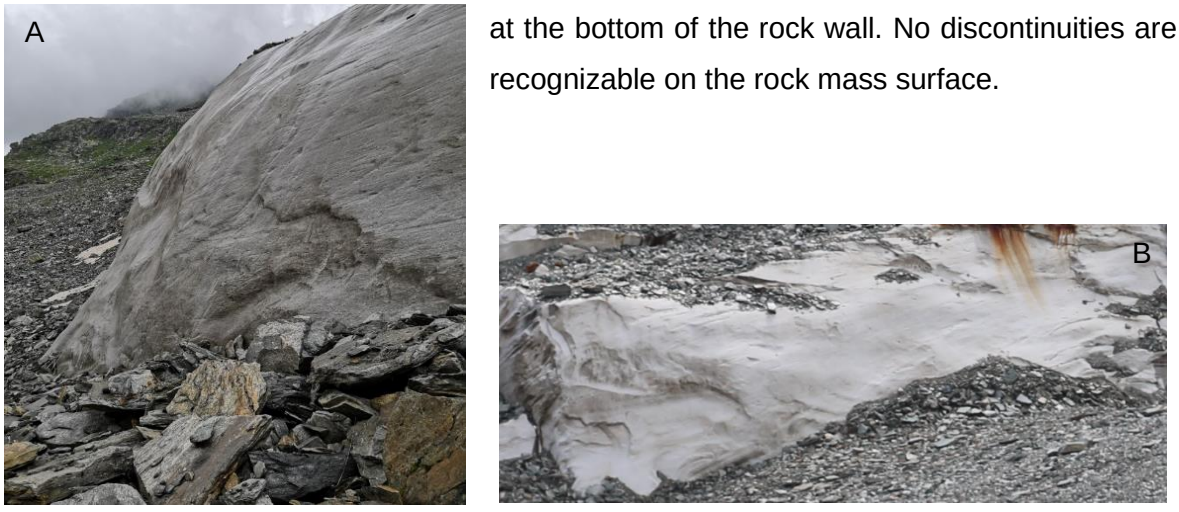

Figure 68 Glacial abrasion marks on the rock surface.

Figure 69 Photographic analysis of a rock mass that is deglaciated since a few years (approx. 5).

The rock slope in Figure 69 is located on the eastern side of the valley and deglaciated since a few years. There are not as many discontinuities recognizable in the rock mass which formed parallel to the slope surface. These parallel discontinuities are marked with the blue area. The JS is less dominant. The rock mass in the bottom on the left side does not show any joints at the surface. Therefore, glacial marks are visible. It indicates that this part became ice-free during the last few years. In general, there are not as many slope parallel joints visible. In the rock mass in the bottom on the right side slope parallel joints may have just developed. Only a few associated joint surfaces are visible.

According to photographic assessment there are joints that are roughly horizontal (yellow) with a trace-length ranging from 1 to 10 m. Other joints (pink) are moderately dipping in northern direction crosscutting most other geological structures. These are parallel to the orientation of the glacier moraines and seem to be more persistent with a visually assessed trace-length of up to 20 m. The green marked joints are dipping steeper in northern direction and are less persistent with up to 1 m. These are nor as dominantly distributed as the other joints. The dark coloured areas indicate water flow through the joint sets.

The rock mass has not reached equilibrium and some joints develop in the present time. In the detailed photograph, joints, which are presently forming can be seen. On the left side

a joint terminates in the rock and small fissures bent downwards are forming (white arrow). The small rock blocks cut by the joint network fail along the slope parallel joint plane and slide down. These rock blocks may fail soon. On the right side two rock blocks may slide down soon on the slope parallel surface (black arrow). In the middle section several rock blocks formed due to crosscutting joint sets that are horizontal, parallel and perpendicular to the valley axis. Beneath the horizontal joint (yellow marked joints) rock blocks detach from surface parallel joint planes (blue marked), cut by the horizontal joint and the surface parallel joint. There is probably a lower joint spacing in this area because of a high load that was applied by the glacier. The rock mass is curved there, and the glacier flow direction is in the left direction so that the glacier may have squeezed against this part of the rock mass. High stresses are therefore applied on the stoss side (right side of the picture) and the part on the left side experiences very low stresses, where a cavity between the glacier and rockwall might have formed. High stress ratios evolve and fractures develop in the low pressure zone (Carol, 1947).

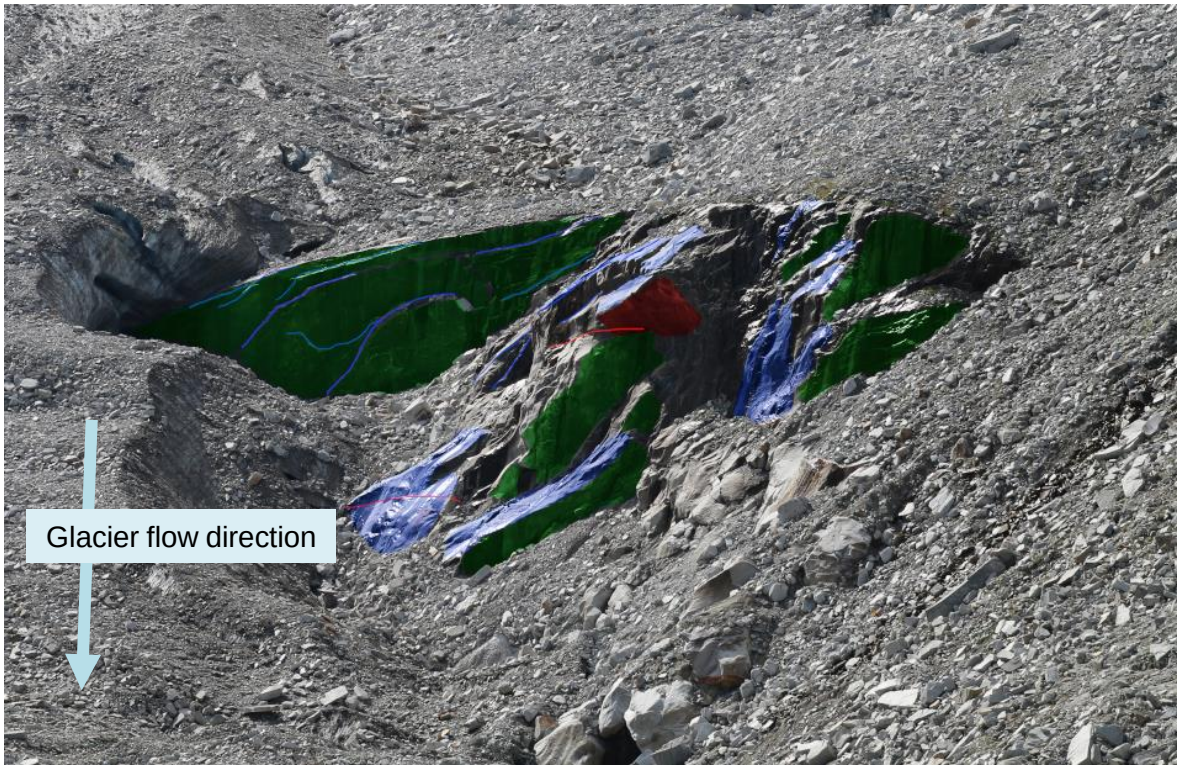

Figure 70 Photographic Analysis of a rock mass which recently became ice-free.

In Figure 70 a photograph of a rock mass that recently became ice-free, is illustrated. The different joint sets are coloured to assess the time needed for the joints to develop. JS1, parallel to the slope, and JS2, perpendicular to JS1, developed already. It can be noted that the spacing of JS1 is larger compared to the higher altitude observations close to the hiking trail. It can be assumed that the rock mass became ice free during the last 20 years. The time seems to be enough to develop the first joints of each JS but during the next year more joints may develop to reach an equal spacing to the pattern further up. Even more fractures

may develop because the load of the glacier is larger than it was at the measurement points at the hiking trail. If more load releases, more exfoliation joints form. Glacial erosion like plucking may play an important role in this location. The joints may develop because of local pressure applied by the glacier flow direction. High stresses evolve at the stoss side of the rock mass and low on the lee side, which leads to fracture propagation in the low pressure zone as explained in section 3.4.3. High pressures beneath a glacier also leads to a thin water layer between the glacier and bedrock. The water may infiltrate into the fractures and as soon as the pressure is released it refreezes again. This might drive further fracture propagation detaching rock blocks, which are then carried away by the glacier. Afterwards new fractures are built within the bedrock (Carol, 1947).

8.5 Spatial pattern

The measurements were made along the hiking trail with a total distance of 1200 m. Along this length the valley slope is oriented in the same direction. Therefore, the dip direction of the measured joint surfaces cannot be correlated to the valley slope orientation. Exfoliation joints also change the dip angle related to the height of the valley wall. In the valley and at the crest the joints are not as steeply inclined as in the middle part following the overall structure of the topography (Hencher *et al.*, 2011). In order to assess the spatial pattern of the discontinuities more measurements at other locations are needed. Additional data at other altitudes or at the opposite side of the valley are necessary to evaluate if the discontinuities change their orientation dependent on the surface geometry.

8.6 Reasons for rock slope failure

The determination of the most dominant process responsible for fracture propagation is complex. Rock slope failure after deglaciation cannot be related to a single event, but to several processes contributing to progressive rock slope weakening.

The rock mass in a glacial environment is subjected to mechanical processes. The development of fractures is dependent on the in-situ stress field. Glacial erosion, oversteepening of the slope and the stress release through glacier retreat are the main factors. The minimum principal stress σ_3 normal to the rock mass can further decrease by reduced ice thickness or erosion of overburden material. It therefore promotes fracturing by decreasing the confining stress on bedrock while maintaining high parallel stresses. Fractures develop in the direction of the maximum applied stress. Increasing the ratio of σ_1 to σ_3 results in a nonlinear increase in stable fracture lengths (Leith *et al.*, 2014a). Granitic gneisses, as there are in the study area, are able to build up high stress ratios. Therefore,

discontinuities with high persistency can develop, like JS1 and JS2.

The formation of new fractures, besides purely mechanical loading, can be due to stresses imposed on the bedrock by thermal and hydrological processes. Liquid water intake in combination with temperatures around 0 °C may have a high impact on the stability of the rock slope. High amounts of precipitation are measured at the weather station Rudolfshütte. Additionally, an increase of air temperature results in a larger amount of snow melt and less days with snow cover or frost and ice. The snow cover as a shield from atmospheric forces is decreasing and the rock mass is increasingly exposed to weathering processes. The amount of liquid water infiltration into the rock mass is increasing. Fracture dynamics are then dominated by thermo-mechanical expansion and contraction of the rock mass (Ewald *et al.*, 2019). The rock slope is exposed to high thermal stresses after the first deglaciation. Afterwards stresses are imposed by diurnal and seasonal temperature variations, which leads to progressive fracture development, especially during spring and autumn (Grämiger *et al.*, 2018). Depending on the amount of intact rock bridges the rock mass might still be stable straight after deglaciation. After glacier retreat rock mass strength decreases progressively over a long period of time. New fractures propagate through intact rock bridges and connect non persistent discontinuities (Fischer *et al.*, 2010). Step-path failure can therefore lead to the final rock slope failure (Xu & Li, 2019).

Nowadays permafrost does not occur at the rock slope surface. According to the topoclimatic key for permafrost from (Schrott *et al.*, 2012), the orientation and altitude of the rock slope is not favourable for permafrost existence. Temperatures are too high during the summer month and the upper part of the subsurface is not permanently frozen. Therefore, permafrost thaw probably does not have a large effect on joint propagation close to the surface but rather in larger depth. Processes like freeze-thaw weathering may play a more important role close to the surface. Nevertheless, permafrost thaw effects play an important role for the general slope stability since deglaciation. The final adjustment to non-glacial conditions might happen after hundreds of years. At this point the bedrock has adapted to non-frozen strength conditions or the slope angle has adapted to the equilibrium angle of permafrost-free rock slopes (Krautblatter & Leith, 2015). Therefore, bedrock fracturing may still be ongoing even after a long time after deglaciation.

9 Conclusion

9.1 Main Results

A rock slope close to the Ödenwinkelkees was geomechanically analysed to assess the effects of (de)glaciation on rock slope stability. Data acquisition was obtained with traditional field work methods like compass measurements and scanline mapping. Additional photographic analyses of the rock slope and stereographic projection of the measured data using the software Dips 7.0 (Rocscience, 2020) lead to the characterization of four different joint sets:

- Joint Set 1 (080/30), which is roughly parallel to the ground surface, and Joint Set 2 (170/90), perpendicular to the valley axis, are persistent (up to 40 m), have a curved and stepped joint surface, aperture with up to a few cm and water flow through the joints
- Joint Set 3 (260/35) has planar joint surfaces, less persistent, terminates mostly into other joints, small aperture with up to 1 mm
- Joint Set 4 (275/80) is less dominant, planar surface

The thesis helped to answer the questions defined in chapter 1.2. First, the aim was to differentiate discontinuities that developed due to glacier-related stress changes or due to tectonic forces. JS1 and JS2 are assumed to be sheeting joints and to have developed because of the deglaciation. They form parallel to the highest applied stress, which is vertically oriented or parallel to the rock slope surface, e.g. due to glacial oversteepening.
Second, the main potential failure mechanisms and which discontinuities contribute to a higher probability of rock slope failure should be defined. Kinematic analyses show that rock slope stability depends dominantly on the geometry of the primary two prominent joint sets with respect to the slope orientation. These joint planes work as base planes for the main potential failure mechanisms planar and wedge sliding. JS1 provides slope parallel planes, favorably oriented for planar sliding. Dependent on the combination with the slope orientation, the rock mass is prone to sliding if the joints are daylighting. Therefore, discontinuities which developed because of glacial processes play a dominant role in the rock slope stability assessment.
The third question was how the stability of rock slopes is affected by (de)glaciation. Rock slope weakening can’t be related to one single process but to the combination of several factors. After glacial retreat, persistent discontinuities developed progressively leading to a

long-term rock mass strength degradation. Joint propagation through previously intact rock bridges may be induced by an increased amount of water intake after precipitation or snow melt. Higher joint water pressure within the rock mass and freeze-thaw weathering may play an important role for progressive joint propagation through rock bridges.

The last question was if there is a spatial or temporal pattern of glacier-related discontinuities recognizable. In order to answer this question properly, additional measurements need to be conducted. More data in the area surrounding the glacier can help to relate the spatial pattern of discontinuities to the highest applied stress by the glacier. Moreover, data from rock walls that recently got ice free is necessary to define a time period in which glacier-related discontinuities evolve.

9.2 Perspectives

For a more detailed description of the joints, data obtained by photogrammetric methods may be helpful. A larger area can be analyzed compared to the traditional field measurements with the compass. Furthermore, it may be possible to obtain data from the opposite side of the valley. It was difficult to access and conduct measurements because of the steep rock walls and the debris cover. The data can be used to compare the joint sets on both valley sides. Changing orientation of joint sets dependent on the surface geometry would be an indication for sheeting joints. Therefore, a more detailed description of the spatial pattern of the joints is necessary to proof whether the joints are tectonic or sheeting joints. A 2D or 3D model of the rock mass is helpful to determine the statistics of the joint set characteristics and for additional kinematic analyses. Furthermore, it is important to do underground observations. Borehole data can be used to check if the spacing of a joint set is increasing with depth, which would be another characteristic for sheeting joints.

Due to climate warming the retreat of glaciers may accelerate, which may lead to an increasing number of rock falls in the higher mountains. Due to the increasing risk the research about paraglacial rock slopes and its stability is important and should be continued in the next decades.

References

Augustinus, P.C. 1995. Glacial valley cross-profile development: the influence of in situ rock stress and rock mass strength, with examples from the Southern Alps, New Zealand.

Baroni, C., Martino, S., Salvatore, M.C., Scarascia Mugnozza, G. & Schilirò, L. 2014. Thermomechanical stress–strain numerical modelling of deglaciation since the Last Glacial Maximum in the Adamello Group (Rhaetian Alps, Italy). *Geomorphology*, **226**, 278–299, http://doi.org/10.1016/j.geomorph.2014.08.013.

Basemap. 2020. Verwaltungsgrundkarte Österreichs: Oberflächenkarte. www.basemap.at/.

Bertrand, A. 2013. Exhuming the core of collosional orogens, the Tauern Window (Eastern-Alps): A geochronological, modelling and structural study.

Carol, H. 1947. The formation of Roches Moutonnées.

Carrivick, J.L., Berry, K., Geilhausen, M., James, W.H., Williams, C., Brown, L.E., Rippin, D.M. & Carver, S.J. 2015. Decadal-scale changes of the ödenwinkelkees, central austria, suggest increasing control of topography and evolution towards steady state. *Geografiska Annaler: Series A, Physical Geography*, **97**, 543–562, http://doi.org/10.1111/geoa.12100.

Carrivick, J.L., Geilhausen, M., Warburton, J., Dickson, N.E., Carver, S.J., Evans, A.J. & Brown, L.E. 2013. Contemporary geomorphological activity throughout the proglacial area of an alpine catchment. *Geomorphology*, **188**, 83–95, http://doi.org/10.1016/j.geomorph.2012.03.029.

Cossart, E., Braucher, R., Fort, M., Bourlès, D.L. & Carcaillet, J. 2008. Slope instability in relation to glacial debuttressing in alpine areas (Upper Durance catchment, southeastern France): Evidence from field data and 10Be cosmic ray exposure ages. *Geomorphology*, **95**, 3–26, http://doi.org/10.1016/j.geomorph.2006.12.022.

Deline, P. & Gruber, S. *et al.* 2015. Ice Loss and Slope Stability in High-Mountain Regions. *In: Snow and Ice-Related Hazards, Risks and Disasters*. Elsevier, 521–561.

Dobinski, W. 2011. Permafrost. *Earth-Science Reviews*, **108**, 158–169, http://doi.org/10.1016/j.earscirev.2011.06.007.

Draebing, D., Krautblatter, M. & Dikau, R. 2014. Interaction of thermal and mechanical processes in steep permafrost rock walls: A conceptual approach. *Geomorphology*, **226**, 226–235, http://doi.org/10.1016/j.geomorph.2014.08.009.

Draebing, D., Krautblatter, M. & Hoffmann, T. 2017. Thermo-cryogenic controls of fracture kinematics in permafrost rockwalls. *Geophysical Research Letters*, **44**, 3535–3544, http://doi.org/10.1002/2016GL072050.

Duriez, J., Scholtès, L. & Donzé, F.-V. 2016. Micromechanics of wing crack propagation for different flaw properties. *Engineering Fracture Mechanics*, **153**, 378–398, http://doi.org/10.1016/j.engfracmech.2015.12.034.

Ewald, A., Hartmeyer, I., Keuschnig, M., Lang, A. & Otto, J.-C. 2019. *Fracture dynamics in an unstable, deglaciating headwall, Kitzsteinhorn, Austria*.

Fiorucci, M., Marmoni, G.M., Martino, S. & Mazzanti, P. 2018. Thermal Response of Jointed Rock Masses Inferred from Infrared Thermographic Surveying (Acuto Test-Site, Italy). *Sensors (Basel, Switzerland)*, **18,** http://doi.org/10.3390/s18072221.

Fischer, L., Amann, F., Moore, J.R. & Huggel, C. 2010. Assessment of periglacial slope stability for the 1988 Tschierva rock avalanche (Piz Morteratsch, Switzerland). *Engineering Geology*, **116**, 32–43, http://doi.org/10.1016/j.enggeo.2010.07.005.

Georesearch. 2020. Project CirqueMonHT - GEORESEARCH. www.georesearch.ac.at/en/areas/research-areas/geo/project-cirquemonht/.

Gigli, G., Frodella, W., Garfagnoli, F., Morelli, S., Mugnai, F., Menna, F. & Casagli, N. 2014. 3-D geomechanical rock mass characterization for the evaluation of rockslide susceptibility scenarios. *Landslides*, **11**, 131–140, http://doi.org/10.1007/s10346-013-0424-2.

GIMP. 2020. GIMP - GNU Image Manipulation Program: Free & Open Source Image Editor. www.gimp.org/.

Gischig, V., Amann, F., Moore, J.R., Loew, S., Eisenbeiss, H. & Stempfhuber, W. 2011. Composite rock slope kinematics at the current Randa instability, Switzerland, based on remote sensing and numerical modeling. *Engineering Geology*, **118**, 37–53, http://doi.org/10.1016/j.enggeo.2010.11.006.

Goodman, R.E. 1976. *Methods of Geological Engineering in Discontinous Rocks*. West Publishing Co.

Grämiger, L.M., Moore, J.R., Gischig, V.S. & Loew, S. 2018. Thermomechanical Stresses Drive Damage of Alpine Valley Rock Walls During Repeat Glacial Cycles. *Journal of Geophysical Research: Earth Surface*, **123**, 2620–2646, http://doi.org/10.1029/2018JF004626.

Grämiger, L.M., Moore, J.R., Gischig, V.S., Loew, S., Funk, M. & Limpach, P. 2020. Hydromechanical Rock Slope Damage During Late Pleistocene and Holocene Glacial Cycles in an Alpine Valley. *Journal of Geophysical Research: Earth Surface*, **125,** http://doi.org/10.1029/2019JF005494.

Gruber, S. & Haeberli, W. 2007. Permafrost in steep bedrock slopes and its temperature-related destabilization following climate change. *Journal of Geophysical Research*, **112,** http://doi.org/10.1029/2006JF000547.

Gschwind, S., Loew, S. & Wolter, A. 2019. Multi-stage structural and kinematic analysis of

a retrogressive rock slope instability complex (Preonzo, Switzerland). *Engineering Geology*, **252**, 27–42, http://doi.org/10.1016/j.enggeo.2019.02.018.

Guerin, A. & Jaboyedoff, M. *et al.* 2019. Detection of rock bridges by infrared thermal imaging and modeling. *Scientific reports*, **9**, 13138, http://doi.org/10.1038/s41598-019-49336-1.

Harris, C. & Arenson, L.U. *et al.* 2009. Permafrost and climate in Europe: Monitoring and modelling thermal, geomorphological and geotechnical responses. *Earth-Science Reviews*, **92**, 117–171, http://doi.org/10.1016/j.earscirev.2008.12.002.

Hartmeyer, I., Delleske, R., Keuschnig, M., Krautblatter, M., Lang, A., Schrott, L. & Otto, J.-C. 2020. *Current glacier recession causes significant rockfall increase: The immediate paraglacial response of deglaciating cirque walls*.

Hencher, S.R., Lee, S.G., Carter, T.G. & Richards, L.R. 2011. Sheeting Joints: Characterisation, Shear Strength and Engineering. *Rock Mechanics and Rock Engineering*, **44**, 1–22, http://doi.org/10.1007/s00603-010-0100-y.

Höck, V. & Pestal, G. 1994. Geologische Karte der Republik Österreich 1:50.000: Wien: Geologische Bundesanstalt.

Hooyer, T.S., Cohen, D. & Iverson, N.R. 2012. Control of glacial quarrying by bedrock joints. *Geomorphology*, **153-154**, 91–101, http://doi.org/10.1016/j.geomorph.2012.02.012.

Huang, D., Cen, D., Ma, G. & Huang, R. 2014. Step-path failure of rock slopes with intermittent joints. *Landslides*, 911–926.

Hudson, J.A. 1989. *Rock Mechanics Principles in engineering practice*. Butterworths, London.

Hugentobler, M., Loew, S., Aaron, J., Roques, C. & Oestreicher, N. 2020. Borehole monitoring of thermo-hydro-mechanical rock slope processes adjacent to an actively retreating glacier. *Geomorphology*, **362**, 107190, http://doi.org/10.1016/j.geomorph.2020.107190.

ISRM. 1978. Suggested methods for the quantitative description of discontinuities in rock masses. *International Journal of Rock Mechanics and Mining Sciences*, 319–368.

Krautblatter, M., Funk, D. & Günzel, F.K. 2013. Why permafrost rocks become unstable: a rock-ice-mechanical model in time and space. *Earth Surface Processes and Landforms*, **38**, 876–887, http://doi.org/10.1002/esp.3374.

Krautblatter, M. & Leith, K. 2015. Glacier- and permafrost-related slope instabilities.

Leith, K., Moore, J.R., Amann, F. & Loew, S. 2014a. In situ stress control on microcrack generation and macroscopic extensional fracture in exhuming bedrock. *Journal of Geophysical Research: Solid Earth*, **119**, 594–615, http://doi.org/10.1002/2012JB009801.

Leith, K., Moore, J.R., Amann, F. & Loew, S. 2014b. Subglacial extensional fracture development and implications for Alpine Valley evolution. *Journal of Geophysical Research: Earth Surface*, **119**, 62–81, http://doi.org/10.1002/2012JF002691.

Martel, S.J. 2017. Progress in understanding sheeting joints over the past two centuries. *Journal of Structural Geology*, **94**, 68–86, http://doi.org/10.1016/j.jsg.2016.11.003.

Matasci, B., Stock, G.M., Jaboyedoff, M., Carrea, D., Collins, B.D., Guérin, A., Matasci, G. & Ravanel, L. 2017. Assessing rockfall susceptibility in steep and overhanging slopes using three-dimensional analysis of failure mechanisms. *Landslides*, **15**, 859–878, http://doi.org/10.1007/s10346-017-0911-y.

McColl, S.T. 2012. Paraglacial rock-slope stability. *Geomorphology*, **153-154**, 1–16, http://doi.org/10.1016/j.geomorph.2012.02.015.

Messenzehl, K.C. 2018. Rock slope instability in alpine geomorphic systems, Switzerland.

Mey, J., Scherler, D., Wickert, A.D., Egholm, D.L., Tesauro, M., Schildgen, T.F. & Strecker, M.R. 2016. Glacial isostatic uplift of the European Alps. *Nature communications*, **7**, 13382, http://doi.org/10.1038/ncomms13382.

Munn, R.E. 2002. *Encyclopedia of global environmental change*. Wiley, Chichester, New York.

ÖBB-Infrastruktur AG. 2021. Kraftwerk Tauernmoos. infrastruktur.oebb.at/de/projekte-fuer-oesterreich/bahnstrom/kraftwerke-und-frequenzumformer/kraftwerk-tauernmoos.

OpenTopoMap. 2020. Topographische Karten aus OpenStreetMap. opentopomap.org/#map=13/47.13602/12.67891.

QGIS. 2020. QGIS 3 Geographic Information System: Open Source Geospatial Foundation Project. www.qgis.org/de/site/.

Ravanel, L., Magnin, F. & Deline, P. 2017. Impacts of the 2003 and 2015 summer heatwaves on permafrost-affected rock-walls in the Mont Blanc massif. *The Science of the total environment*, **609**, 132–143, http://doi.org/10.1016/j.scitotenv.2017.07.055.

Rocscience. 2020. Dips 7.0. www.rocscience.com/software/dips.

SAGIS. 2020. Salzburger Geographisches Informationssystem, Land Salzburg: Orthofoto. www.salzburg.gv.at/sagismobile/sagisonline/map/Basiskarten/Alle%20Themen.

Schmid, S.M., Scharf, A., Handy, M.R. & Rosenberg, C.L. 2013. The Tauern Window (Eastern Alps, Austria): a new tectonic map, with cross-sections and a tectonometamorphic synthesis. *Swiss Journal of Geosciences*, **106**, 1–32, http://doi.org/10.1007/s00015-013-0123-y.

Schoeneich, P., Dall'Amico, M., Deline, P. & Zischg, A. 2011. Hazards related to permafrost and to permafrost degradation: PermaNET project, state-of-the-art report 6.2.

Schrott, L., Otto, J.-C. & Keller, F. 2012. Modelling alpine permafrost distribution in the

Hohe Tauern region, Austria.

Shang, J., West, L.J., Hencher, S.R. & Zhao, Z. 2018. Geological discontinuity persistence: Implications and quantification. *Engineering Geology*, **241**, 41–54, http://doi.org/10.1016/j.enggeo.2018.05.010.

Singh, B. & Goel, R.K. 1999. *Rock Mass Classification: A Practical Approach in Civil Engineering,* 1st ed. Elsevier.

Slupetzky, H. 2020. Das Ödenwinkel- und Riffelkees (Stubachtal, Hohe Tauern) und die Entstehung von Schuttnetzwerken in den Gletschervorfeldern.: Eine Dokumentation über 60 Jahre Forschung. *Salzburger Geographische Arbeiten*.

Stead, D. & Wolter, A. 2015. A critical review of rock slope failure mechanisms: The importance of structural geology. *Journal of Structural Geology*, **74**, 1–23, http://doi.org/10.1016/j.jsg.2015.02.002.

Strunden, J., Ehlers, T.A., Brehm, D. & Nettesheim, M. 2015. Spatial and temporal variations in rockfall determined from TLS measurements in a deglaciated valley, Switzerland. *Journal of Geophysical Research: Earth Surface*, **120**, 1251–1273, http://doi.org/10.1002/2014JF003274.

Tuckey, Z. & Stead, D. 2016. Improvements to field and remote sensing methods for mapping discontinuity persistence and intact rock bridges in rock slopes. *Engineering Geology*, **208**, 136–153, http://doi.org/10.1016/j.enggeo.2016.05.001.

van Everdigen, R.O., Harris, S.A., French, H.M., Heginbottom, J.A., Johnston, G.H. & Ladanyi, B., Sego, D. C. 1998. Glossary of permafrost and related ground-ice terms.

Veselá, P., Söllner, F., Finger F. & Gerdes, A. 2011. Magmato-sedimentary Carboniferous to Jurassic evolution of the western Tauern window, Eastern Alps (constraints from U-Pb zircon dating and geochemistry). *International Journal of Earth Sciences*, **100**, 993–1027, http://doi.org/10.1007/s00531-010-0596-0.

Walter, F. & Amann, F. *et al.* 2020. Direct observations of a three million cubic meter rock-slope collapse with almost immediate initiation of ensuing debris flows. *Geomorphology*, **351**, 106933, http://doi.org/10.1016/j.geomorph.2019.106933.

Willenberg, H., Loew, S., Eberhardt, E., Evans, K.F., Spillmann, T., Heincke, B., Maurer, H. & Green, A.G. 2008. Internal structure and deformation of an unstable crystalline rock mass above Randa (Switzerland): Part I — Internal structure from integrated geological and geophysical investigations. *Engineering Geology*, **101**, 1–14, http://doi.org/10.1016/j.enggeo.2008.01.015.

Wyllie, D.C. & Mah, C.W. 2005. *Rock Slope Engineering: Civil and Mining,* 4th ed. Taylor & Francis.

Xu, J. & Li, Z. 2019. Crack Propagation and Coalescence of Step-Path Failure in Rocks. *Rock Mechanics and Rock Engineering*, **52**, 965–979, http://doi.org/10.1007/s00603-

018-1661-4.

ZAMG. 2021. Klimaübersichten - Jahrbuch. www.zamg.ac.at/cms/de/klima/klimauebersichten/jahrbuch.

Zemp, M., Haeberli, W., Hoelzle, M. & Paul, F. 2006. Alpine glaciers to disappear within decades? *Geophysical Research Letters*, **33,** http://doi.org/10.1029/2006GL026319.

Ziegler, M., Loew, S. & Moore, J.R. 2013. Distribution and inferred age of exfoliation joints in the Aar Granite of the central Swiss Alps and relationship to Quaternary landscape evolution. *Geomorphology*, **201**, 344-362, http://doi.org/10.1016/j.geomorph.2013.07.010.

Appendix A

Measurement Point	Location	Orientation		Comments	
1		240/24 248/15	235/20		
2		298/45 246/30	322/77 156/72		
3		080/26 078/16 060/25 062/26 090/35 254/28 274/45 276/45	338/90 342/90 174/95 052/45 258/45 262/30 260/30 150/70 162/70		
4	12°37’57.104’’E 47°7’30.537’’N	078/35 070/42 074/40	000/86 342/87 342/89	Scanline 4	
5	12°37’57.416’’E 47°7’28.584’’N			Scanline 1-3	
6	12°38’0.893’’E 47°7’25.352’’N	084/30 082/26 088/24	174/90 180/90 178/86		
7		074/40 070/30 070/42	004/88 000/90		
8	12°38’3.009’’E 47°7’23.140’’N			Scanline 5 + 6	
9		300/67 294/65 348/75	320/60 80/10 86/10	360/78	

Scanline 1

	Label	Trend	Plunge	Length (m)	Date
Scanline	1	342	8	5,6	28.08.20

	Dip Direction	Dip	Height (m)	Width (m)	Rock Type
Outcrop	72	70	10	6	Granitic Gneiss

No.	Type	Inters. Distance (m)	Spacing (m)	α	β	Semi-trace length (m)
1	J2	0,9	0,90	164	78	8
2	J2	2,4	1,50	168	85	8
3		3,2	0,80	14	90	1
4	J2	3,5	0,30	346	85	
5	J2	5,6	2,10	162	85	3

No.	Persistence	Termination	Waviness	Roughness	Aperture (mm)	Comments
1	P	O	2,5	9		
2	P	O	2,5	9		
3	P	R	1	4	2	
4	P	J	1,5	6	10	
5	P	J	2	3		

Scanline 2

	Label	Trend	Plunge	Length (m)	Date
Scanline	2	164	10	5	28.08.20

	Dip Direction	Dip	Height (m)	Width (m)	Rock Type
Outcrop	162	85	10	5	Granitic Gneiss

No.	Type	Inters. Distance (m)	Spacing (m)	α	β	Semi-trace length (m)
1		1,14	1,14			0,1
2	J4	2,34	1,20	260	88	8
3	J4	3,14	0,80	262	80	2
4	J4	3,94	0,80	258	88	1
5	J4	4,07	0,13	264	90	0,3
6		4,45	0,38			

No.	Persistence	Termination	Waviness	Roughness	Aperture (mm)	Comments
1		R	3	10	2 to 4	fissure
2	P	O	3	10		
3	P	J	2,5	8	5	fissure
4		J	1,5	6		
5		J	1,5	3		
6			2,5	8	10	

Scanline 3

	Label	Trend	Plunge	Length (m)	Date
Scanline	3	342	15	5,3	28.08.20

	Dip Direction	Dip	Height (m)	Width (m)	Rock Type
Outcrop	350	75	20	6	Granitic Gneiss

No.	Type	Inters. Distance (m)	Spacing (m)	α	β	Semi-trace length (m)
1		0,05	0,05			3
2	J4	0,4	0,35	268	80	20
3	J4	0,8	0,40	268	45	1
4	J4	1,5	0,70	268	75	1
5	J4	2	0,50	268	75	0,1
6		3	1,00			0,2
7		3,6	0,60			0,1
8	J3	5,15	1,55	258	42	1,5

No.	Persistence	Termination	Waviness	Roughness	Aperture (mm)	Comments
1	P	R	1,5	5	10	
2		O	2	4	10	further up aperture up to 5 cm
3		R	2	7	5	
4		J	2,5	6		curved
5		J	1,5	5		
6		J				stepped
7		J				stepped, very irregular
8	P	J	1,5	4	5	

Scanline 4

	Label	Trend	Plunge	Length (m)	Date
Scanline	4	340	90	10,5	29.08.20

	Dip Direction	Dip	Height (m)	Width (m)	Rock Type
Outcrop	80	30	20	10,5	Granitic Gneiss

No.	Type	Inters. Distance (m)	Spacing (m)	α	β	Semi-trace length (m)
1	J2	1,55	1,55	8	82	1,5
2	J2	1,9	0,35	4	82	1,5
3	J2	2	0,10	4	82	5
4	J2	2,77	0,77	358	85	2
5		4,1	1,33	126	77	0,5
6	J2	5,5	1,40	350	85	15
7	J2	5,95	0,45	345	85	15
8	J2	6,4	0,45	345	85	2
9	J2	6,9	0,50	345	85	15
10	J2	8,2	1,30	164	80	5
11	J2	8,6	0,40	170	70	15
12	J2	9,9	1,30	340	88	0,2
13	J2	10,45	0,55	158	82	6

No.	Persistence	Termination	Waviness	Roughness	Aperture (mm)	Comments
1	P	J	1,5	3	1	
2	I	J	2	7		stepped
3	P	R	1,5	3		
4	P	J	2	3	0,5 - 1	
5	P	R	1,5	2		
6	I	J	2,5	4	2 - 5	stepped
7	I	J ?	2,5	3	5	termination in grass
8	P	R	2,5	3		
9	P	R	2,5	7	2	stepped
10	P	J	3	4	2	curved
11	P	R	2,5	3	10	
12	I	J ?	1	3	2	termination in grass
13	I	J	2,5	3	5	stepped

Scanline 5

	Label	Trend	Plunge	Length (m)	Date
Scanline	5	280	35	7,6	29.08.20

	Dip Direction	Dip	Height (m)	Width (m)	Rock Type
Outcrop	174	82	2	40	Granitic Gneiss

No.	Type	Inters. Distance (m)	Spacing (m)	α	β	Semi-trace length (m)
1	J4	0,0	0,00	282	80	0,5
2	J4	0,6	0,60	282	80	0,5
3	J4	2,3	1,70	280	82	0,5
4	J4	3,1	0,80	278	80	0,7
5	J4	3,8	0,70	270	80	1
6	J4	4,8	1,00	282	82	1,5
7	J4	6,9	2,10	290	85	0,5

No.	Persistence	Termination	Waviness	Roughness	Aperture (mm)	Comments
1	P	O	1,5	4		
2	P	O	1,5	4		
3	P	O	1,5	4	2	through whole outcrop
4	P	O	1,5	4		
5	P	O	1,5	5		through whole outcrop
6	P	O	1,5	4		
7	P	O	1,5	4		

Scanline 6

	Label	Trend	Plunge	Length (m)	Date
Scanline	6		90	1,5	29.08.20

	Dip Direction	Dip	Height (m)	Width (m)	Rock Type
Outcrop	174	82	2	40	Granitic Gneiss

No.	Type	Inters. Distance (m)	Spacing (m)	α	β	Semi-trace length (m)
1	J1	0,00	0,00	88	37	
2	J1	0,35	0,35	86	35	0,2
3	J1	0,85	0,50	87	35	0,3
4	J1	1,1	0,25	86	38	0,1
5	J1	1,25	0,15	84	33	0,3

No.	Persistence	Termination	Waviness	Roughness	Aperture (mm)	Comments
1	P					all parallel
2	P	J	2,5	7		
3	P	J	2,5	7		
4	P	J/R	2,5	7		
5	P	J	2,5	7		